

Prompt Photon Production at HERA

DISSERTATION

zur Erlangung des Doktorgrades
des Fachbereichs Physik
der Universität Hamburg

vorgelegt von

Rachid Lemrani-Alaoui

aus Frankreich

Hamburg
2003

Gutachter der Dissertation:	Prof. Dr. F.-W. Büsser Prof. Dr. B. Naroska
Gutachter der Disputation:	Prof. Dr. F.-W. Büsser Prof. Dr. G. Heinzelmann
Datum der Disputation:	25.02.2003
Vorsitzender des Prüfungsausschusses:	Dr. H.D. Rüter
Vorsitzender des Promotionsausschusses:	Prof. Dr. G. Huber
Dekan des Fachbereichs Physik	Prof. Dr. F.-W. Büsser

Abstract

Inclusive prompt photons and prompt photons together with a jet are measured in photo-production at HERA. Cross sections are presented as a function of transverse energy E_T^γ and pseudorapidity η^γ for $E_T^\gamma > 5$ GeV and $-1 < \eta^\gamma < 0.9$ in the inelasticity range $0.2 < y < 0.7$ corresponding to γp center of mass energies $140 < W < 270$ GeV. For the prompt photons + jet analysis a jet was required in addition with $E_T^{jet} > 4.5$ GeV and $-1.5 < \eta^{jet} < 2.3$. The data were taken with the H1 detector in the years 1996-2000 using an integrated luminosity of 105 pb^{-1} . After selection of prompt photon candidates, a sizable amount of background from π^0 mesons remains and the γ signal is extracted by a likelihood technique using calorimetric shower shape variables. The results are compared to the PYTHIA and HERWIG event generators and to a NLO-QCD calculation. PYTHIA and HERWIG predictions describes the data well in shape, are however low in normalisation. The NLO-QCD calculation describes the data quite well in the presented η^γ and E_T^γ ranges. It has however a tendency to overshoot the data especially at large η^γ which could be explained by multiple interactions.

Kurzfassung

Es wird eine Messung zur Photoproduktion von prompten Photonen bei HERA vorgestellt. Die Photonen wurden dabei sowohl inklusiv als auch zusammen mit einem Jet nachgewiesen. Erzeugungsquerschnitte werden als Funktion der transversalen Energie E_T^γ und der Pseudorapazität η^γ für $E_T^\gamma > 5$ GeV und $-1 < \eta^\gamma < 0.9$ im Unelastizitätsbereich $0.2 < y < 0.7$ präsentiert. Dieser Bereich entspricht Schwerpunktsenergien W im Photon-Proton System von $140 < W < 270$ GeV. Im Fall der nichtinklusive Produktion prompter Photonen wurde zusätzlich ein Jet mit $E_T^{jet} > 4.5$ GeV und $-1.5 < \eta^{jet} < 2.3$ gefordert. Die Daten wurden mit der H1 Detektor in den Jahren 1996-2000 registriert, wobei eine integrierte Luminosität von 105 pb^{-1} benutzt wurde. Die Auswahl der Ereignisse mit Kandidaten prompter Photonen enthält noch einen erheblichen durch π^0 -Mesonen verursachten Untergrundanteil. Der Anteil prompter Photonen wird durch eine *Maximum-Likelihood*-Technik unter Verwendung von Variablen bestimmt, welche die im Kalorimeter gemessenen Schauerformen beschreiben. Die Ergebnisse werden mit den Ereignisgeneratoren PYTHIA und HERWIG und einer NLO-QCD-Rechnung verglichen. Die Voraussagen von PYTHIA und HERWIG beschreiben zwar gut die relativen Abhängigkeiten der Querschnitte, sie sind aber absolut zu niedrig. Die NLO-QCD-Rechnung beschreibt die Ergebnisse in den untersuchten η^γ und E_T^γ Bereichen recht gut, allerdings mit einer Tendenz, vor allem bei großen η^γ , etwas über den Messungen zu liegen. Dies kann durch partonische Mehrfachwechselwirkungen erklärt werden.

To my brother Lahcen

Contents

Introduction	1
1 Theoretical framework	3
1.1 ep scattering	3
1.1.1 Kinematics	3
1.1.2 Structure functions	4
1.2 The naive quark parton model	5
1.2.1 The QCD Improved Parton Model	5
1.2.2 The evolution of Parton Distributions	6
1.3 The structure of the Photon	8
1.4 Photo-production at HERA	9
2 Prompt photon production	11
2.1 Prompt Photon Production in γp reactions	11
2.2 Previous experimental results	15
2.2.1 Prompt Photon at HERA	15
2.2.2 Prompt Photons at other experiments	16
3 Monte-Carlo simulation	20
3.1 Event Generators	20
3.1.1 Treatment of hadronisation	21
3.1.2 Multiple interactions	22
3.2 PYTHIA and HERWIG Monte Carlo Samples	22
4 The H1 experiment at HERA	26
4.1 The HERA accelerator	26
4.2 The H1 detector	27
4.2.1 The calorimeters	29
4.2.2 The tracking system	32
4.2.3 The Trigger System	33
4.2.4 The luminosity system	35
4.3 Simulation of the H1 detector	35
5 Reconstruction	37
5.1 Photon reconstruction	37
5.1.1 Photon identification	37

5.1.2	Kinematic measurements	40
5.2	Reconstruction of the hadronic final state	43
5.2.1	Hadronic final state measurement	43
5.2.2	Hadronic energy scale of the Liquid Argon calorimeter	44
5.3	Jet reconstruction	44
5.3.1	Jet k_T algorithm	45
5.4	Reconstruction of further kinematic variables	45
6	Event Selection	48
6.1	Data taking periods and run selection	48
6.2	Photon fiducial volume cuts	49
6.3	Triggering	50
6.4	Background rejection	53
6.5	Event selection summary	58
7	Extraction of the signal	61
7.1	π^0 and η background	62
7.2	The shower shape variables	62
7.3	Signal extraction	65
7.3.1	Discriminator definition	65
7.3.2	Fit of the different particle contributions to the data	66
7.4	Comparison to PYTHIA	70
7.4.1	E_T and η distributions with and without jet requirement	70
7.4.2	Variation of the isolation cuts	74
8	Cross section calculation	76
8.1	Cross section determination	76
8.1.1	Correction to generator level	76
8.1.2	Bin Purities	77
8.1.3	Cross sections	77
8.2	Systematic uncertainties	78
9	Results and comparison to theory	85
9.1	PYTHIA and HERWIG	85
9.2	NLO calculation	85
9.3	Multiple interactions	89
9.4	Cross section of inclusive prompt photon production	90
9.5	Comparison to ZEUS results	91
9.6	Cross section of Prompt Photon + jet production	92
10	Summary and outlook	95
	Bibliography	101
	List of figures	101
	List of tables	103

Introduction

The standard model, a theory completed in the beginning of the seventies, has been very successful in describing all the collected data in high energy physics. However it is expected that a new theory is needed at the higher energies which will be reached during the next decade. A few aspects of the standard model based on a quantum gauge field theory are described here. The constituents of all the existing matter are elementary particles called fermions. They interact with each other through the electromagnetic, the weak, the strong and the gravitational force. The electromagnetic and weak forces have been unified into the electroweak force. These interactions take place by exchange between fermions of so-called bosons: photon, weak bosons (W^+ , W^- and Z) for the electroweak force, and eight gluons for the strong force. The strength of a force is given by the coupling constants, the fine structure constant α for the electroweak and α_s for the strong force. The gravitational force can be neglected in high energy physics and is not part of the standard model. The fermions are classified in two categories: the six quarks which are sensitive to electroweak and strong forces and the six leptons which are only sensitive to electroweak forces. The fermions are classified in three generations of two quarks (*up, down*), (*charm, strange*), (*top, bottom*) and of two leptons (*electron, electron neutrino ν_e*), (*muon, muon neutrino ν_μ*), (*tau, tau neutrino ν_τ*). The mass of the particles is due to a coupling to the Higgs boson, the only still undiscovered particle of the standard model. A few parameters (e.g coupling constants, mixing angles, masses) are needed for the theory and are being measured by the experiments.

Physicists use high energy machines to probe matter at small scales and to produce new particles. In scattering experiments either beams of particles are scattered against fixed targets (fixed target experiments) or two high energetic particle beams are brought to collide with each other. The proton appears to be formed of quarks and gluons at high energies, and many other particles (the hadrons) composed of quarks and gluons have been observed. Nowadays the proton is being probed at the HERA collider at scale a thousand times smaller than its own size by using beams of electrons and protons. Higher energies allow also to produce new particles and all the fermions of the standard model have indeed been observed starting with the electron in 1897 up to the tau neutrino hundred years later.

After a collision the properties (observables) of the produced particles are measured in a detector. To a first approximation a pair of elementary particles from the colliding beams interact with each other. However a lot of complications arise due to the composite structure of the colliding particles and many other interactions and processes take place. For instance produced quarks and gluons are not observed directly. Instead, quarks and gluons produce jets of hadrons following a process called hadronisation. The hadronisation of quarks and gluons is extremely difficult to describe using the standard model and is not fully understood theoretically. However

models have been developed and they are useful to reconstruct the properties of the quarks and gluons themselves from the observation of the jets. The observation of a photon in the final state is a cleaner measurement because it is less sensitive to the hadronisation models. These so-called prompt photons are produced through the interaction of the elementary particles of the beams.

In chapter 1 ep physics at HERA is shortly discussed, in particular deep inelastic scattering and photo-production. Chapter 2 introduces theoretical aspects of the prompt photon production and gives some previous experimental results. In chapter 3 the employed Monte-Carlo event generators are presented and the produced Monte-Carlo samples are listed. Chapter 4 describes briefly the HERA machine and the H1 detector, in particular the components relevant for this analysis. In chapter 5 the photon and jet reconstruction are explained. Chapter 6 describes the event selection. In chapter 7 the signal and background separation is presented. In chapter 8 extraction of cross-sections and the systematic errors are discussed. In chapter 9 a comparison of the inclusive prompt photon analysis to the theory is presented and further results from the prompt-photon + jet analysis are discussed. In chapter 10 the presented analysis and the results are summarized.

Chapter 1

Theoretical framework

Prompt photon production as discussed in this report is a special case of ep scattering at HERA. In this chapter the basic concepts of ep scattering are presented, in particular deep inelastic scattering (DIS) and photo-production.

1.1 ep scattering

The main process studied at HERA is deep inelastic scattering (DIS) of electrons and protons. It is shortly described here to define the relevant kinematics and the concept of structure functions.

1.1.1 Kinematics

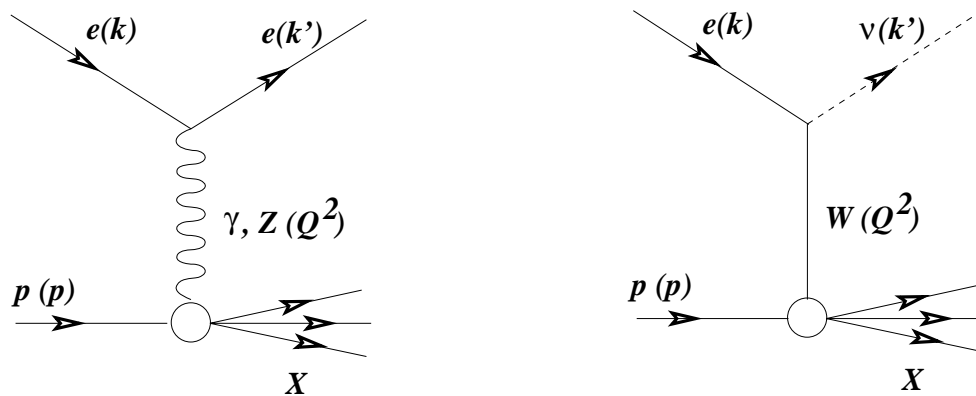


Figure 1.1: *Diagrams of electron and proton scattering via photon and Z exchange for neutral current interactions and W exchange for charged current interactions. The four-momentum vectors of the particles are given in parentheses.*

Figure 1.1 shows the DIS processes where an electron (e) interacts with a proton (p). In neutral current (NC) interactions ($e^\pm p \rightarrow e^\pm X$) a neutral boson (γ, Z) is exchanged leading in

the final state to a scattered electron and the hadronic final state X (break-up of the proton). In charged current (CC) interactions ($e^- p \rightarrow \nu_e X$, $e^+ p \rightarrow \bar{\nu}_e X$) a charged boson (W^-, W^+) is exchanged with a neutrino ν in the final state instead of the scattered electron.

We define k and k' as the incident and scattered lepton four-momenta, p as the proton four-momentum and $q = k - k'$ as the momentum transfer. The process is determined by the 3 Lorentz invariant variables:

$$\text{Four-momentum transfer squared: } Q^2 = -q^2 = -(k - k')^2, \quad Q^2 \in [0, s] \quad (1.1)$$

$$\text{Björken scaling variable: } x = \frac{Q^2}{2p \cdot q}, \quad x \in [0, 1] \quad (1.2)$$

$$\text{Inelasticity: } y = \frac{p \cdot q}{p \cdot k}, \quad y \in [0, 1] \quad (1.3)$$

Neglecting the masses of the electron and of the proton the 3 variables are related by:

$$Q^2 = s \cdot x \cdot y \quad (1.4)$$

where $s = (k + p)^2$ is the total invariant energy squared.

The invariant mass W of the hadronic final state is given by:

$$W^2 = (p + q)^2. \quad (1.5)$$

1.1.2 Structure functions

The DIS cross-section for the photon exchange is given by:

$$\frac{d^2 \sigma^{ep}(x, Q^2)}{dx dQ^2} = \frac{4\pi\alpha^2}{xQ^4} \left[\frac{y^2}{2} 2xF_1(x, Q^2) + (1-y)F_2(x, Q^2) \right] \quad (1.6)$$

where α is fine structure constant and F_1 and F_2 are the structure functions of the proton as a function of x and Q^2 . The contributions of Z^0 and W^\pm exchanges is small at low Q^2 : $Q^2 \ll M_{Z^0}^2, M_W^2$. This is due to the propagator terms of the form $1/(Q^2 + M_{Z^0}^2)$ respectively $1/(Q^2 + M_W^2)$ for the weak exchange. Using the longitudinal structure function $F_L = F_2 - 2xF_1$ the cross-section can be written as:

$$\frac{d^2 \sigma^{ep}(x, Q^2)}{dx dQ^2} = \frac{2\pi\alpha^2}{xQ^4} \left[(1 + (1-y)^2)F_2(x, Q^2) - y^2 F_L(x, Q^2) \right] \quad (1.7)$$

In most of the phase space at HERA the differential cross-section is dominated by F_2 . Only at large y there is a sizable effect of F_L on the cross-section.

1.2 The naive quark parton model

The structure functions defined in the previous section are related in the quark-parton model (QPM) to the quark distributions in the proton [1]. It is assumed that the proton is a stream of parallel partons i with electric charges e_i which can be described by densities $q_i(x)$. The structure function is then given by: $F_2(x, Q^2) = F_2(x) = \sum e_i^2 x q_i(x)$.

For spin $\frac{1}{2}\hbar$ quarks the cross-section for longitudinally polarized photons is zero (Callan-Gross relation [2]): $2xF_1(x) = F_2(x)$

The structure functions do not depend on Q^2 . This so-called scaling behavior, predicted by Björken for large Q^2 and large $1/x$, is fulfilled in the QPM.

The QPM approximation holds for protons with very high momenta (infinite momentum frame). The proton is then almost flat due to Lorentz contraction and the interaction time is very small due to time dilatation. In this approximation the quarks of the proton are far from each-other and have no time to interact with each-other. The Björken variable x is in this model equal to the proton momentum fraction carried by struck quark.

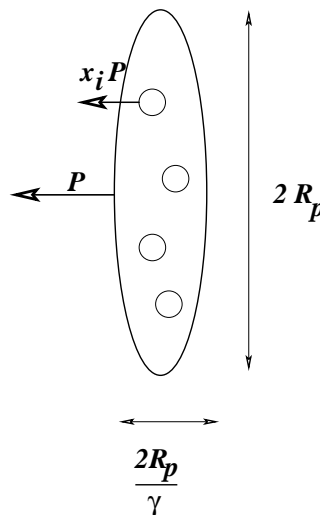


Figure 1.2: Picture of a Lorentz contracted proton with momentum P . Inside the proton the partons i with momentum fraction $x_i P$ are almost free during the interaction. The contraction factor is given by the inverse Lorentz factor $1/\gamma$.

1.2.1 The QCD Improved Parton Model

That the QPM is insufficient got first apparent by the observation that the momentum sum : $\sum \int_0^1 dx q_i(x)x < 1$ (about one half of the momentum is missing) [3].

The theory of strong interaction, Quantum Chromodynamique (QCD), introduces also neutral partons in the proton: the gluons. In QCD, interactions of partons take place through gluons by gluon radiation from quarks and gluon splitting in $q\bar{q}$ pairs. This leads to a sea of quarks and gluons in addition to the valence quarks (see Figure 1.3). The Björken scaling is now broken

leading to a decrease of $F_2(x, Q^2)$ at large Q^2 and large x and an increase at small x as indicated in Figure 1.4. This can simply be explained by a depletion of high x quarks due to gluon radiation at large Q^2 , where smaller structures can be resolved and a corresponding accumulation of sea quarks at small x . Another QCD effect is that the quarks acquire transverse momenta from gluon radiation leading to a non-zero longitudinal structure function F_L .

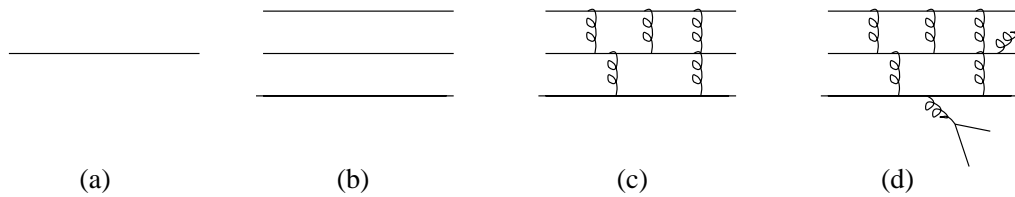


Figure 1.3: *The different models for the proton. At low energies the proton behaves as a point-like particle (a). (b) shows the three free valence quarks in the proton. In (c) the valence quarks are interacting via gluons. In (d) a sea of quarks and gluons appears due to QCD effects like gluon radiation from quarks and gluon splitting in $q\bar{q}$ pairs.*

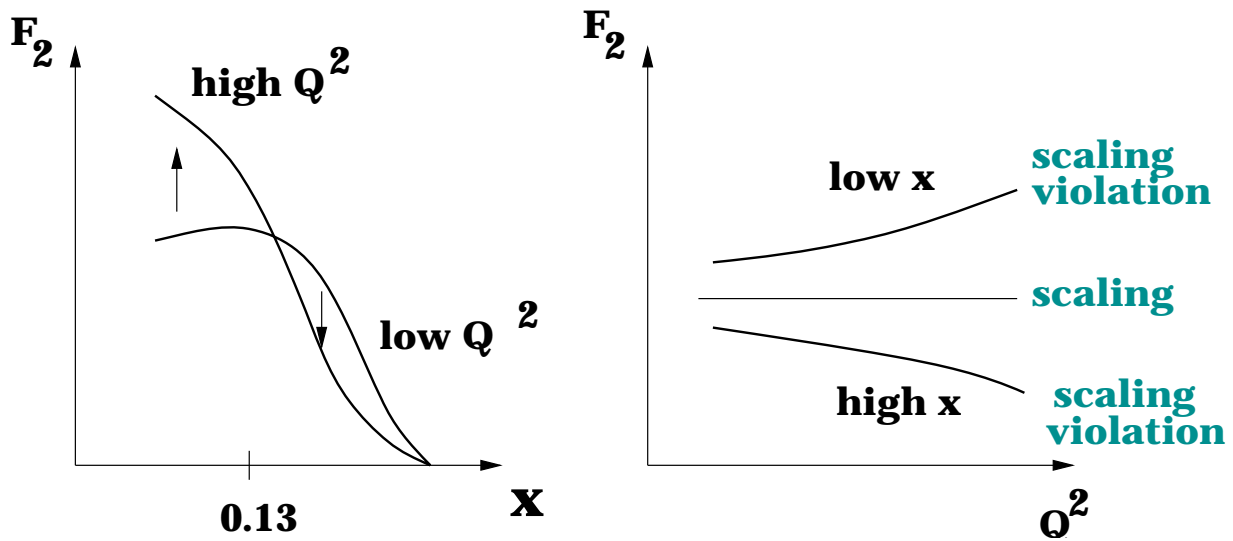


Figure 1.4: *Sketch of the variation of F_2 as a function of x and Q^2 .*

1.2.2 The evolution of Parton Distributions

The partons distributions cannot yet be calculated perturbatively. The Dokshitzer-Gribov-Lipatov-Altarelli-Parisi (DGLAP) equations [4–7] give though the evolution of the parton distributions $q_i(x)$ and $g(x)$ with Q^2 (eqs. 1.8,1.9). Thus for known parton distributions at scale Q_0^2 one can derive the parton distributions at scale Q^2 .

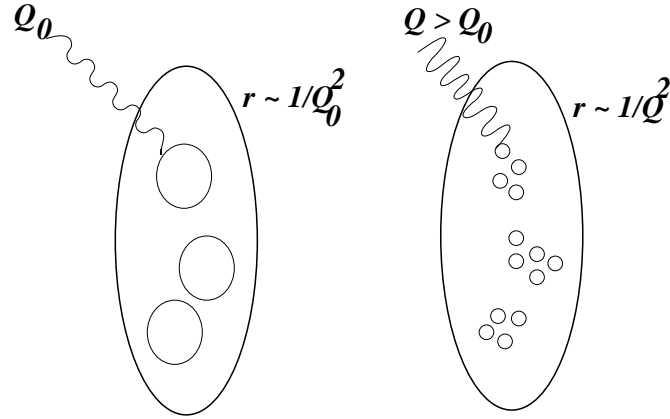


Figure 1.5: Picture of a proton probed by photons of different virtualities Q_0 and $Q > Q_0$. As the virtuality increases smaller structure are resolved. A quark appearing as point-like at virtuality Q_0 , may appear to have radiated gluons at higher virtuality Q .

$$\frac{dq_i(x, Q^2)}{d \ln Q^2} = \frac{\alpha(Q^2)}{2\pi} \int_x^1 \frac{dy}{y} \left[\sum_j q_j(y, Q^2) P_{q_j \rightarrow q_i} \left(\frac{x}{y} \right) + g(y, Q^2) P_{g \rightarrow q_i} \left(\frac{x}{y} \right) \right] \quad (1.8)$$

$$\frac{dg(x, Q^2)}{d \ln Q^2} = \frac{\alpha(Q^2)}{2\pi} \int_x^1 \frac{dy}{y} \left[\sum_j q_j(y, Q^2) P_{q_j \rightarrow g} \left(\frac{x}{y} \right) + g(y, Q^2) P_{g \rightarrow g} \left(\frac{x}{y} \right) \right] \quad (1.9)$$

The splitting functions $P_{j \rightarrow i}$ reflect for instance that a quark of momentum x can be the product of a quark of momentum $y > x$ radiating a gluon of momentum $y - x$ or of the splitting of a gluon. These functions give the probabilities of the leading-order diagrams of figure 1.6. They have also been computed at next-to-leading order [8].

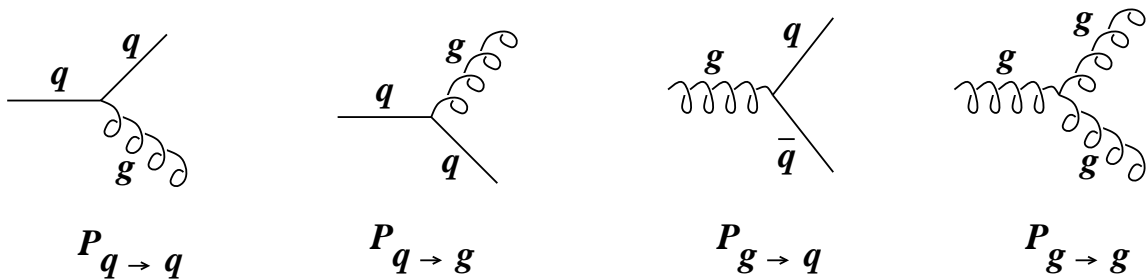


Figure 1.6: The probability of the shown leading order diagrams is given by the splitting functions $P_{q \rightarrow q}$, $P_{q \rightarrow g}$, $P_{g \rightarrow q}$, $P_{g \rightarrow g}$.

1.3 The structure of the Photon

In the standard model the photon is the gauge boson for the electromagnetic force. The photon is an elementary particle. However it can fluctuate into virtual pairs of charged leptons or quarks for a short time according to the quantum uncertainty principle.

For a photon of high energy the quark-antiquark pair can develop into a quark-gluon cascade leading to a complicated partonic object with the same quantum numbers as the photon. This development is not calculable in perturbative QCD and models using parametrisations constrained by measurements have been developed.

At high Q^2 the photon has no time to fluctuate: it behaves as a point-like particle. But when the time of interaction is much smaller than the fluctuation time, the photon behaves as a hadronic object and there are indeed similarities in photon-proton and hadron-proton interactions.

The concept of hadronic structure for the photon was originally introduced in the Vector-Dominance-Model (VDM) [9]. It considers the photon as a superposition of vector-mesons with the same quantum numbers i.e. in terms of vector-meson wave-functions:

$$|\gamma\rangle = \sum_{V=\rho,\omega,\phi,\dots} c_V |V\rangle. \quad (1.10)$$

The VDM works well at low γp center-of-mass energies but is insufficient at high energies. In general three components are then considered as illustrated in Fig 1.7: the bare component where the photon doesn't fluctuate, the anomalous or point-like component where pQCD can be applied, and the non-perturbative VDM component:

$$\sigma^{\gamma p} = \sigma_{dir}^{\gamma p} + \sigma_{anom}^{\gamma p} + \sigma_{VDM}^{\gamma p} \quad (1.11)$$

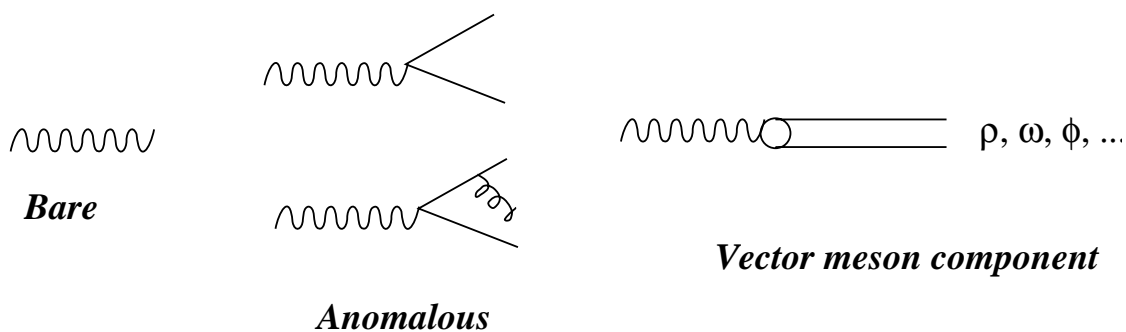


Figure 1.7: The three components of the photon structure: the bare component where the photon interacts directly, the anomalous component where the photon undergoes perturbative QCD processes and the vector-meson component where the photon fluctuates into a complex hadronic object that cannot be calculated by perturbative QCD.

It is possible to define a structure function F_2 for the photon based on its parton content in analogy to the proton:

$$F_2^\gamma(x, Q^2) = \sum e_i^2 (xq_i^\gamma(x, Q^2) + x\bar{q}_i^\gamma(x, Q^2)) \quad (1.12)$$

It describes the distribution of electric charge of the photon structure and can be constrained at e^+e^- experiments in DIS-like $\gamma^*\gamma$ reactions: the almost real γ , the probed photon, is radiated by the electron (or positron) scattered at small angle and the highly virtual photon γ^* , the probe, is radiated by the electron scattered at large angle. DORIS, PETRA, PEP, TRISTAN, LEP experiments contributed to the measurement of F_2^γ .

Similarly to the proton case, the parton density functions (pdfs) in the photon and DGLAP evolution equations are introduced. An additional term $a(x) = 3e_i^2 \frac{\alpha}{2\pi} [x^2 + (1-x)^2]$ enters the equation 1.8 to take into account the point-like component $\gamma \rightarrow q\bar{q}$. It is referred to as the 'inhomogeneous' term and makes F_2^γ rise at large x . The available models for the structure of the photon introduce pdfs at a low scale Q_0 depending on parameters. Fits of the pdfs to the measured F_2^γ are performed using DGLAP equations at LO or NLO to evolve the structure function in Q^2 .

The existing data on F_2^γ do not constrain much the gluon density in the photon. As for the proton, F_2^γ is directly related to the quark content and only indirectly to the gluon content. The data on F_2^γ are less precise than in the proton case and there is no momentum sum rule constraining the photon pdfs.

In jet production in $\gamma\gamma$ and γp scattering there is sensitivity to the gluon density of the photon and AMY, TOPAZ, TRISTAN $\gamma\gamma$ experiments already provided evidence for a non-zero gluon component ($qg \rightarrow qg$). At HERA more precise results were achieved.

1.4 Photo-production at HERA

The ep cross-section decreases strongly with Q^2 ($1/Q^2$ propagator term). For $Q^2 \approx 0$ the exchanged photons are almost real. We can then consider these events as γp scattering and speak of photo-production events. The electron behaves as a source of photons with energies in the range from zero up to the HERA electron energy of 27.5 GeV. The spectrum of the photon energies integrated to a maximal Q^2 , Q_{max}^2 , is given in the Weizsäcker-Williams approximation (WWA) [10] by:

$$f_{\gamma/e}(y) = \frac{\alpha}{2\pi} \left(\frac{1 + (1-y)^2}{y} \right) \ln \left(\frac{Q_{max}^2(1-y)}{m_e^2 y^2} \right) \quad (1.13)$$

Hard photo-production events contain particles with high transverse momentum P_T : a so-called hard interaction took place. The variable P_T can provide the renormalization scale for perturbative QCD calculations, replacing Q^2 which is used in DIS but is too small here. The factorization scale provides the frontier between the regions where perturbative QCD can be applied and the non-perturbative regions where the evolution ladder is described by the parton distributions.

There are two classes of photo-production. In the direct process the exchanged photon couples directly to the quarks of the proton (Fig. 1.8). In the resolved process the photon

fluctuates into a hadronic state as discussed in section 1.3 and a parton of the photon enters the hard interaction (Fig. 1.9). In this case there is a photon remnant which is not participating in the hard interaction, similar as in the case of the proton.

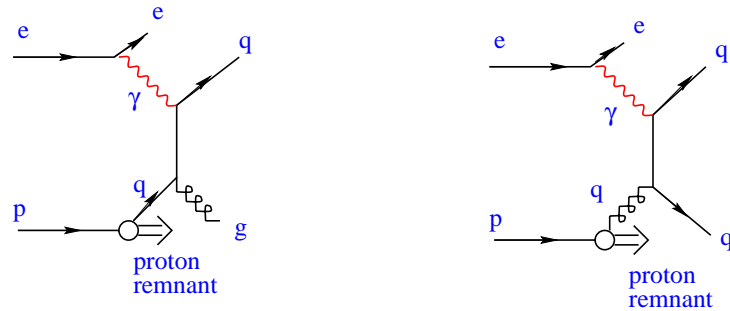


Figure 1.8: Feynman graphs of direct di-jets photo-production events

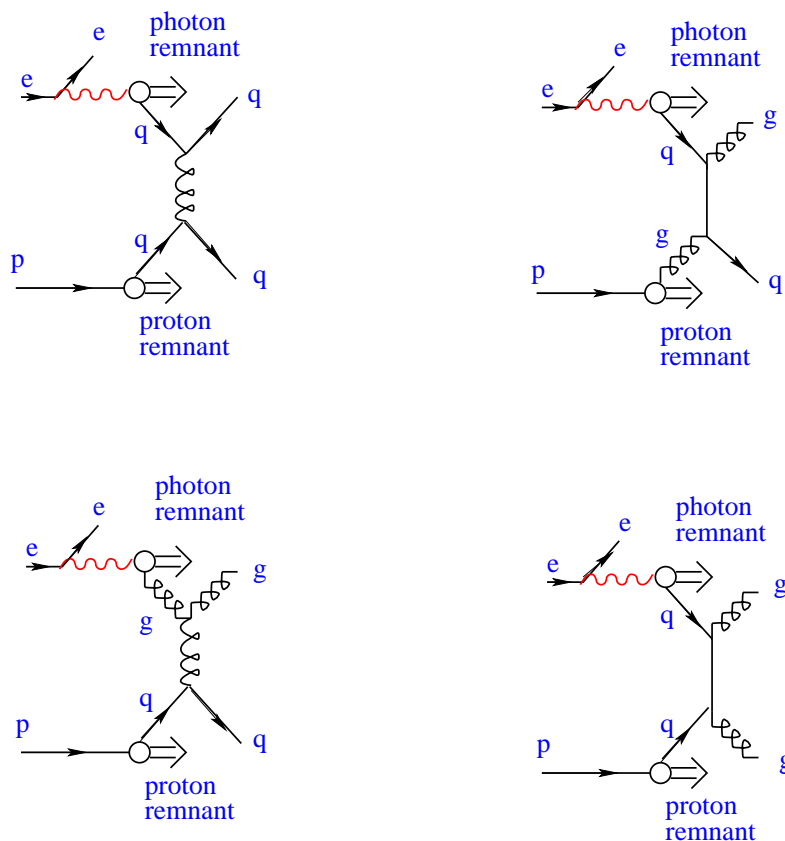


Figure 1.9: Feynman graphs of resolved di-jets photo-production events

Chapter 2

Prompt photon production

2.1 Prompt Photon Production in γp reactions

Prompt photon events have a photon in the final state produced in a hard interaction (see section 1.4), i.e. the experimental signature is a photon with substantial P_T . These photons have to be distinguished from photons produced via particle decays and, in ep reactions, also from photons emitted by the incident or scattered electrons. Figure 2.1 and 2.2 show examples of prompt photon diagrams at leading order with the direct component (Born diagram)

$$q\gamma \rightarrow q\gamma$$

and the resolved components

$$q^\gamma g^p \rightarrow \gamma q$$

$$g^\gamma q^p \rightarrow \gamma q$$

$$q\bar{q} \rightarrow \gamma g .$$

Parton fragmentation can also lead to a photon in the final state as shown in Figure 2.3(b)(d). For example the following di-jets processes have to be included when a prompt photon is appearing in the final state:

$$\gamma g \rightarrow q\bar{q}$$

$$\gamma q \rightarrow qg$$

The contributions of these different processes to the total prompt photon cross-section are presented in section 9.2.

Prompt photon measurements are free from some of the complications encountered in jet measurements such as the non perturbative hadronisation process, the jet identification and the jet energy measurement. The photon is directly measured in the detector. On the other hand the cross-section for prompt photon production is much smaller. The electromagnetic coupling constant α enters in the diagrams instead of the strong coupling constant α_s as for the jets.

The main experimental difficulty in the prompt photon measurement is a large background from neutral mesons.

Prompt photon production is sensitive to the parton structure of the proton and due to the resolved processes (see Fig. 2.2) also to the parton content of the photon. In particular it is directly sensitive to the gluon content of the photon, however with the presently available integrated luminosities this cannot seriously be constrained.

At HERA the gluon content of the photon can also be studied in the jet production analyses (see Fig. 1.8, 1.9) and in J/ψ production analyses in the reactions $\gamma p \rightarrow \text{jets } X$ and $\gamma p \rightarrow J/\psi X$.

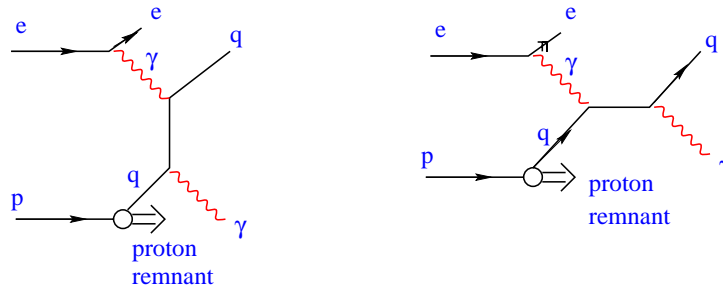


Figure 2.1: Example of direct prompt photon processes at leading order. The photon couples directly to a parton from the proton.

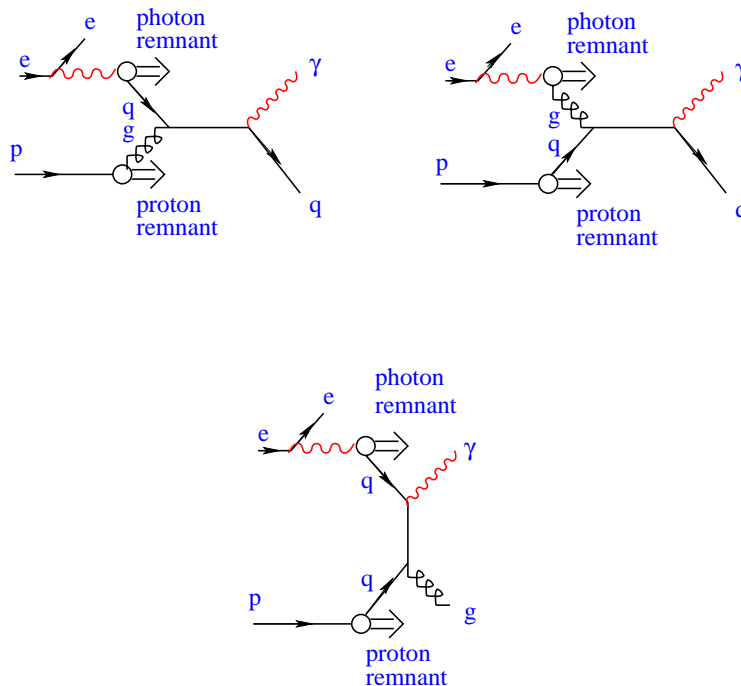


Figure 2.2: Examples of resolved prompt photon processes at leading order. The photon is resolved and a parton from the photon couples to a parton from the proton.

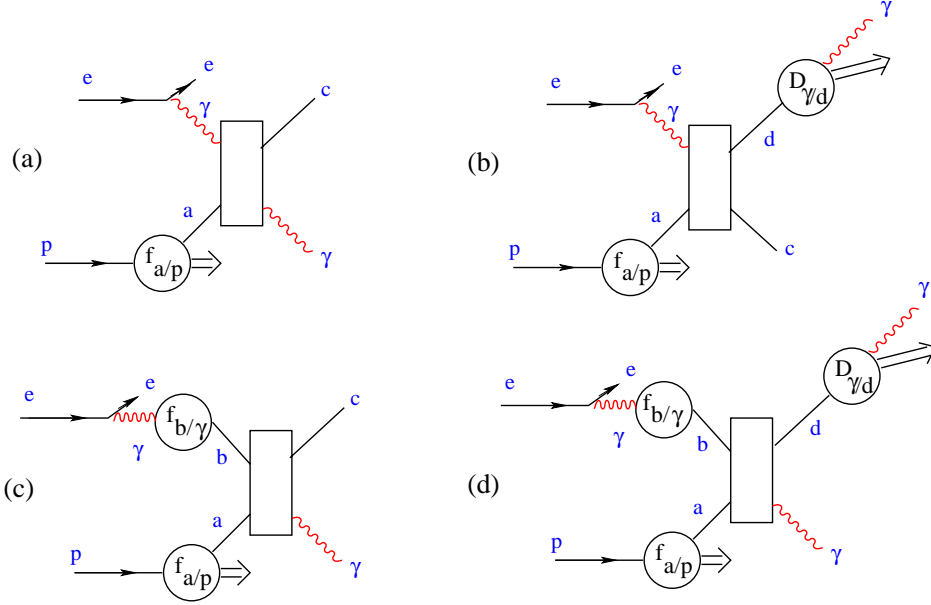


Figure 2.3: *Diagrams of the prompt photon production. The direct-direct (a), direct-fragmentation (b), resolved-direct (c) and resolved-fragmentation (d) processes are distinguished. The functions in the circles are defined in the text.*

The prompt photon cross-sections are given in leading order following [11] (see Fig. 2.3) by:

$$d\sigma_{dir}^{nonfrag} = \Sigma f_{a/p}(x_p, Q^2) \otimes f_{\gamma/e}(y) \otimes \sigma_{a\gamma \rightarrow \gamma+X} \quad (2.1)$$

$$d\sigma_{dir}^{frag} = \Sigma f_{a/p}(x_p, Q^2) \otimes f_{\gamma/e}(y) \otimes \sigma_{a\gamma \rightarrow d+X} \otimes D_{\gamma/d}(z, Q^2) \quad (2.2)$$

$$d\sigma_{res}^{nonfrag} = \Sigma f_{a/p}(x_p, Q^2) \otimes f_{b/e}(y) \otimes \sigma_{ab \rightarrow \gamma+X} \quad (2.3)$$

$$d\sigma_{res}^{frag} = \Sigma f_{a/p}(x_p, Q^2) \otimes f_{b/e}(x_e, Q^2) \otimes \sigma_{ab \rightarrow d+X} \otimes D_{\gamma/d}(z, Q^2) \quad (2.4)$$

Here $f_{a/p}(x_p, Q^2)$ is the probability that the proton p will produce a parton a carrying a fraction x_p of the proton's momentum.

The parton fragmentation function $D_{\gamma/d}(z, Q^2)$ gives the probability that the parton d will produce a photon γ carrying a fraction z of the parton's momentum.

The flux $f_{\gamma/e}(y)$ of the photon radiated by the electron e is given in the Weizsäcker-Williams approximation (see section 1.4) by

$$f_{\gamma/e}(y) = \frac{\alpha}{2\pi} \left(\frac{1 + (1-y)^2}{y} \right) \ln \left(\frac{Q_{max}^2(1-y)}{m_e^2 y^2} \right). \quad (2.5)$$

The probability $f_{b/e}(x_e, Q^2)$ that an electron e will produce a parton b carrying a fraction x_γ of the photon's momentum is:

$$f_{b/e}(x_e, Q^2) = \int_{x_e}^1 \frac{dy}{y} f_{\gamma/e}(x_\gamma, Q^2) f_{b/\gamma}(x_\gamma, Q^2). \quad (2.6)$$

Several NLO calculations for prompt photon production at HERA have been performed [12–14]. The most recent calculation [14] includes NLO corrections to all the leading order diagrams of figure 2.4: direct non-fragmentation (a), resolved non-fragmentation (b), direct fragmentation (c), resolved fragmentation (d). The box term also shown in figure 2.4 (e) is of order $\alpha^2\alpha_s^2$. The direct processes are of order $O(\alpha^2)$ (two electromagnetic vertices). The resolved processes are of the same order $O(\alpha^2)$ the hard subprocess being of order $O(\alpha\alpha_s)$ and the photon structure function of order $O(\alpha/\alpha_s)$. The fragmentation processes are also of the same order $O(\alpha^2)$ because the fragmentation function are of order $O(\alpha/\alpha_s)$. In the analysis discussed below the contribution of fragmentation is strongly suppressed by an isolation requirement for the photon (see section 6.4)

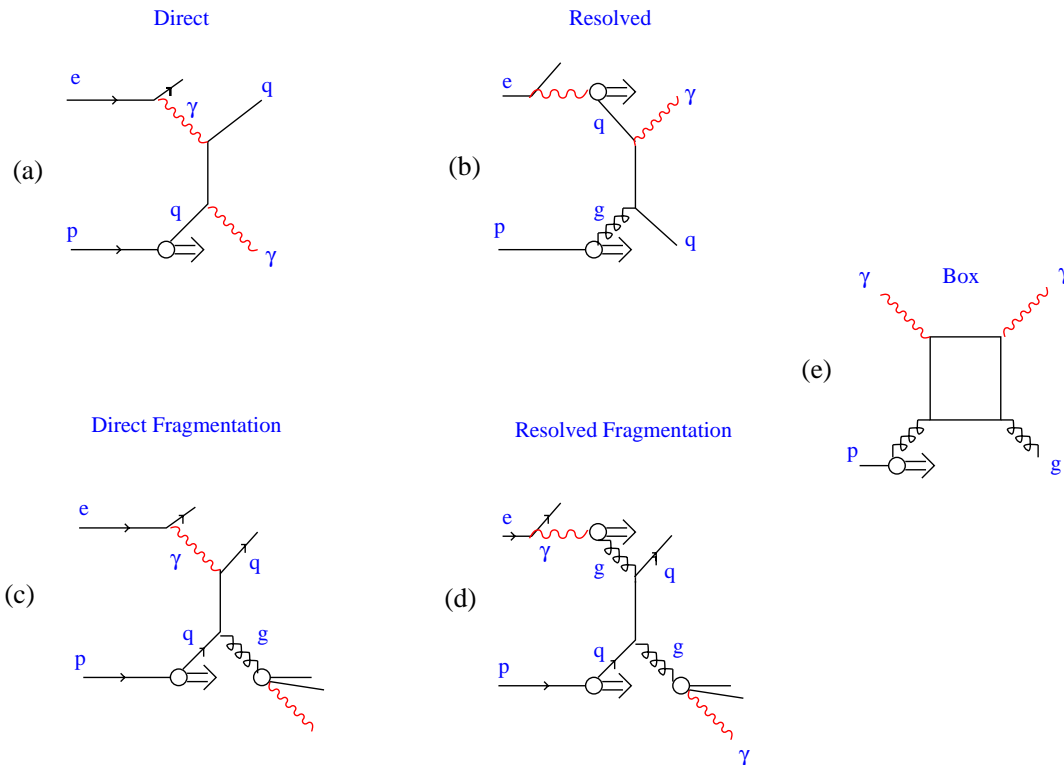


Figure 2.4: Diagrams of the prompt photon production. The direct-direct (a), resolved-direct (b), direct-fragmentation (c) and resolved-fragmentation (d) processes are distinguished. The box diagram (e) of order $\alpha^2\alpha_s^2$ is also shown

2.2 Previous experimental results

2.2.1 Prompt Photon at HERA

The latest published results from the ZEUS experiment were based on an integrated luminosity of 38.4 pb^{-1} using 1996 and 1997 data [15–18]. The cross-section is given as a function of the transverse energy E_T^γ (Fig. 2.5) and the pseudo-rapidity¹ η^γ (Fig. 2.6) for $E_T^\gamma > 5 \text{ GeV}$ and $-0.7 < \eta^\gamma < 0.9$ in the γp center-of-mass energy range 134–285 GeV. Comparisons were made with Monte-Carlo models based on leading order matrix elements and leading logarithm parton showers and also with next-to-leading order QCD calculations. Good agreement is observed for the E_T^γ distribution but for negative η^γ all predictions are below the data.

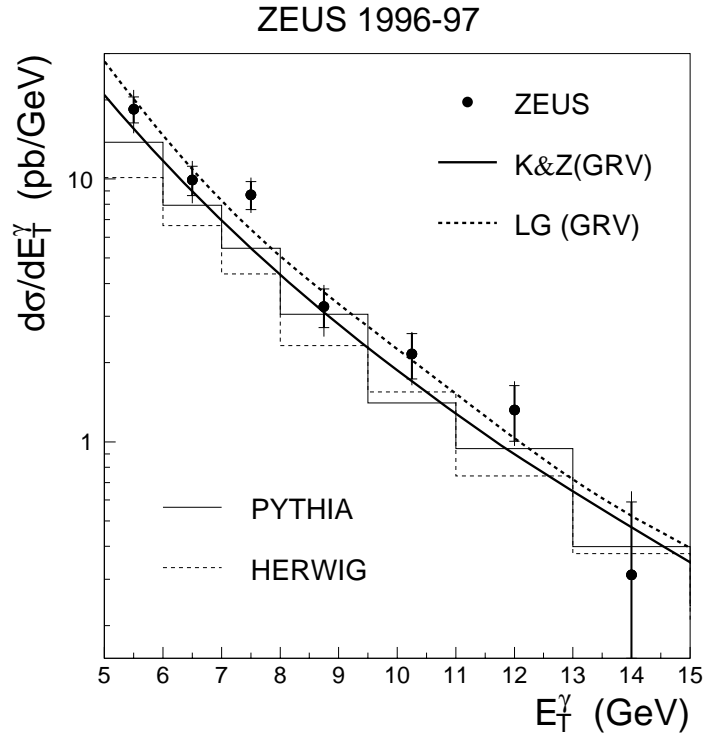


Figure 2.5: ZEUS E_T^γ distribution of the prompt photons in the phase space discussed in the text. The data points have been compared to the Monte-Carlo programs PYTHIA and HERWIG (see chapter 3) and next-to-leading order calculations.

The H1 experiment presented preliminary results [19] based on 7.9 pb^{-1} taken in 1996. A cross-section for prompt photon photo-production with $E_T^\gamma > 5 \text{ GeV}$ and $-1.2 < \eta^\gamma < 1.6$ of $104.8 \pm 5.9 \pm 15.7 \text{ pb}$ was measured in agreement with QCD prediction of 84 pb.

¹The pseudo-rapidity η is defined as $-\ln(\tan(\frac{\theta}{2}))$, where θ is the polar angle with respect to the proton beam direction.

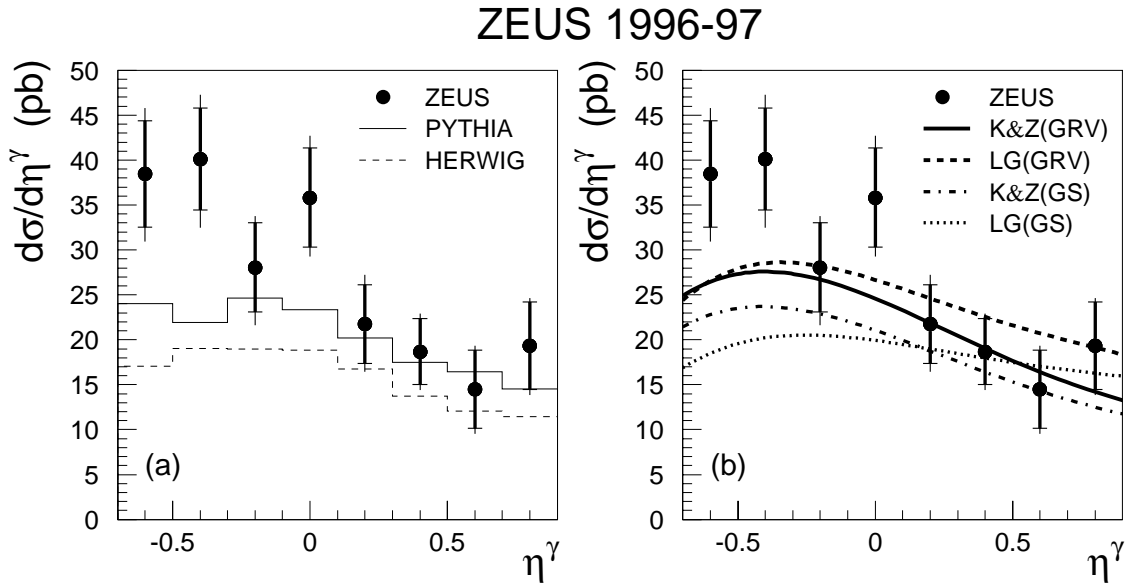


Figure 2.6: ZEUS η^γ distribution of the prompt photons in the phase space discussed in the text. The data points have been compared to the Monte-Carlo programs *PYTHIA* and *HERWIG* (see chapter 3) and next-to-leading order calculations.

2.2.2 Prompt Photons at other experiments

Table 2.1 shows a list of publications on prompt photon analyses. They have contributed to a better understanding of QCD.

In 1983 the E629 experiment at Fermilab provided an observation of prompt photons [23]. In 1985, NA14 disfavoured the gauge-integer-charge-quark model [24]. In 1988 NA24 [26] and WA70 [28] found evidence for the valence-quark-antiquark annihilation process. In 1998, OPAL [55] measured the quark-to-photon fragmentation function. Many prompt photon measurements helped constraining the gluon content of the proton in the early nineties, but recent results in many hadronic colliders cannot be explained by the present perturbative NLO QCD calculations (see e.g. [50, 51]).

Figure 2.7 shows a compilation [51] of results from hadronic experiments (i.e. using hadron beams). The results are presented as a ratio data/theory as a function of the reduced variable $x_T = 2E_T^\gamma/\sqrt{s}$. The fixed target experiments at CERN are WA70 analyzing the reactions π^+p and π^-p and UA6 analyzing the reactions pp and $\bar{p}p$. E706 is a π^-Be fixed target experiment at Fermilab. The pp collider experiments at CERN are R806, R807, R110 and CDF and DØ are $\bar{p}p$ experiments at the Tevatron. All experiments show the same feature. The x_T distribution predicted by the NLO calculation is less steep than the measurements.

This discrepancy may be explained by a large intrinsic transverse momentum k_t of the partons in the proton. The partons acquire this transverse momentum through radiation of soft gluons.

Experiments	Year	Reaction	Energy (GeV)	Location
R412	'76 [20]	pp	$\sqrt{s}=45,53$	CERN ISR
R107	'78 [21]	pp	$\sqrt{s}=53$	CERN ISR
R806	'82 [22]	pp	$\sqrt{s}=31,45,53,63$	CERN ISR
E629	'83 [23]	pC, π^+C	$E_{beam}=200$	Fermilab FNAL
NA14	'85 [24]	γLi	$E_{beam}=50-150$	CERN SPS
NA3	'86 [25]	pC, π^+C, π^-C	$\sqrt{s}=19.4$	CERN
NA24	'87 [26]	π^+C, π^-C	$E_{beam}=300$	CERN
WA70	'88 [27, 28]	pH, π^+C, π^-C	$E_{beam}=280$	CERN SPS
UA1	'88 [29]	$p\bar{p}$	$\sqrt{s}=546,630$	CERN $Spp\bar{S}$
UA2	'91,'92,'93 [30–32]	$p\bar{p}$	$\sqrt{s}=546, 630$	CERN $Spp\bar{S}$
UA6	'93,'98 [33, 34]	$pp p\bar{p}$	$\sqrt{s}=24$	CERN
CDF	'92,'93,'94,'02 [35–39]	$p\bar{p}$	$\sqrt{s}=630, 1800$	Fermilab Tevatron
D0	'96,'00 [40, 41]	$p\bar{p}$	$\sqrt{s}=630, 1800$	Fermilab Tevatron
E706	'99 [42]	pBe	$\sqrt{s}=32,39$	Fermilab
ALEPH	'91,'96 [43, 44]	e^+e^-	$\sqrt{s}=100$	CERN LEP
DELPHI	'92 [45]	e^+e^-	$\sqrt{s}=100$	CERN LEP
L3	92 [46]	e^+e^-	$\sqrt{s}=100$	CERN LEP
OPAL	'90,'91,'98 [47, 48, 55]	e^+e^-	$\sqrt{s}=100$	CERN LEP
H1	'97 [19]	ep	$\sqrt{s}=300$	DESY HERA
ZEUS	'97,'00,'01 [15, 16, 49]	ep	$\sqrt{s}=300$	DESY HERA

Table 2.1: List of experiments on prompt photon production, year of publication, the reaction studied, the center-of-mass energy \sqrt{s} or the beam energy for fixed target experiments, and the location.

Figure 2.8 shows how agreement with the data is achieved by introducing an ad-hoc higher $\langle k_T \rangle$. The value of $\langle k_T \rangle$ is fitted to give the best possible description.

The so-called resummed calculations [52, 53] try to compensate for the lack of real gluon radiation with respect to virtual gluon radiation arising from the energy cut-offs used for the numerical calculations. These resummed calculations are less scale dependent than NLO theory, but fail to describe the data. A more recent resummed calculation [54] taking into account the recoil of the parton after soft gluon radiation gives better results (Fig. 2.9). This subject is still under investigation.

The production of prompt photons was also studied at LEP by all four experiments. OPAL gave the first measurement of the quark-to-photon fragmentation function through the inclusive production of prompt photons in hadronic Z^0 decay [55].

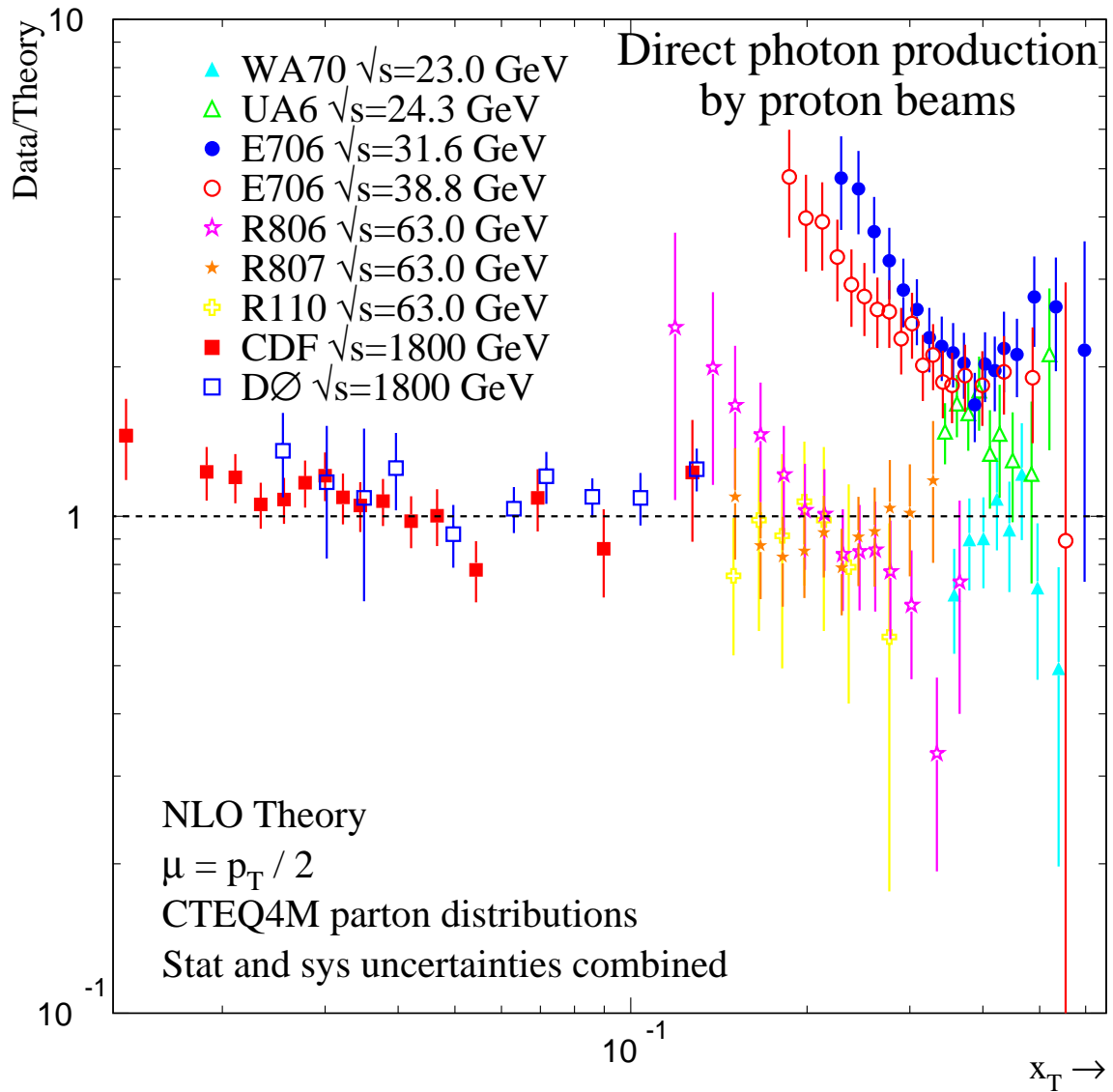


Figure 2.7: The data cross-section divided by the NLO prediction is shown as a function of $X_T = \frac{2E_T^y}{\sqrt{s}}$ for different prompt photon experiments.

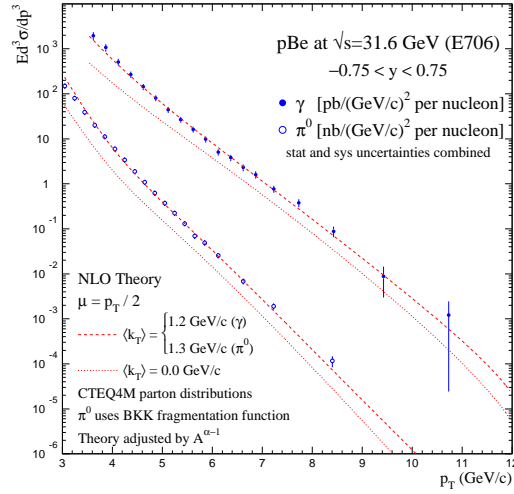


Figure 2.8: E706 prompt photon and π^0 inclusive cross-sections as a function of E_T for 530 GeV/c proton-nucleon interaction. It is compared to a NLO prediction without $\langle k_T \rangle$ (dotted) and with $\langle k_T \rangle$ enhancement (dashed). A value of $\langle k_T \rangle = 1.2$ GeV for the prompt photon and 1.3 GeV for π^0 data applied to the NLO predictions improves the data description.

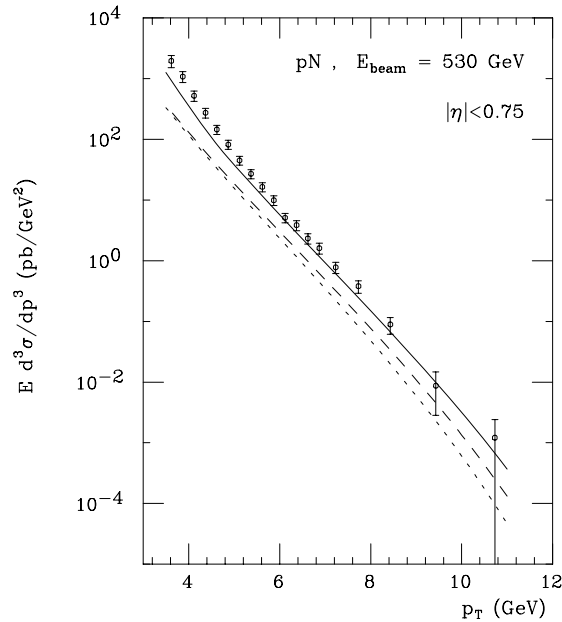


Figure 2.9: NLO calculation compared to E706 prompt photon results. The dotted lines represents the bare NLO calculation, while the dashed line incorporates resummation calculation and the full line both resummation calculation and recoil of the partons.

Chapter 3

Monte-Carlo simulation

3.1 Event Generators

The Monte-Carlo event generators used in this analysis simulate leading order hard sub-processes calculated by perturbative QCD and treat higher order effects by leading-logarithmic parton-showers as sketched in figure 3.1. They also include non-perturbative physics by the use of hadronisation models discussed below and parton density functions.

The events provided by the Monte-Carlo generators are put through the full H1-detector simulation. They are used to take account of the detector effects like acceptance and kinematic smearings and to determine the correction factors to be applied to the data in order to obtain the cross-sections at the hadron level.

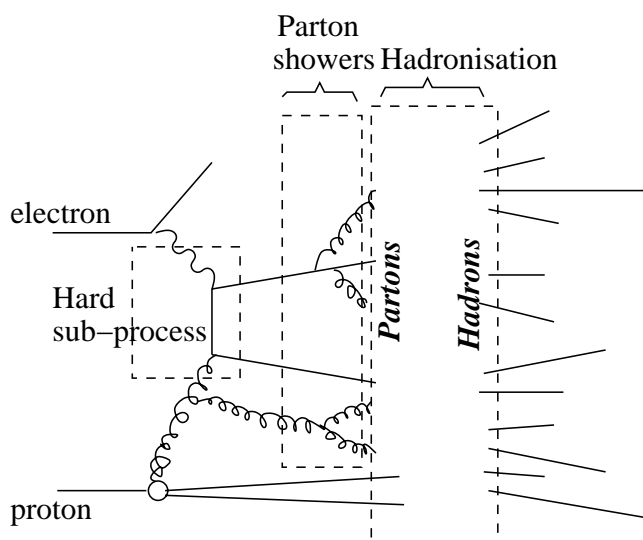


Figure 3.1: *The different components of a Monte-Carlo event generator: the hard subprocess, the partons showers and the hadronisation.*

3.1.1 Treatment of hadronisation

Because of colour confinement partons are not detected directly. Thus only colourless hadrons are observed in the final state and enter the detectors. In a first stage a shower of partons is produced using the Leading-Log approximation of QCD. The resulting partons are in a second stage converted into hadrons using non-perturbative models.

Lund string model

A simplified description of the Lund string model [56] is given. The coloured partons from parton showers are connected by a colour flux along a thin tube or a string of energy density $\sim 1 \text{ GeV} / \text{fm}$. As the partons move apart the string is stretched and its potential energy is increased. When the potential energy of the string is high enough to produce a $q\bar{q}$ pair it breaks up into two strings. If the energy of the fragments is high enough the process can be repeated and new $q\bar{q}$ pairs are formed. The process is repeated until only on-shell colourless hadrons remain. The figure 3.2 shows a simplified sketch of these different steps. The production of baryons is still poorly understood. In the simplest approach a string is also allowed to break into an antiquark-diquark pair.

The PYTHIA event generator [58] (see section 3.2) uses the Lund string model implemented in the JETSET program [57].

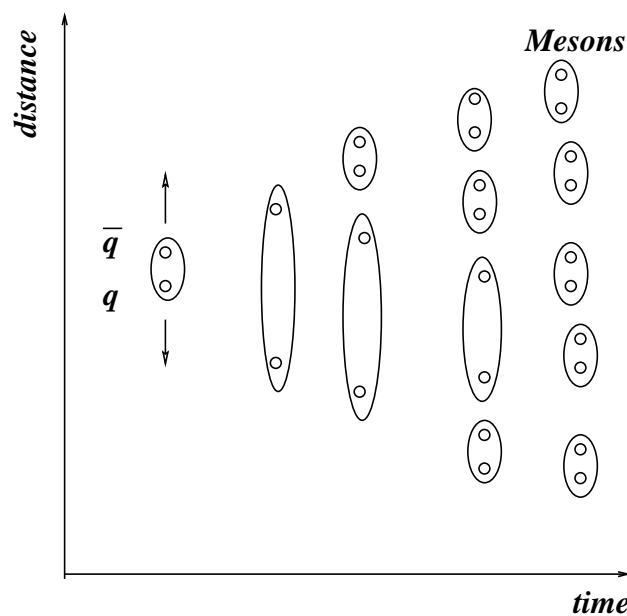


Figure 3.2: Simplified sketch of the breaking of a string into mesons used in the Lund hadronisation model.

Cluster model

In the cluster fragmentation model [64] the final state gluons obtained after parton showering are split into antiquark-quark pairs or antiquark-diquark pairs. Close enough quarks, diquarks, antiquarks or antiquarks are grouped to form colourless clusters. Heavy clusters are split into lighter clusters before all clusters decay into colourless hadrons. The cluster model is used in HERWIG [64] (see section 3.2).

3.1.2 Multiple interactions

Multiple interactions are implemented into the Monte-Carlo generators to take into account events where several parton-pairs (from the proton and the photon) undergo hard interactions. Experiments have shown that multiple interactions give rise to some energy flow that cannot be neglected e.g. [60]. In PYTHIA independent parton-parton scattering below the transverse momentum of the main partonic scatter are allowed down to some limit (1.45 GeV here). In HERWIG, multiple interactions are simulated by adding low P_T hadrons (the so-called soft underlying event SUE) to a fraction of the events. It has been tuned to the UA5 experimental results [64].

3.2 PYTHIA and HERWIG Monte Carlo Samples

The two Monte-Carlo models PYTHIA [58] and HERWIG [64] are used in this analysis. The generated events were put through the H1 detector simulation.

For PYTHIA, version 6.1 [63] was used in the ep interactions mode. It includes leading-order hard interactions, leading-logarithmic parton showers, parton distributions, initial and final state radiation, the Lund string fragmentation model (implemented in JETSET), multiple interactions and decay of the formed instable hadrons.

HERWIG (Hadron Emission Reactions With Interfering Gluons) version 5.1 [65] has been used. HERWIG has a detailed simulation of the QCD parton showers using a coherent showering algorithm applied to initial and final state radiation. The main difference to PYTHIA lies in the evolution of the parton showers, the hadronisation model used, and the treatment of multiple interactions (see also sections 3.1.1 and 3.1.2).

The GRV (LO) [61, 62] photon and proton structure functions were used for both event generators. The minimum P_T of the hard scatter was set to 3 GeV and the maximum Q^2 to 4 GeV. The intrinsic k_T of the partons in the proton was set to 1 GeV for the PYTHIA Monte-Carlo files.

Prompt photon processes

Figure 3.3 shows the processes generated for the prompt photon events. No fragmentation functions of partons-to-photons (see section 2.1) were used. However contributions from di-jet events where a quark radiates a high E_T photon are also included in the PYTHIA samples.

Samples of PYTHIA events without multiple interaction were also simulated for comparison.

The amounts of simulated prompt photon events with PYTHIA and HERWIG are summarized in tables 3.1 and 3.2.

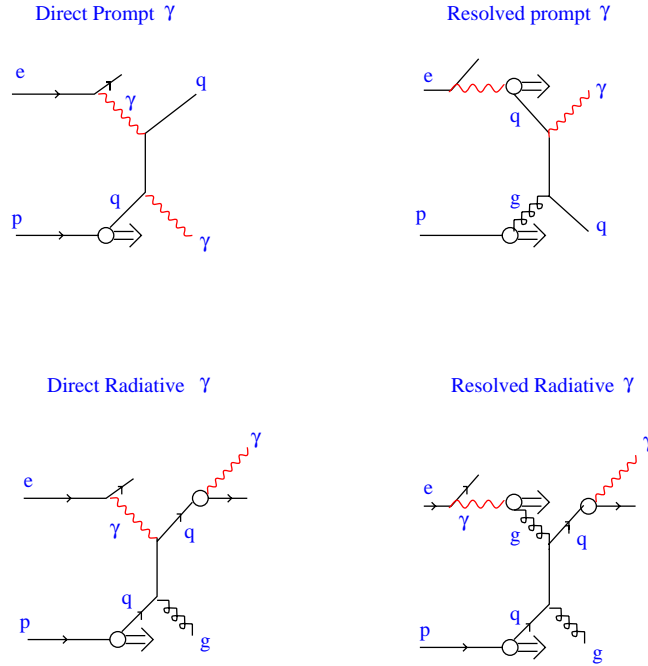


Figure 3.3: Example of graphs for prompt photon production as handled by PYTHIA and HERWIG: direct-direct (a) resolved-direct (b) (see section 2.1), and in addition the smaller contribution from di-jet graphs where a quark radiates a photon are included (c),(d) for PYTHIA only.

	Direct	Resolved	Direct radiative	Resolved Radiative
96	54.	70.	53.	56.
97	135	140.	127.	134.
98-99 e-	104.	94.	100.	83.
99 e+	130.	128.	120.	112.
2000 e+	312.	279.	299.	249.

Table 3.1: Integrated luminosities in pb^{-1} simulated with PYTHIA for the conditions of the different years of data taking for graphs contributing to the prompt photon signal.

	Direct	Resolved
96	57.	60.
97	132	137.
98-99 e-	102.	100.
99 e+	123.	133.
2000 e+	308.	303.

Table 3.2: Integrated luminosities in pb^{-1} simulated with HERWIG for the conditions of the different years of data taking for graphs contributing to the prompt photon signal.

Photo-production background processes

Di-jet events were also simulated to study the background from high P_T neutral mesons which may fake a photon signal in the detector due to the decay into photons according to:

$$\pi^0 \rightarrow \gamma\gamma (B.R. = 99\%), \eta \rightarrow \gamma\gamma (B.R. = 39\%), \eta^0 \rightarrow \pi^0\pi^0\pi^0 (B.R. = 32\%).$$

At high energies the granularity of the detector does not allow a separation of the produced photons, and a single cluster is observed in the detector faking a single photon.

Background calculations were performed using PYTHIA, but they have little influence on the final prompt photon results (see chapter 7). They are only used for comparisons and for the estimate of contamination due to η 's in proportion to π^0 's.

Due to the very large cross section of di-jets in photo-production, preselection cuts were applied for this background simulation already at the generator level. Events without a high P_T neutral particle (fake prompt photon candidate) fulfilling some isolation requirements are rejected. The isolation requirement is performed around the candidate in cones of radii R in the plane of pseudo-rapidity η and azimuth ϕ .

The following quantities are defined:

$$E_T^{cand} = \text{transverse energy of the fake prompt photon candidate}$$

$$E_{Tall}(R) = \sum_{r_i < R} E_T(\text{all particles } i)$$

$$E_{Tneutrals}(R) = \sum_{r_i < R} E_T(\text{neutral particles } i)$$

$$d_{charged} = \text{distance in } (\eta, \phi) \text{ plane of the closest charged particle to the candidate}$$

The following estimator defining the isolation of the neutral particle is used:

$$\text{For } d_{charged} > 0.7 : \text{estimator} = E_{Tneutrals}(0.1)/E_{Tall}(0.5)$$

$$\text{For } d_{charged} < 0.7 : \text{estimator} = (D_{charged}/0.7)(E_{Tneutrals}(0.1)/E_{Tall}(0.5) - 0.3)$$

The events are accepted if:

$$E_T^{cand} > 15 \text{ GeV}$$

$$\text{or } E_T^{cand} > 5 \text{ GeV and estimator} > 0.2$$

$$\text{or } 4 > E_T^{cand} > 5 \text{ GeV and estimator} > 0.3$$

PYTHIA Monte-Carlo di-jet samples of smaller integrated luminosity (132 pb^{-1}) without preselection at the generator level are also used to control the above selection. An inefficiency of less than 10% is obtained.

The background calculations showed that after the experimental cuts (see chapter 6) the background is composed of π_0 's (94%) and η 's (5%). The other sources of background are negligible (below 2% in total e.g. 0.4 % antineutrons).

	Direct	Resolved
96	52.	42.
97	126.	121.
98-99 e-	100.	98.
99 e+	120.	114.
2000 e+	299.	338.

Table 3.3: *Integrated luminosities in pb^{-1} simulated with PYTHIA for the conditions of the different years of data taking for graphs contributing to the hadronic jet background.*

Deep inelastic scattering background processes

To study the background contribution from DIS, events corresponding to 65 pb^{-1} of events were generated using the RAPGAP [66] event generator.

Single particles

Single particles (γ 's, π^0 's, η^0 's), in the liquid Argon calorimeter, with $4 < E_T < 15 \text{ GeV}$, were simulated. These are used in the prompt photon extraction procedure based on a shower shape analysis (see chapter 7).

Chapter 4

The H1 experiment at HERA

The H1 experiment is located in Hamburg at DESY (the Deutsches Elektronen Synchrotron laboratory) and is one of the two collider experiments at HERA (the Hadron Electron Ring Accelerator). Since 1992 it has collected data on electron-proton and positron-proton scattering over a wide kinematic range. In this chapter the HERA accelerator is shortly presented and the H1 detector [67, 68] is briefly described, in particular the components most relevant for this analysis.

4.1 The HERA accelerator

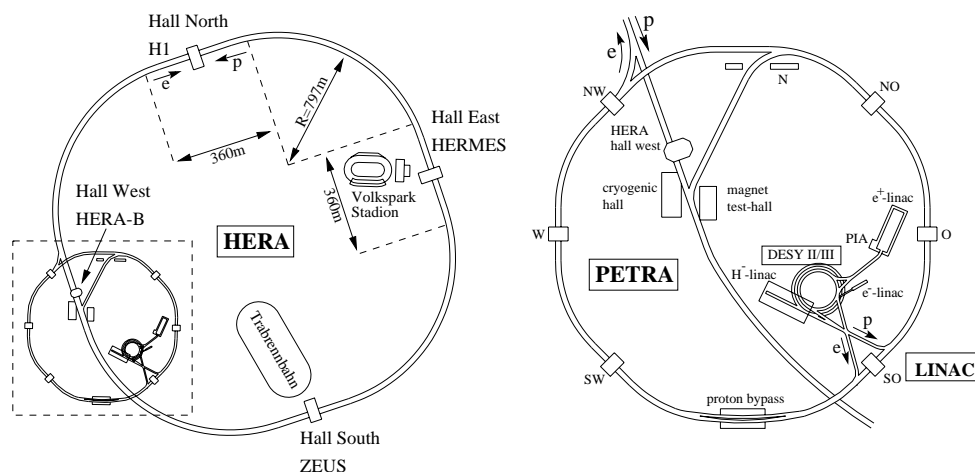


Figure 4.1: *The storage rings of HERA and the pre-accelerators.*

HERA is composed of two underground storage rings of 6.3 km circumference, one for electrons or positrons, the other for protons. Figure 4.1 shows an overview of the HERA accelerator and the pre-accelerators LINAC, DESY II/III and PETRA. The electrons are accelerated

to 27.5 GeV and the protons to 920 GeV (820 GeV before 1998). The center-of-mass energy of 320 GeV is one order of magnitude higher than reached at the previous electron-nucleon fixed target experiments. The other colliding experiment ZEUS is located diametrically opposite to H1. There are in addition two other experiments HERMES and HERA-B making use of only one beam (fixed target experiments). HERMES studies the collisions of polarized electrons on polarized nucleons of a gaseous target and HERA-B uses proton-nucleon scattering mainly to study B- physics.

Each beam is composed of a maximum of 210 particle bunches separated by 96 nanoseconds. The colliding proton and electron bunches are synchronized such that they collide within the H1 and ZEUS detectors. Pilot bunches are electron or proton bunches without corresponding partners in the opposite beam. Typically 10 pilot bunches are used to study the rate of interactions of the beams with the residual gas in the beam-pipe (beam gas interactions) or with the beam-pipe itself (beam wall interactions). The distribution of the interaction point or vertex is determined by the bunch lengths and is approximately Gaussian with a width of about 11 cm.

4.2 The H1 detector

The H1 detector is composed of many detector elements with different purposes situated around the interaction point of the colliding beams. It offers an almost 4π solid angle coverage, leaving out the regions of the entering and outgoing beams. The detector shows a backward forward asymmetry reflecting the different beam energies. A right handed set of Cartesian coordinates (x, y, z) is defined. The positive z direction is given by the direction of the proton beam. The x axis is directed toward the center of the HERA rings and the y axis points vertically upward. The polar angle θ is the angle with respect to the z axis so that $\theta = 180^\circ$ for an unscattered electron (see Fig. 4.2)

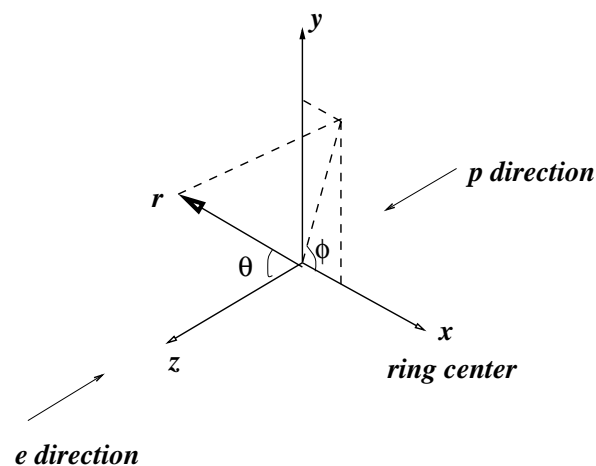
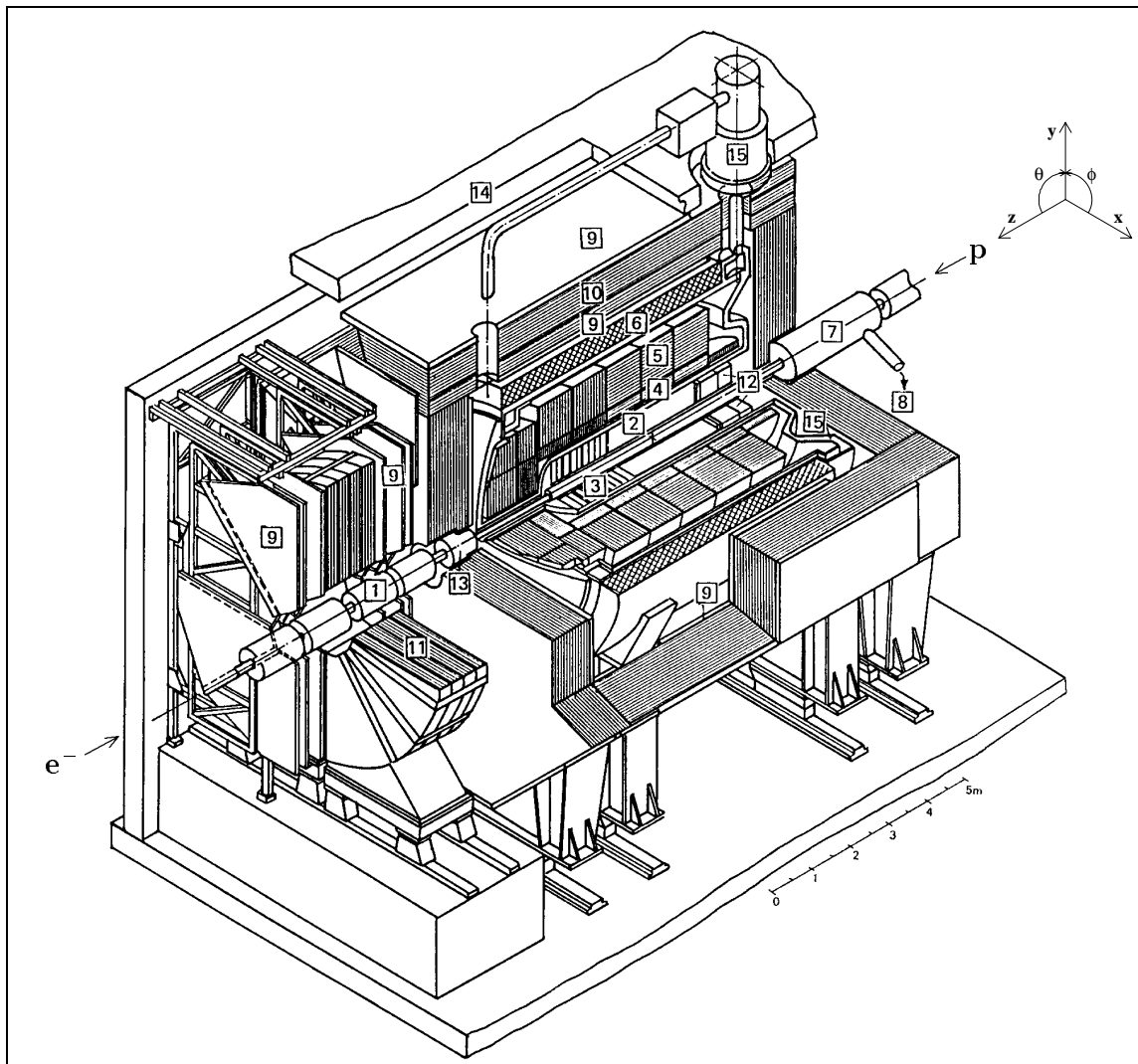


Figure 4.2: The definition of the Cartesian coordinate system (x, y, z) with respect to the e and p beam directions. The corresponding spherical coordinate system (r, θ, ϕ) is also shown.



- | | |
|--|--|
| 1 Beam pipe and beam magnets | 9 Muon chambers |
| 2 Central tracking device | 10 Instrumented iron yoke |
| 3 Forward tracking device | 11 Forward muon toroid |
| 4 Electromagnetic LAr calorimeter | 12 Backw. electromagn. calorimeter (BEMC) |
| 5 Hadronic LAr calorimeter | 13 PLUG calorimeter |
| 6 Superconducting coil (1.15 T) | 14 Concrete shielding |
| 7 Compensating magnet | 15 Liquid argon cryostat |
| 8 Helium supply for 7 | |

Figure 4.3: Schematic view of the H1 detector

A picture of the H1 detector is presented in figure 4.3. It shows, starting from the center of the detector, the tracking devices measuring the trajectories of charged particles, surrounding calorimeters to measure the energies of incident particles (e , γ , hadrons), the coil generating a longitudinal magnetic field of 1.15 Tesla, and the muon detectors.

4.2.1 The calorimeters

There are four calorimeters in the H1 detector (see Fig 4.3): The liquid Argon (LAr) calorimeter, the backward calorimeter SPACAL, the PLUG and the Tail Catcher“. The LAr calorimeter is used in the present analysis to identify the electromagnetic showers produced by the prompt photons. The PLUG calorimeter is in the forward region and covers small angles. The Tail Catcher allows to detect showers leaking out of the LAr calorimeter into the instrumented iron. PLUG and Tail catcher are not used in this analysis.

Electromagnetic showers

When a particle enters the calorimeter it produces a cascade of particles, a so-called shower. The Bethe and Bloch formula gives the energy loss $\frac{dE}{dl}$ mostly by ionisation depending on the nature of the particle and as a function some characteristics of the material being crossed.

For photons and electrons the cascade development is mainly through the reactions of photon conversion ($\gamma \rightarrow e^+ e^-$) and electron bremsstrahlung ($e \rightarrow e\gamma$) described by the Bethe-Heitler formulae [69], Except for the position of the first interaction, a photon shower is very similar to an electron shower.

The longitudinal development of an electromagnetic shower was already studied in 1952 by Rossi [70]. The depth l of an electromagnetic calorimeter is measured in units of radiation length X_0 . The number of particles increases first exponentially according to $N(l) = 2^l$. It reaches a maximum at a depth l_{max} which increases logarithmically with the shower energy E_0 . After l_{max} the ionisation losses get larger than the losses due to bremsstrahlung. The critical energy at which the two cross-sections are equal is $E_c \approx \frac{550\text{MeV}}{Z}$ where Z is the atomic number of the material. l_{max} is related to E_c by $l_{max} = \ln\left(\ln\frac{E_0}{E_c} - 0.5\right)$ for photons and $l_{max} = \ln\left(\ln\frac{E_0}{E_c} - 1\right)$ for electrons.

The mean longitudinal development of a electromagnetic shower for a particle of energy E_{inc} can be parametrised by the Longo-Sestilli empirical formula [71]:

$$\frac{dE}{dl} = E_0 \frac{\beta^\alpha}{\Gamma(\alpha)} l^{\alpha-1} e^{-\beta l} \quad (4.1)$$

where α and β are energy (E_0) dependent parameters.

The lateral development of a shower is determined by two phases [72]: in the first phase of the shower development the bremsstrahlung emissions and the other interactions occur at small angles. Therefore the shower begins with a small transverse radius. In the second phase, as the energies of the produced particles get lower the angles of emission get larger and the shower gets broader. The transverse shower profile distribution is the sum of two exponential components corresponding to these two phases. The scale describing the transverse shower

radius is the Molière radius R_m . It is the area of the cylinder containing 92% of the total energy of the shower:

$$R_m \approx \frac{21.2\text{MeV}}{E_c} X_0 \approx 7 \frac{A}{Z} \frac{g}{\text{cm}^2} \quad (4.2)$$

where A is the mass number and Z the atomic number of the material [73].

The Liquid Argon Calorimeter

The liquid Argon calorimeter [74] covers the polar angle range $\theta \in [4^\circ, 153^\circ]$. It is a sampling calorimeter using liquid Argon as active material and lead and stainless steel as absorber material in the inner and outer parts respectively. Electromagnetic showers are deposited in the inner lead/LAr part whereas hadronic showers penetrate also into the outer steel/LAr part. It is built out of different wheels (see Fig. 4.4): the Backward Barrel Electromagnetic calorimeter (BBE), the Central Barrel calorimeters (CB1, CB2, CB3), the Forward Barrel Calorimeters (FB1, FB2), the Inner and Outer Forward calorimeters (IF, OF). The wheels are composed out of eight octants (see Fig. 4.6). The ~ 45000 cells (see Figs. 4.5, 4.6) of the calorimeter ensure a good spatial resolution of the deposited energy.

The depth of the electromagnetic section is $\sim 20 - 30$ radiation lengths and the total depth of the calorimeter is $\sim 5 - 8$ interaction length. The resolution of the calorimeter determined at test-beam measurements is $\sigma_{em}(E)/E = 0.12/\sqrt{E/\text{GeV}} \oplus 0.01$ for electrons and $\sigma_{had}(E)/E = 0.5/\sqrt{E/\text{GeV}} \oplus 0.02$ for charged pions [75, 76].

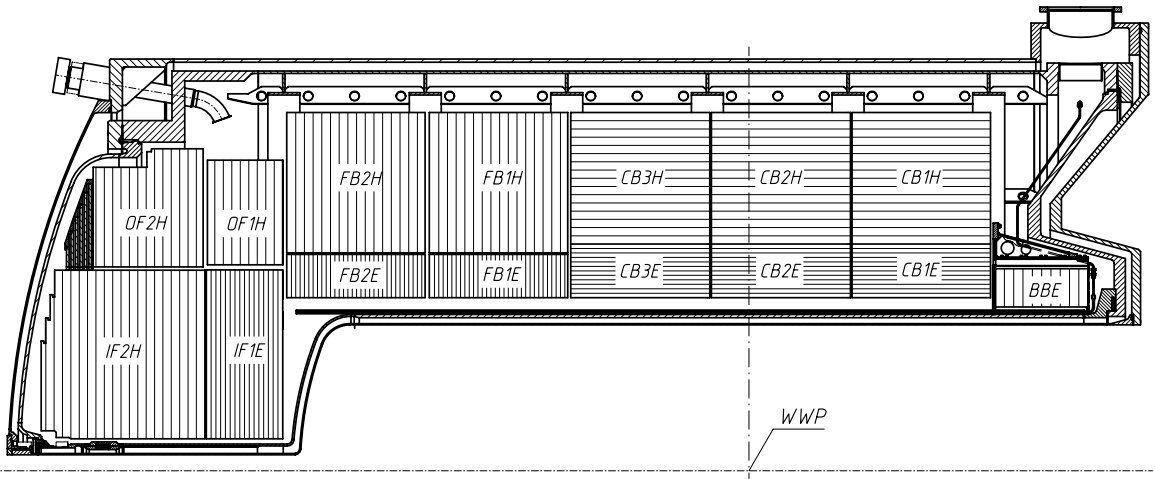


Figure 4.4: The different wheels of the inner and outer forward (IF,OF), central barrel (CB), backward barrel BBE calorimeters and their electromagnetic (E) and hadronic sections (H)

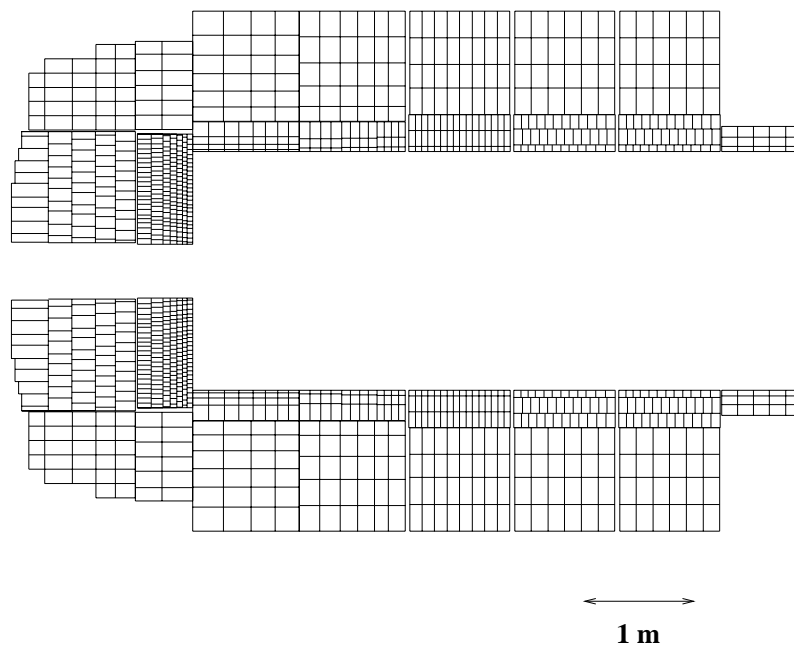


Figure 4.5: *Wheel and cell structure of the LAr calorimeter.*

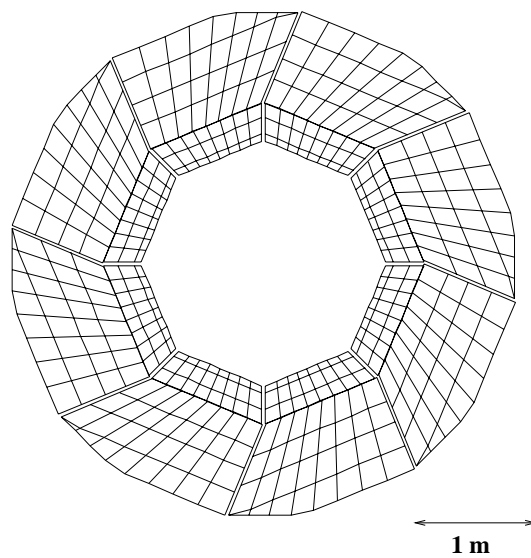


Figure 4.6: *Octant and cell structure of the CB1 wheel of the LAr calorimeter.*

The Backward Calorimeter: SPACAL

The SPACAL (Spaghetti Calorimeter) covers the polar angle range $\theta \in [153^\circ, 178^\circ]$. It is made of lead scintillating fibers and consists of an electromagnetic section and a hadronic section (described in detail in [77, 78]). A resolution of $\sigma(E)/E = 7.5\%/\sqrt{E/GeV} \oplus 2\%$ for the electromagnetic section and of $\sigma(E)/E \approx 30\%/\sqrt{E/GeV}$ for the hadronic section was achieved [79]. The hadronic section increases the depth from 1 nuclear interaction length λ (of the electromagnetic section) to 2λ in total. The main purpose of the SPACAL is to identify scattered electrons in DIS processes at low Q^2 ($Q^2 < 100 \text{ GeV}^2$). Its precise timing allows through a time-of-flight system to reduce the background from proton beam induced background. For this analysis it is used to measure the hadronic energies in the backward region.

4.2.2 The tracking system

Figure 4.7 shows a picture of the tracking system. It is composed of drift chambers, multi-wire proportional chambers (MWPC's) and silicon trackers around the beampipe.

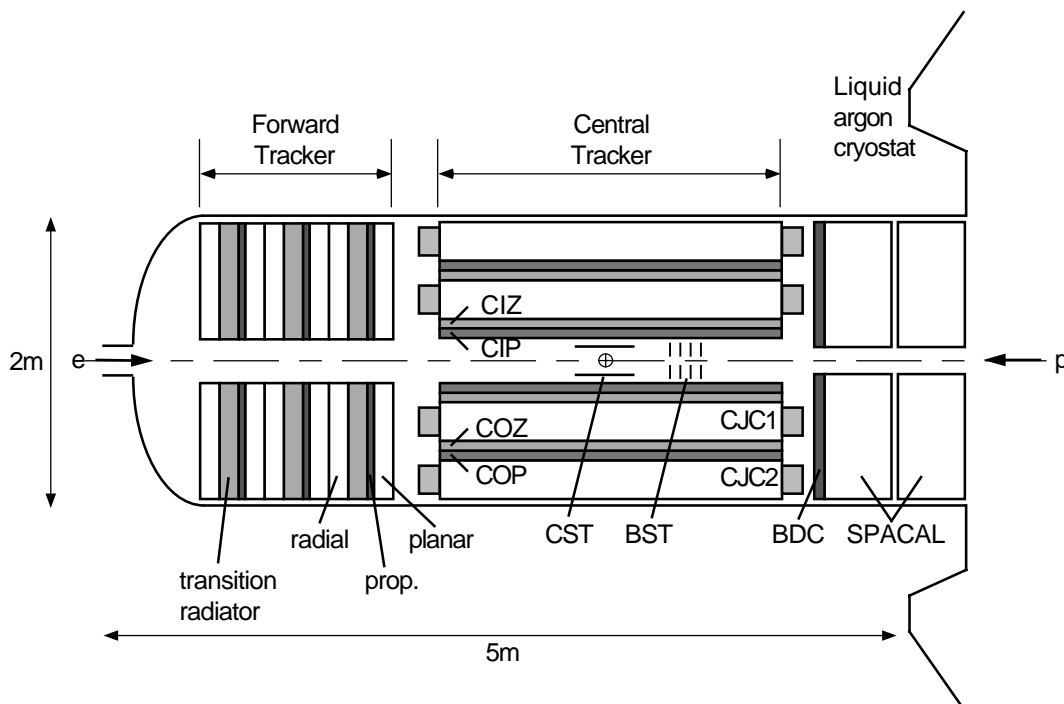


Figure 4.7: Schematic transverse view of the tracking system

Drift chambers

The drift chambers allow the reconstruction of the tracks left by charged particles. They consist of a set of anode sense wires surrounded by cathode wires organized in cells. A special gas mixture (e.g. Argon-Ethane-Isopropanol 48-52-1%) fills the chambers. When a charged particle crosses the chambers the gas is ionized and the released electrons drift in the electric field toward the sense wire while the ions drift towards the cathode. The typical drift length is a few centimeters. The increased field close to the anode wires leads to further ionisation and an amplification of the signal (avalanche of electrons and ions). This signal is further amplified before being digitized by a FADC (flash analogue digital converter). A particle leaves many such signals or hits along its trajectory. The drift velocity of the electrons and ions being known, a helicoidal trajectory or reconstructed track can be fitted to the set of hits.

MWPC's

The principle of multi-wire proportional chambers (MWPC's) is the same as that of drift chambers except that the distances between the anode wires and between these and the cathode wires or pads (a few mm) is much smaller. The direct time resolution is better than for the drift chambers because the amplification (avalanche) occurs immediately. On the other hand there is no drift time measurement and the spatial resolution is worse. Therefore drift chambers and MWPC's complement each-other in track reconstruction and triggering.

The H1 tracking system

The cylindrical central chambers CJC1 and CJC2 [80] cover the polar angle range $[25^\circ, 155^\circ]$ and are the main chambers used in this analysis. They are essentially of the same design. The sense wires are parallel to the z axis. Each cell is inclined by 30° with respect to the radial direction. Thus a particle crosses many drift cells facilitating the track reconstruction. The central inner chamber (CIZ) and the central outer chamber (COZ) are thin drift chambers improving the z resolution of the reconstructed tracks. CIZ is positioned inside CJC1 while COZ is positioned between CJC1 and CJC2. Two MWPC's, the central inner proportional (CIP) and the central outer proportional (COP) chambers improve further the spatial resolution of the tracks and are next to CIZ and COZ respectively. They are also used for triggering.

The forward track detectors FTD cover the polar angle range $\theta \in [7^\circ, 25^\circ]$ and consist of three identical supermodules each consisting of three planar chambers, a MWPC, a transition radiator and a radial chamber. The backward drift chamber (BDC) covers the polar angle range $\theta \in [153^\circ, 177^\circ]$.

The silicon trackers (CST, BST in Fig. 4.7) are not used in this analysis.

4.2.3 The Trigger System

The trigger system decides whether an event is to be kept or rejected. The rate of accepted and stored events is about 10 Hz. The trigger system identifies and selects events of interest and rejects beam-gas and beam-wall events which have a rate of 100 to 200 kHz depending on

the beam and vacuum quality. Figure 4.8 shows the different levels of decision making of the trigger system and the reduction of the rates from level to level. A compromise is made at each level between the available time for the decision making and the refinement of the analysis of each event necessary for a good decision making.

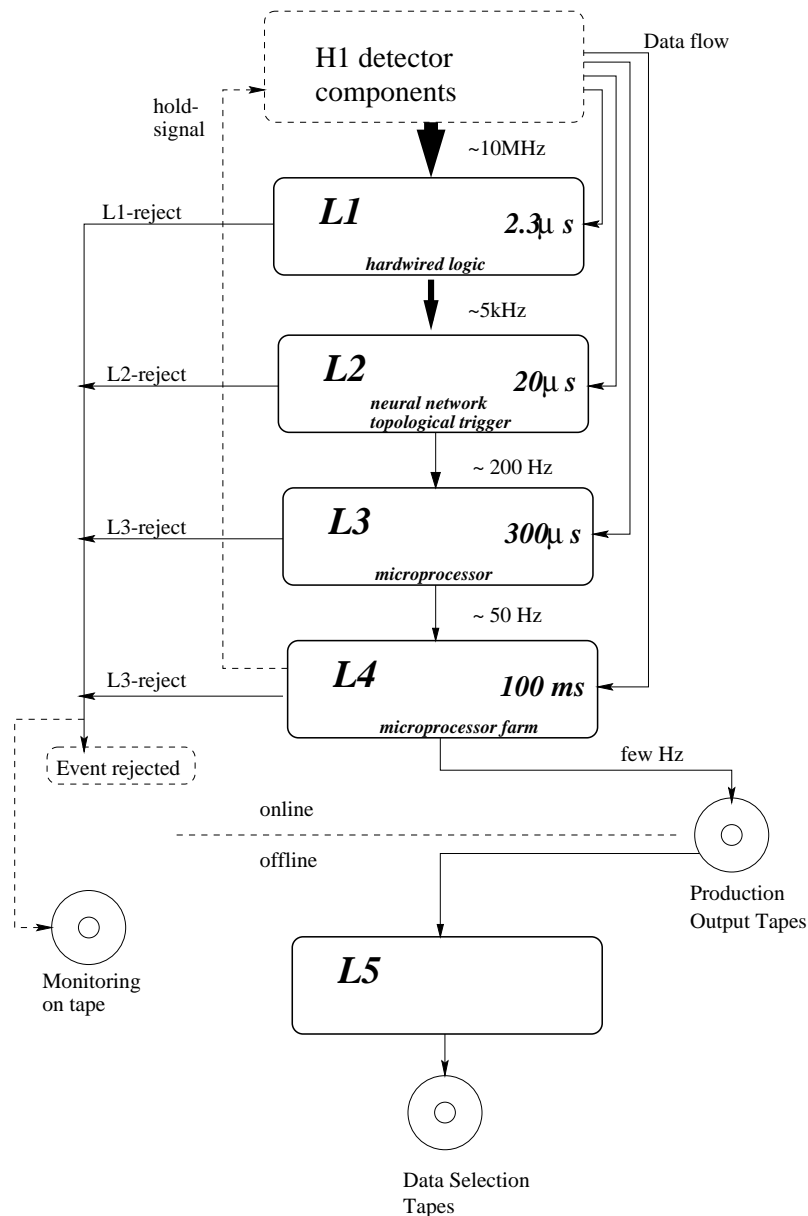


Figure 4.8: *The trigger system*

The level 1 (L1) trigger makes use of a set of signals (trigger elements) sent by the different components of the H1 detector. The 256 trigger elements are combined by boolean operations

to form 128 sub-triggers. It is only after 24 bunch-crossings ($2.3 \mu\text{s}$) that all the signals are ready to be combined and a pipeline is used to store the following events. If at least one sub-trigger is fulfilled an event is further transferred to the Level 2 (L2) trigger for further analysis. Here can occur dead-time losses as the following events are ignored until the trigger system has completely analyzed the event kept at L1.

The L2 trigger further reduces background rates. It takes the decision to keep an event or to reject it within $20 \mu\text{s}$. It makes use of the sub-triggers and of other trigger information coming from the detectors. It has two components: the topological trigger L2TT and the neuronal network trigger L2NN. L2TT makes use of a grid in (θ, ϕ) on which the signals are projected to discriminate against background events and to select events of interest. L2NN uses neural network algorithms applied to the information delivered by the detectors. When the L2 trigger accepts an event, the time consuming treatment (zero-suppression, digitization) of the information coming from the detectors starts.

The level 3 (L3) trigger was designed to further select events within $800 \mu\text{s}$ but was not yet available.

The level 4 (L4) trigger uses about 30 parallel micro-processors and the full information on the events to make a decision.

4.2.4 The luminosity system

The luminosity determination is based on the measurement of the event-rate of the Bethe-Heitler process: $ep \rightarrow ep\gamma$. The cross-section for this reaction is precisely calculable. The luminosity system consists of two crystal calorimeters, one situated at $z = -103\text{m}$ detecting photons and the other situated at $z = -33\text{m}$ detecting electrons. In the present analysis an integrated luminosity of 105pb^{-1} was used taken in the years 1996 to 2000.

4.3 Simulation of the H1 detector

The H1SIM program simulates the detector response to the generated Monte-Carlo events [86] based on the program GEANT [81]. On the basis of a detailed geometrical description of the detectors and the fields, GEANT gives for generated particles the deposited energies in the active material of the detectors. Normally the standard GEANT shower developments in the liquid Argon calorimeter are not used by H1 because of the long time of computation needed. A special parametrisation H1FAST [82, 83] is used instead. In the present analysis the original GEANT code is used to achieve a better description of the photon showers. Such detailed shower calculations have been successfully examined in measurements in test beams [75, 76]. Figure 4.9 and 4.10 show the lateral shower profile distributions for electrons respectively for pions obtained in these measurements. They are compared to the GEANT simulation before and after noise treatment (addition of noise and zero-suppression). The events simulated by H1SIM are further treated by the standard H1 reconstruction program H1REC which is also used for experimental data [68].

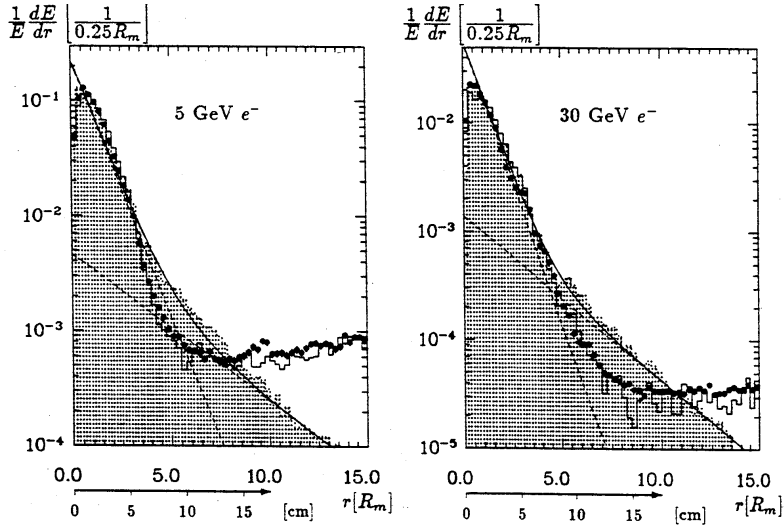


Figure 4.9: Lateral shower profile distributions for electrons in the electromagnetic inner forward part of the detector obtained in test beam measurement (points) for different energies. The histograms are the GEANT simulation before (dotted line) and after (full line) addition and zero-suppression of noise. The sum of two exponents is fitted to the GEANT results before noise treatment [84].

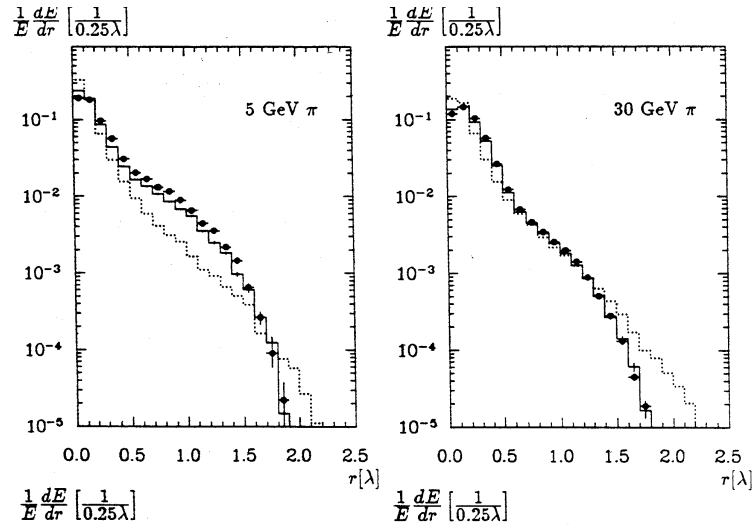


Figure 4.10: Lateral shower profile distributions for pions in the electromagnetic inner forward part of the detector obtained in test beam measurement (points) for different energies. The histograms are the GEANT simulation before (dotted line) and after (full line) addition and zero-suppression of noise [84].

Chapter 5

Reconstruction

Overview

This chapter is dedicated to the reconstruction of the prompt photon events. The prompt photons are detected in the central barrel of the liquid Argon calorimeter. It provides the energy and the scattering angle of the photon. An algorithm for finding and selecting photon-like showers is described. Also the determination of the variables characterizing the hadronic final state besides the prompt photon is presented. These variables are used together with the photon quantities to determine the inelasticity y and the γp center-of-mass energy $W_{\gamma p}$. The hadronic final state quantities are reconstructed using the clusters in the liquid Argon calorimeter and in the SPACAL and the tracks of the chambers avoiding double counting of energies. A variable characterizing the isolation of the prompt photons is based on the summation of the energies attributed to the tracks and clusters inside a cone surrounding the photon. As discussed in chapter 6 such an isolation requirement is performed to reject background originating from neutral mesons.

Jets are reconstructed using the inclusive k_T algorithm [90, 92]. This algorithm is used at detector level for the selection of jets. It can also be used at hadron level and parton level for theoretical calculations. The jet and photon quantities are used to calculate the fraction of the photon energy, x_γ , and of the proton energy, x_p , participating in the hard process (see chapter 2).

The LAr calorimeter alignment and the energy calibration for the relevant variables of this analysis are also discussed.

5.1 Photon reconstruction

5.1.1 Photon identification

Like electrons and positrons, photons produce compact and narrow showers in the LAr Calorimeter very different from the usually broad and deeply penetrating shower of hadrons. The identification of the prompt photon candidates is described here. It is based on a finder originally used for the identification of electron showers in deep inelastic scattering. A further step in the photon shower analysis is discussed in chapter 7.

Clustering and energy scale

The photon shower produces charges by ionisation in the liquid argon. These charges are collected in the calorimetric cells and converted by calibration factors into energies. The typical value of electronic noise (σ_{noise}) in a cells is 10 to 30 MeV. Only cells which have a neighbouring cell with energy above $4\sigma_{noise}$ are kept. The clustering algorithm [85] forms groups of cells corresponding to particle showers. It is tuned such that it identifies electromagnetic showers (electrons or photons) as single clusters. Hadronic showers are in general split into several clusters. Corrections are applied for the energy losses in dead materials (beam pipe, central tracker, inner cryostat wall) and in the cracks between the calorimeter stacks. These corrections were derived by Monte Carlo studies [67, 86].

Electromagnetic shower selection

The standard electromagnetic shower finder of H1 (QESCAT [87]) is used to select electron or photon candidates. It searches for the electromagnetic shower with the highest E_T fulfilling some shape and isolation criteria. An electromagnetic shower is distinguished from a hadronic shower by requiring that almost all its energy is deposited in the electromagnetic part of the liquid Argon calorimeter and only a small fraction of the energy is leaking in the hadronic part. Furthermore the shower is asked to be compact to distinguish it from the broader hadronic showers or showers produced by several particles close to each-other. The shower candidate is required to be isolated, aiming to reject candidates which are products of decays with accompanying particles. This isolation requirement is less harsh in QESCAT for candidates with low hadronic activity behind the electromagnetic shower. The shower is required in addition to be formed by a cluster of at least 3 cells. This ensures that the cluster is not the result of electronic noise.

More explicitly, QESCAT is based on estimators provided by the following cluster characteristics:

- Fraction of energy deposited in the electromagnetic section of the LAr: E_{em}/E_{cand} .
- Fraction of energy deposited in the cells of the core of the cluster: E_{core}/E_{cand} .
- Transverse dispersion: $\sigma_R = \sqrt{\langle r^2 \rangle - \langle r^1 \rangle^2}$
with $\langle r^n \rangle = \sum_{cells} w_i r_i^n / \sum_{cells} w_i$, $n = 1, 2$, where w_i are the energy densities of the cells i and r_i are the distances to the shower axis.
- Energy deposited in a cone starting from the interaction point around the axis of the candidate momentum of radius $R=0.25$ in the (η, ϕ) plane: $E_{(R=0.25)}$
- Energy deposited in the hadronic section of the LAr: E_{had} .

Table 5.1 shows the cuts applied on these estimators. The cuts on E_{had} and E_{em}/E_{cand} ensure that most of the energy is deposited in the electromagnetic part of the LAr calorimeter and not in the hadronic part. The cuts on σ_R and E_{core}/E_{cand} ensure that the shower is compact. The core of the cluster are four or eight contiguous cells depending on the calorimeter granularity including the cell of highest energy.

Estimators	cut value
$\frac{E_{em}}{E_{cand}}$	$> f_1(\theta) = 0.94 + 0.05\cos(2\theta)$
$\frac{E_{core}}{E_{cand}}$	$> f_2(\theta)$
$\sigma_R(cm)$	$< f_3(\theta)$
N_{cells}	> 3
$\frac{E_{cand}}{E_{(R=0.25)}}$	> 0.98 or > 0.95 and $E_{had} < 0.3$ GeV

Table 5.1: Cut description for photon shower identification. The $f_i(\theta)$ (see Fig. 5.1) are functions depending on the polar angle θ .

Figure 5.1 shows the cuts applied to the shower shapes as a function of the angle θ . It aims at a maximum rejection power against non-electron-like (or non-photon-like) showers keeping most of the electron-like (or photon-like) electromagnetic showers. The cuts are optimized by taking into account the differences in shower shapes as function of the angle θ . Indeed the cell structure of the calorimeter differs from wheel to wheel. For instance in wheel CB3 the cell segmentation in ϕ is twice as high as in wheels CB1 and CB2. Also the angle of penetration of the photons into the calorimeter has an effect on the shower shapes. For the regions between wheels (z-cracks) with exception of the transition from CB1 to CB2 no cuts are applied on $\frac{E_{core}}{E_{cand}}$ in order to keep as much electrons (or photons) as possible.

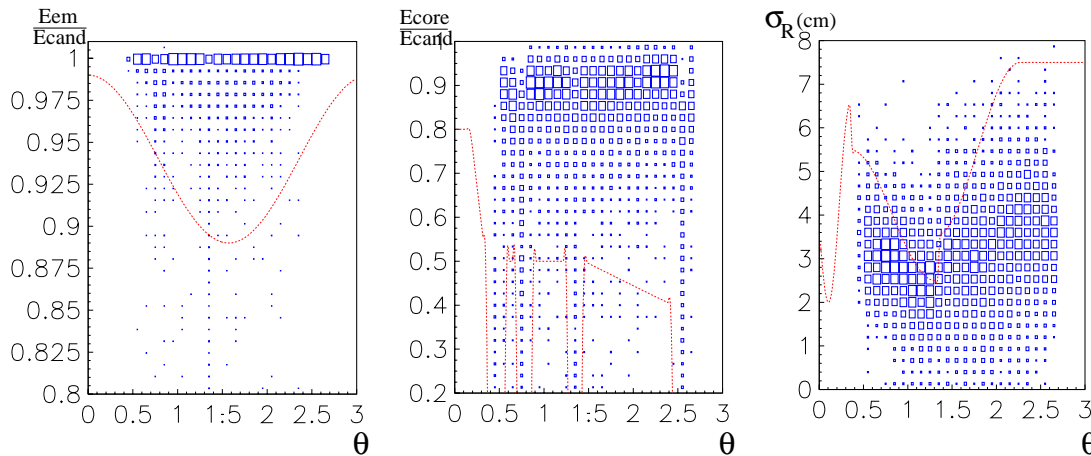


Figure 5.1: $\frac{E_{em}}{E_{cand}}$, $\frac{E_{core}}{E_{cand}}$ and σ_R (cm) as a function of θ (radians) for electrons simulated in the LAr calorimeter with E_T greater than 5 GeV. The functions $f_1(\theta)$, $f_2(\theta)$, $f_3(\theta)$ are also drawn (see table 5.1)

Efficiency of the prompt photon identification

The efficiency of the prompt photon identification using QESCAT is determined using the PYTHIA prompt photon Monte-Carlo samples. The efficiency is defined as the ratio of identified photons with all the requirements described above to the generated prompt photons. Figure 5.2 shows the efficiency as a function of the energy E^γ , the polar angle θ^γ , and the azimuth angle ϕ^γ . The z -cracks are the spaces between two wheels and the ϕ -cracks the spaces between two octants. They induce a drop of efficiency. The z -cracks correspond to the θ values of 25° (IF/OF-FB), 50° (FB-CB3), 80° (CB3-CB2), 120° (CB2-CB1). In the cracks the photons may penetrate up to the hadronic part of the calorimeter where they leave most of their energy and are then not identified as electromagnetic showers. An overall efficiency of about 90 % is achieved. This is to be compared with an overall efficiency of about 55% for π^0 's and of about 30% for η 's

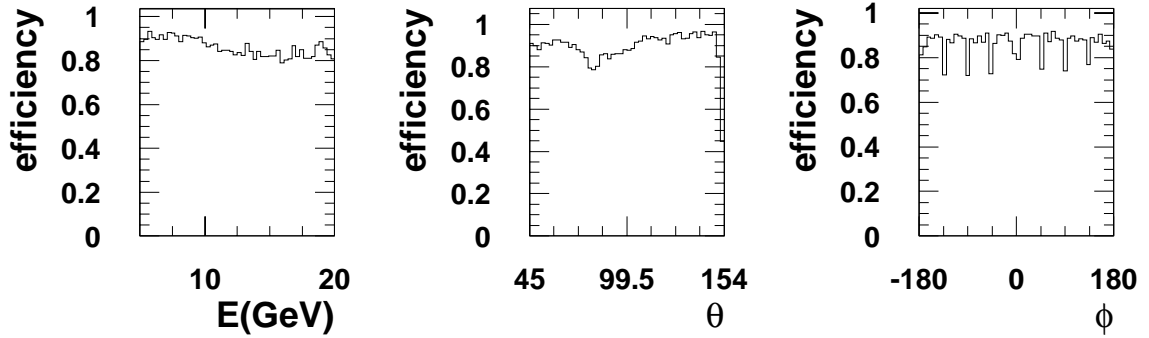


Figure 5.2: Efficiency of the QESCAT shower finder. The efficiency is shown as a function of the energy E^γ , the polar angle θ^γ in the range $[45^\circ, 154^\circ]$, and the azimuth angle ϕ^γ

A study of the QESCAT efficiency for electrons was performed in [89]. It uses an independent electron finder based on a cone jet algorithm of radius $R=0.5$. The efficiency of the photon finding for the data and for Monte Carlo samples was found to agree within 2%. The regions close to the cracks where the agreement gets worse (up to 5%) are cut out in the prompt photon analysis. A corresponding systematic error is applied to the final results.

5.1.2 Kinematic measurements

Calibration of the photon energy

The LAr calorimeter has originally been calibrated in test-beam measurements. Additional correction factors have been applied based on the data taken during ep running: electrons have been used in deep inelastic scattering where the measurements over-constrain the kinematics. The energy measured by the liquid Argon calorimeter have been calibrated [89] with respect to

the energy given by the so called double-angle method which uses angular measurements only and the primary electron energy:

$$E_{DA} = \frac{2E_e \sin \gamma_h}{\sin \gamma_h + \sin \theta_e - \sin(\gamma_h - \theta)}. \quad (5.1)$$

Here E_e is the energy of the incident electron, θ_e the electron angle and γ_h is the inclusive hadronic angle given by:

$$\tan\left(\frac{\gamma_h}{2}\right) = \frac{\sum_i (E_i - P_{z,i})}{\sqrt{(\sum_i P_{x,i})^2 + (\sum_i P_{y,i})^2}}. \quad (5.2)$$

The summations run over all particles i except the electron, E_i being the energy of the particle i and $P_{x,i}$, $P_{y,i}$, $P_{z,i}$ its momentum components projected along the axes x,y and z respectively.

A set of calibration factors have been determined as a function of the period of running, the wheels and octants of the calorimeter. The systematic errors on the calibration (electromagnetic energy scale uncertainty) depend on the number of electron events used. In the region used in this analysis it varies between 0.7% in the two backward wheels of the central barrel (CB1 and CB2) and 1.5% in the more forward wheel (CB3).

Figure 5.3 shows the effect of the calibration using the prompt photon PYTHIA Monte-Carlo sample. It shows the differences between generated and reconstructed E_T values of the prompt photons before ($\Delta E_{T(rec-gen)}$) and after ($\Delta E_{T(cal-gen)}$) calibration. These differences are also shown as a function of E_T^γ , η^γ and ϕ^γ .

Determination of the photon kinematic variables

The position and energy of the photon are determined using the LAr calorimeter. The high granularity of the cell structure allows a precise measurement of the center-of-gravity of the electromagnetic clusters.

The z impact position z_{imp} is obtained from the direction r of the cluster defined by:

$$\mathbf{r} = \frac{\sum_{cells} \sqrt{w_i} \mathbf{r}_i}{\sum_{cells} \sqrt{w_i}}. \quad (5.3)$$

w_i is here the energy density in the cell i and \mathbf{r}_i the unit vector given by the direction of a cell i from the event vertex. The position of the interaction point (vertex) differs from event to event by typically a few cm (see 6.5) due to the proton bunch length. It is determined from the trajectories of the outgoing particles measured in the tracking system. The photon angle θ^γ is obtained by the z impact position z_{imp} of the photon in the calorimeter and the position of the vertex z_{vertex} :

$$\theta^\gamma = \arctan\left(\frac{R_{cal}}{z_{imp} - z_{vertex}}\right), \quad (5.4)$$

where $R_{cal} = 105$ cm is the inner radius of the liquid Argon calorimeter. The pseudo-rapidity η^γ is then:

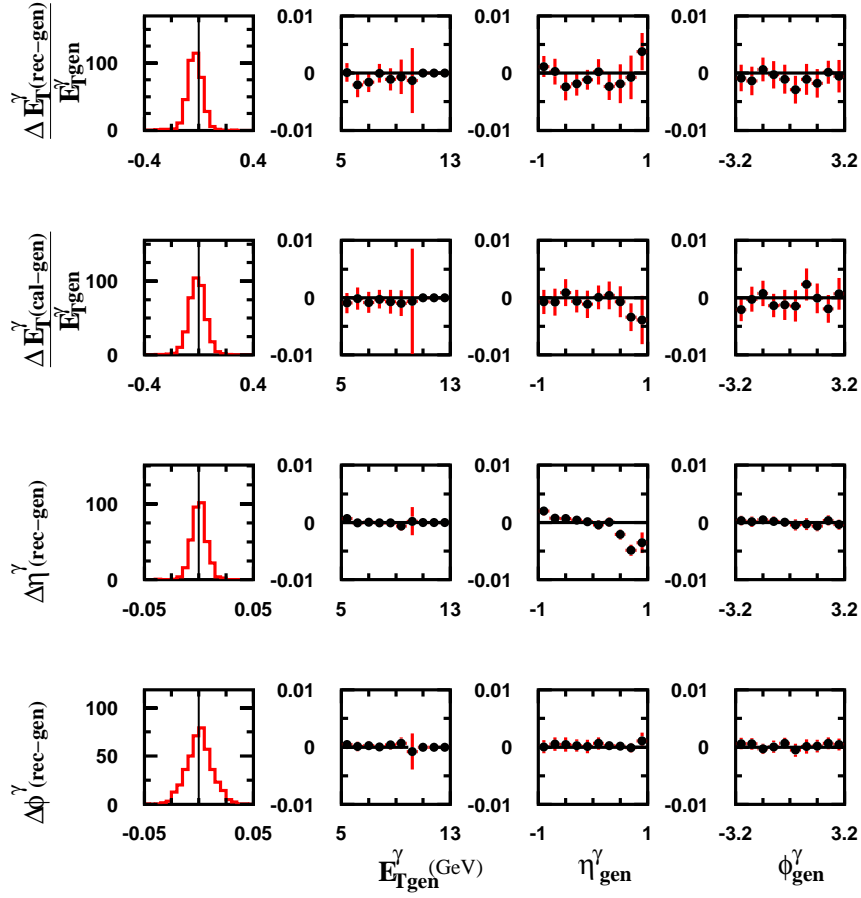


Figure 5.3: Resolution and possible bias for various variables using prompt photon Monte-Carlo events. The differences between generator and reconstructed values of pseudo-rapidity η^γ and azimuth angle ϕ^γ are shown. The true E_T^γ of the photons E_{Tgen} is compared to the measured E_T^γ before the Double-Angle calibration E_{Trec} and after E_{Tcal} . All the deviations are also given as a function of E_T^γ , η^γ and ϕ^γ .

$$\eta^\gamma = -\ln\left(\tan\left(\frac{\theta^\gamma}{2}\right)\right). \quad (5.5)$$

The transverse momentum E_T^γ (or P_T^γ) of the photon is given by

$$E_T^\gamma = E^\gamma \cdot \sin(\theta^\gamma). \quad (5.6)$$

To check the reconstruction, figure 5.3 shows the differences between generator and reconstructed values of pseudo-rapidity η^γ and azimuth angle ϕ^γ using prompt photon Monte-Carlo files. These differences are also shown as a function of E_T^γ , η^γ and ϕ^γ .

Calorimeter alignment

The exact calorimeter position was determined with respect to the tracking system using electron tracks and the corresponding showers in the calorimeter [89]. This method corrects for the difference between the expected position of the calorimeter from the design and the true position. These differences may arise from temperature contraction and small position and rotation shifts during the mounting of the detector.

5.2 Reconstruction of the hadronic final state

The reconstruction of the hadronic final state is described here. The calorimetric noise suppression and the combination of calorimetric clusters and tracks information are also used for other hadronic objects e.g. jets.

5.2.1 Hadronic final state measurement

The four-momentum of the hadronic final state is obtained using the tracking (forward and central trackers) and the calorimetric information $\mathbf{P}^{\text{clusters}}$ (liquid Argon and SPACAL). The four-momenta of the detector objects ($\mathbf{p}^{\text{tracks}}$ for the tracks and $\mathbf{p}^{\text{clusters}}$ for the clusters) are summed:

$$\mathbf{p}^{\text{tracks}} = \sum_{\text{tracks}} \mathbf{p}^{\text{tracks}} \quad \text{and} \quad \mathbf{p}^{\text{clusters}} = \sum_{\text{clusters}} \mathbf{p}^{\text{clusters}}. \quad (5.7)$$

The noise contribution $\mathbf{P}^{\text{noise}}$ is subtracted. The low energy isolated clusters with energies below 0.4 GeV (0.8 GeV) and isolated in a sphere of radius 40 cm (20 cm) for polar angles $\theta > 15^\circ$ ($\theta < 15^\circ$) are attributed to $\mathbf{P}^{\text{noise}}$ [88].

Double counting which may arise when the four-momenta of the tracks and of the clusters are added is avoided as follows [88]. The tracks with transverse momenta below 2 GeV are selected and extrapolated to the calorimeter surface. If the energy in a cylinder of radius 25cm for the electromagnetic section and 50 cm for the hadronic section is greater than that measured by the tracker the calorimetric energy is used. Otherwise the track momentum is used and the calorimetric energy is ignored. If a track does not reached the calorimeter the track momentum is used.

$\mathbf{p}^{\text{double counting}}$ is the sum of the four-momenta of the tracks or clusters that are ignored:

$$\mathbf{p}^{\text{double counting}} = \sum_{\text{ignored tracks and clusters}} \mathbf{p}^{\text{tracks and clusters}} \quad (5.8)$$

Thus:

$$\mathbf{p}^{\text{HFS}} = \mathbf{p}^{\text{clusters}} + \mathbf{p}^{\text{tracks}} - \mathbf{p}^{\text{double counting}} - \mathbf{p}^{\text{noise}} \quad (5.9)$$

This measurement of the four-momentum of the complete hadronic final state of an event is used in this analysis for the determination of the variable y using the Jaquet-Blondel method:

$$y_{jb} = \frac{E^{HFS} - P_z^{HFS} + E^\gamma(1 - \cos(\theta^\gamma))}{2E_e} \quad (5.10)$$

where E^{HFS} is the energy of the hadronic final state, P_z^{HFS} its momentum projected along z .

5.2.2 Hadronic energy scale of the Liquid Argon calorimeter

The Hadronic calibration is performed using neutral current deep inelastic scattering Monte-Carlo samples. It is based on the balance of the P_T of the hadronic final state and of the P_T of the calibrated electron (see previous section). Calibration constants are determined for each electromagnetic part and hadronic part of the different wheels separately. A precision of 2% on the hadronic energy scale is thus achieved. Figure 5.4 shows the correlation between the true y of the prompt photon Monte-Carlo events and the reconstructed y .

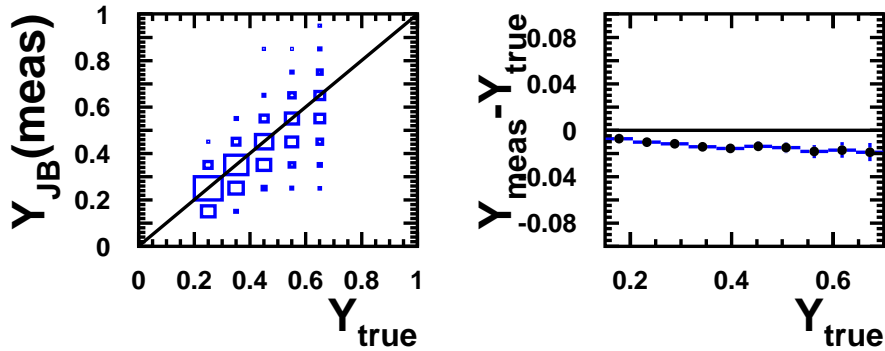


Figure 5.4: Correlation plots between true and measured y using PYTHIA prompt photon Monte-Carlo samples.

5.3 Jet reconstruction

During the hadronisation of the partons (see section 3.2) many colourless final state particles are produced. The intrinsic transverse momentum of these particles is given by the hadronisation scale, typically $\lesssim 1$ GeV. If the initial parton has high enough momentum with respect to this scale a collimated jet of hadrons results. The kinematic properties of these jets are correlated to those of the incoming partons. Jet algorithms are applied to the measured detector objects in order to find the jets and to compute their kinematics. In this analysis the tracker and the calorimeter objects (detector level) are used as described for the hadronic final state (see section 5.2.1). The jet finding is also applied to the generated hadrons in the Monte-Carlo simulations (hadron level). In next-to-leading order calculations the jets can be found before hadronisation (parton level). It is essential for the jet definition to have good correspondence between the different levels (parton, hadron and detector level). The jet k_T algorithm is presented below.

5.3.1 Jet k_T algorithm

The jet k_T algorithm [90, 92] is both collinear-safe and infra-red safe. Indeed, in the algorithm are two parallel particles equivalent to one particle with the sum of the momenta of the pair (collinear-safe) and the results of the algorithm are not much affected by addition of soft particles (infra-red safe). The corresponding requirement holds also for the detector level in view of the granularity of the detectors (resolution) and the presence of electric noise (small cell energies).

The algorithm works as follows:

- A distance d_{ij} is calculated for every pair of objects and d_i for each object:

$$d_i = E_{T,i}^2 \text{ and } d_{ij} = \min(E_{T,i}^2, E_{T,j}^2) R_{ij}^2 \quad (5.11)$$

with $R_{ij}^2 = \Delta\eta_{ij}^2 + \Delta\phi_{ij}^2$ and R_0 being a parameter set at 1.0, where $\Delta\eta_{ij}$ and $\Delta\phi_{ij}^2$ are the differences in pseudo-rapidity and azimuth with respect to the beam axis.

- d_{min} is defined as the smallest value of all d_i and d_{ij} .
- If d_{min} belongs to the set d_{ij} the two corresponding objects i and j are merged to a new object according to:

$$E_{Tij} = \sum_{k=i,j} E_{Tk}, \quad \eta_{ij} = \frac{\sum_{k=i,j} E_{Tk} \eta_k}{\sum_{k=i,j} E_{Tk}}, \quad \phi_{ij} = \frac{\sum_{k=i,j} E_{Tk} \phi_k}{\sum_{k=i,j} E_{Tk}} \quad (5.12)$$

and the particles i and j are removed from the list of objects.

- If d_{min} belongs to the set d_i , the object i becomes a jet and is removed from the list of objects.
- The procedure is repeated until all objects are removed from the list and only jets remain.

The kinematic variables E_T^{jet} , η^{jet} of the jets are obtained from equation 5.12. The transverse momentum P_T^{jet} of the jet is given by the vectorial sum of the transverse momenta of the objects forming the jet.

Figure 5.5 shows some correlations between jets at hadron level and detector level.

5.4 Reconstruction of further kinematic variables

The measurement of the photon variables transverse momentum E_T^γ (or P_T^γ), angle θ^γ , pseudo-rapidity η^γ and the jet variables transverse momentum P_T^{jet} , transverse energy E_T^{jet} and pseudo-rapidity η^{jet} , and the variable y have already been discussed in the previous sections.

The γp center of mass energy $W_{\gamma p}$ used to define the phase space of the prompt photon selection is given by:

$$W_{\gamma p} = \sqrt{y \cdot s}, \quad (5.13)$$

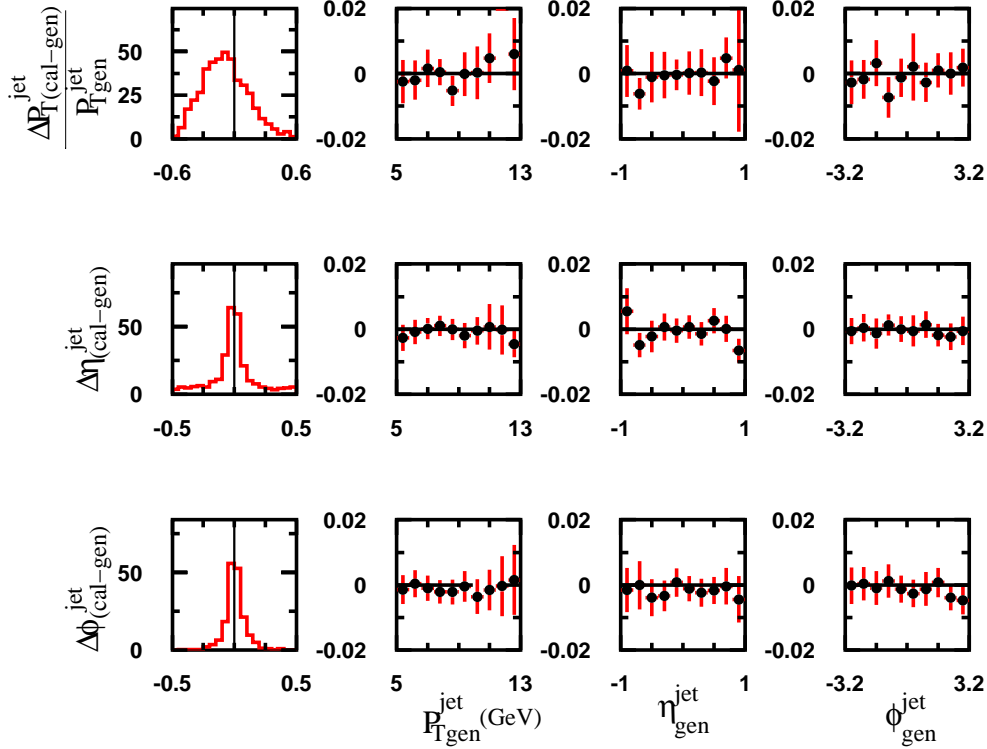


Figure 5.5: Difference between detector (*rec*) and generator (*gen*) level of P_T^{jet} , η^{jet} and ϕ^{jet} for PYTHIA prompt photon Monte-Carlo events. These differences are also shown as a function of P_T^{jet} , η^{jet} and ϕ^{jet} .

where \sqrt{s} is the center-of-mass energy of the electron-proton system. It is equal to 300 GeV for a 27.5 electron beam and a 820 GeV proton beam (before 1997 running conditions) and 320 GeV for 920 GeV proton beam (after 1998 running conditions).

The fraction of the primary photon momentum x_γ involved in the hard scatter leading to a jet and prompt photon in the final state is given by:

$$x_\gamma = \frac{E_T^{jet} e^{-\eta^{jet}} + E_T^\gamma e^{-\eta^\gamma}}{2yE_e}. \quad (5.14)$$

The fraction of the proton's momentum x_p involved in the hard scatter is given by:

$$x_p = \frac{E_T^{jet} e^{\eta^{jet}} + E_T^\gamma e^{\eta^\gamma}}{2E_p}. \quad (5.15)$$

A Lorentz invariant variable is defined to characterize the isolation of the photon candidate. A cone of radius 1 in the (η, ϕ) plane around the candidate cluster is considered. The distance of a particle i to the candidate in this plane is given by

$$R_{(\eta,\phi)}^i = \sqrt{(\eta^i - \eta^\gamma)^2 + (\phi^i - \phi^\gamma)^2}. \quad (5.16)$$

The transverse energy in the cone of radius $R(\eta, \phi) = 1$ around the candidate is defined as:

$$E_{T, cone}^{R(\eta,\phi)=1} = \sum_{R_{(\eta,\phi)}^{cells+tracks} < 1} E_T^{cells+tracks}$$

the sum being over all tracks and clusters of the liquid Argon calorimeter and SPACAL inside the cone, avoiding double counting as described in section 5.2, and not counting the candidate itself. The transverse energy fraction in the cone with respect to the candidate E_T^γ not counting the candidate itself is thus:

$$\frac{E_{T, cone}^{R(\eta,\phi)=1}}{E_T^\gamma} \quad (5.17)$$

Chapter 6

Event Selection

This chapter describes the final event selection for prompt photon production. The preselection cuts referring to the identification of the prompt photon showers in the liquid Argon calorimeter were discussed in section 5.1. Further cuts are applied to select prompt photon candidates and reject non- ep -background, Compton events, neutral current deep-inelastic-scattering events and neutral mesons in hadronic jets.

6.1 Data taking periods and run selection

The present analysis is based on the data taken during years 1996 to 2000. Table 6.1 shows the running conditions during this period.

Year	beams	beams energy	center-of-mass energy	integrated luminosity
1996-1997	e^+p	$E_e=27.5$ GeV $E_p=820$ GeV	$\sqrt{s}=300$ GeV	28.0 pb $^{-1}$
1998-April 1999	e^-p	$E_e=27.5$ GeV $E_p=920$ GeV	$\sqrt{s}=320$ GeV	16.3 pb $^{-1}$
May 1999-2000	e^+p	$E_e=27.5$ GeV $E_p=920$ GeV	$\sqrt{s}320$ GeV	57.8 pb $^{-1}$

Table 6.1: *The used beams, the beam energies, the center-of-mass energies and the integrated luminosities are shown for the different years.*

The data taken during one filling of electron or positron and proton bunches ("luminosity fill") is divided into so-called runs. Different runs may have different detector conditions. The integrated luminosity is determined for each run. The runs are excluded when the sub-detectors necessary for this analysis are not operational, namely the luminosity system, the time-of-flight system, the liquid Argon calorimeter, the SPACAL, and the central jet chambers. In addition the triggers used in the analysis have to be enabled.

6.2 Photon fiducial volume cuts

Candidates for which $E_T^\gamma > 5$ GeV and $-1 < \eta^\gamma < 1.5$ are selected. The lower cut on E_T is determined by the trigger efficiency. The cut on η^γ is to ensure that the photon goes through the central tracker and a cluster-track link veto can be done properly. Also a prompt photon+jet sample is selected (see in chapter 9). Figure 6.1 shows an example of a prompt photon event with a well isolated γ candidate.

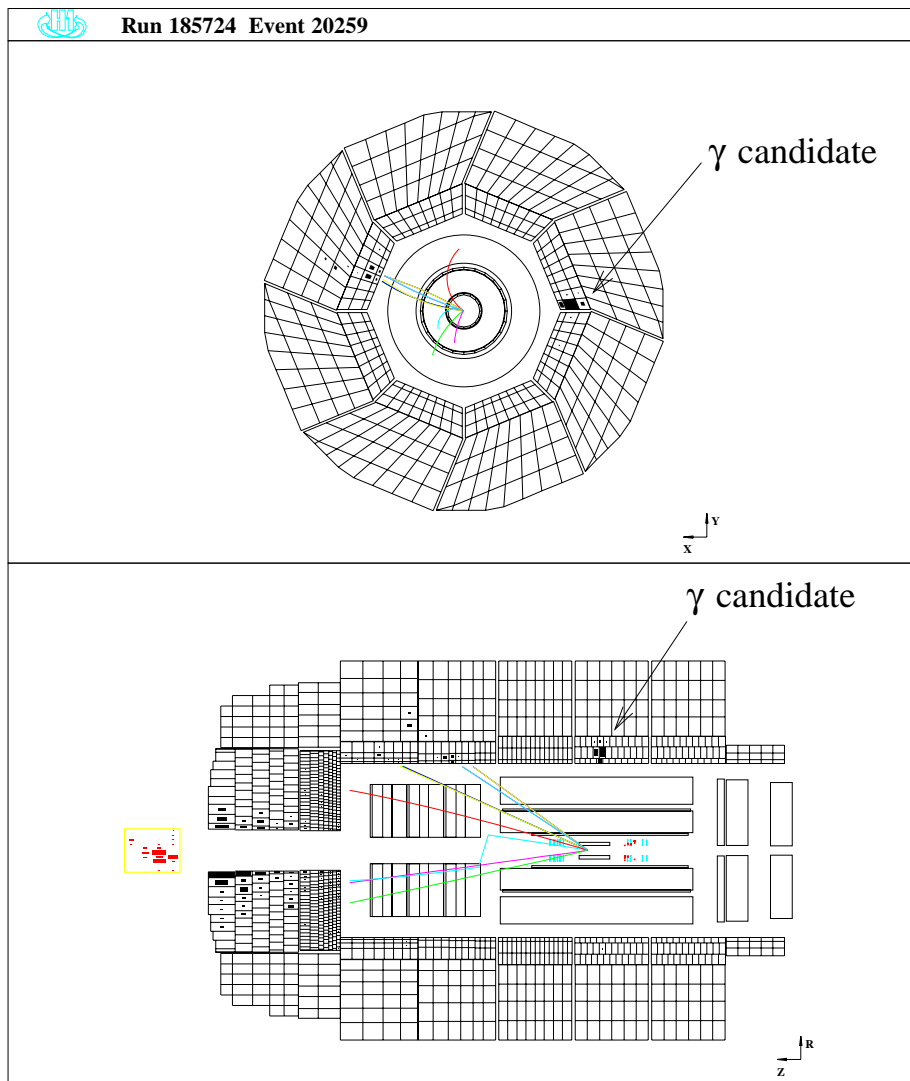


Figure 6.1: *Prompt photon candidate. Proton beam from right, e^+ beam from left.*

6.3 Triggering

The triggering of the prompt photon events is based on the requirement of an energetic compact electromagnetic cluster in the liquid Argon calorimeter. The global H1 trigger system is described in section 4.2.3. The level 1 sub-trigger used in this analysis is described here. The prompt photon events passing the level 1 requirement do not suffer further selection at the other trigger levels (levels L2 to L4) of the trigger system.

Level L1 Sub-trigger

The level L1 sub-trigger *ST67* is used. The requirement of an energetic compact electromagnetic cluster in the liquid Argon calorimeter is performed by the trigger-element:

- *LAr-electron-1*.

Other trigger elements enter the subtrigger *ST67*, namely the *T0* trigger elements:

- *LAr-T0*: the timing information of the liquid Argon calorimeter
- *Ray-T0*: the timing information of the central and forward proportional chambers.

Their aim is to ensure that the event took place during the bunch-crossings. They reduce thus non-*ep*-events (see section 6.4) where the timing *T0* of the sub-detectors is not synchronised with a corresponding bunch crossing time.

The trigger-elements are combined to form the sub-trigger *ST67* according to:

$$ST67 = (LAr - electron - 1) \text{ and } ((Ray - T0) \text{ or } (LAr - T0))$$

Events which have been triggered by *ST67* are selected.

Trigger Efficiency:

Energy thresholds are applied to *LAr-electron-1*. The efficiency of the triggering decreases with the energy of the photon candidates. For the determination of the trigger efficiency another sub-trigger (*ST71*) based on independent conditions is used as monitor trigger (MT). The data used are a selection of neutral current deep inelastic events where the electrons are detected in the LAr calorimeter.

The efficiency is given by the fraction of events triggered by *ST67* for a sample of events triggered by the MT:

$$\varepsilon = \frac{\text{number of events triggered by MT and ST67}}{\text{number of events triggered by MT}} \quad (6.1)$$

In some regions the thresholds of *LAr - electron - 1* are set to higher values than normal due to electronic noise. Fiducial cuts are applied yearwise to remove regions where the trigger efficiencies are poor. The trigger efficiency $\varepsilon_{z,\phi}$ is computed as a function of the impact position z and of the azimuth ϕ for energies greater than 5 GeV. Ideally, the trigger efficiencies should only depend on z and not on ϕ . Figure 6.2 shows, for the example of year 2000, the trigger efficiency as a function of z and ϕ . Only these regions are accepted where the efficiency is more than 90 % of the efficiency of a z -bin averaging over ϕ .

Figures 6.3 and 6.4 show the trigger efficiencies as a function of the energy of the cluster for different pseudo-rapidity bins after applying the fiducial cuts. For years 1996 and 1997, where the trigger thresholds were higher, a cut at $E_T > 7$ GeV is applied.

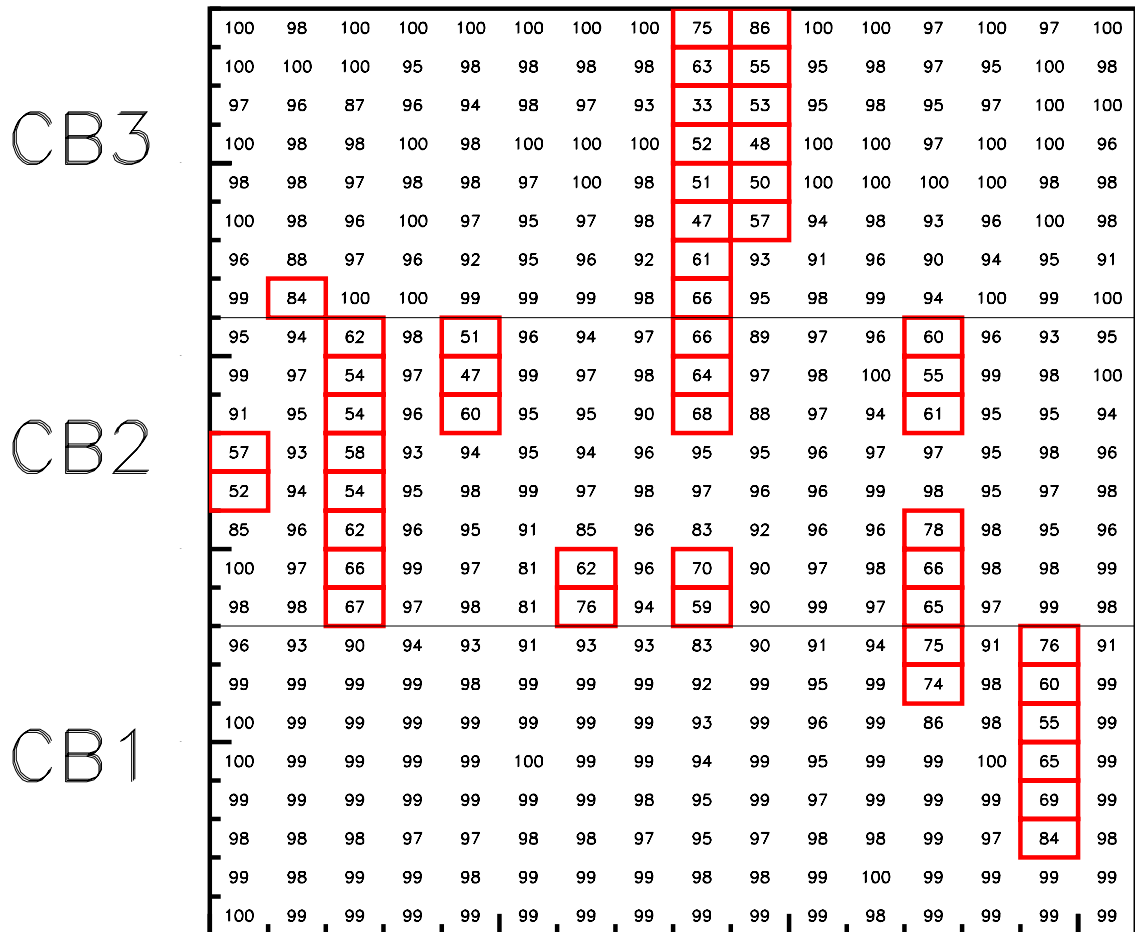

 ϕ

Figure 6.2: Trigger efficiency for the example of year 2000 for energies greater than 5 GeV as a function of impact position z (in wheels CB1, CB2, CB3) and azimuth ϕ . The boxes indicate the cut regions.

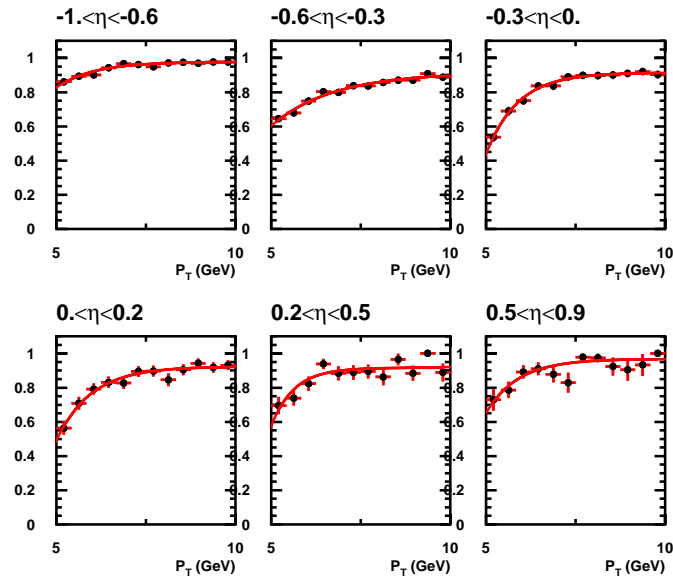


Figure 6.3: Trigger Efficiency (years 1998-2000) as a function of the cluster energy for different η bins. $E_T^\gamma > 5$ GeV used in the analysis.

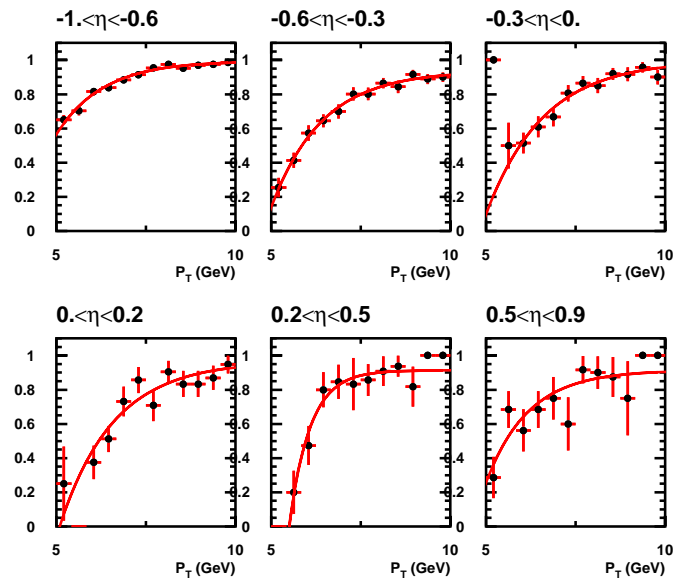


Figure 6.4: Trigger Efficiency (years 1996-1997) as a function of the cluster energy for different η bins. $E_T^\gamma > 7$ GeV used in the analysis.

6.4 Background rejection

In this section the cuts rejecting the various backgrounds are presented. In all the following distributions the previous cuts are already applied. In section 6.5 the efficiency of the cuts for the signal Monte Carlo samples will be summarized and the number of remaining events after each cut for the data and the various background Monte-Carlo samples are listed.

Non- ep -induced background

There are three types of backgrounds not due to ep collisions:

- Muons from cosmic-rays (see figure 6.6). When energetic enough, these muons can produce an electromagnetic shower in the liquid Argon calorimeter.
- So-called halo-muons (see figure 6.6) produced by protons which leave their orbit and interact with the beam-pipe. These muons travel parallel to the proton beam, enter the H1 detector and may trigger an event.
- Beam-gas events (see figure 6.7) where a proton interacts with a particle of the residual gas inside the beam pipe.

The Non- ep -induced events may have a vertex but most of the time its position is far away from the nominal interaction point. To remove a large part of these events the vertex of the events is required to be within 35 cm of the nominal vertex position (see figure 6.5).

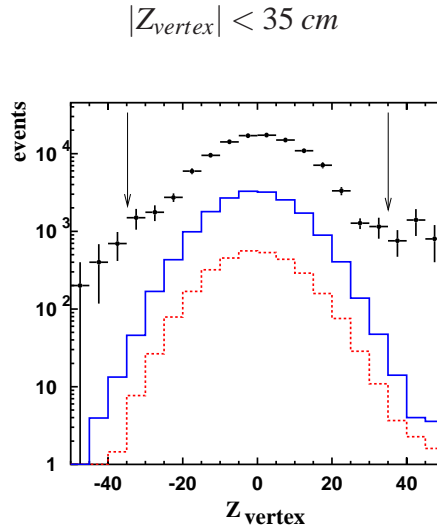


Figure 6.5: Vertex position Z_{vertex} distribution of the candidates of the full data sample selected by QESCAT (section 5.1). A cut $|Z_{\text{vertex}}| < 35 \text{ cm}$ is applied. The points are the data, the dashed line is the prompt photon signal (PYTHIA), the full line is signal+hadronic jet background (PYTHIA). The DIS background is not yet removed. All curves correspond to the integrated luminosity of 105 pb^{-1} .

In addition a set of topological muon finders is used. A muon is characterized by energy depositions along a tube crossing the H1 detector. The topological finders are thus based on the energy deposition patterns in different sub-detectors (tail catcher, liquid Argon calorimeter, SPACAL, central jet chambers).

Compton events

Compton events ($ep \rightarrow e\gamma p$) are characterized by a detected photon and a detected electron in the H1 detector (see figure 6.7). At least two tracks fitted to the vertex crossing the central tracker are required to remove this background (see figure 6.8). This requirement ensures in addition a good vertex reconstruction.

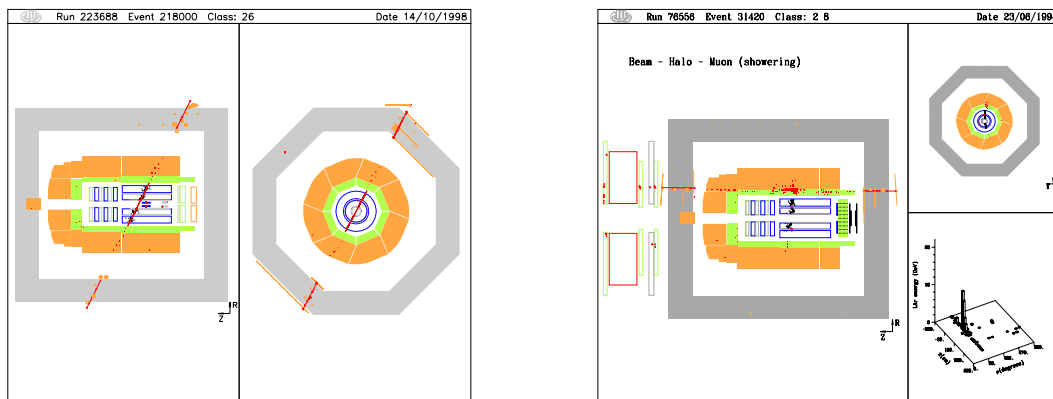


Figure 6.6: A cosmic-ray event (left) and a halo-muon event (right).

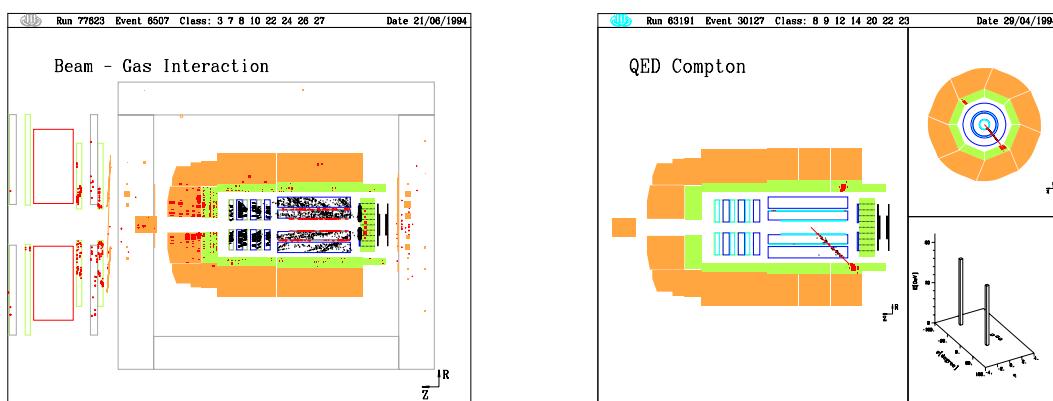


Figure 6.7: A beam-gas event (left) and a compton event (right).

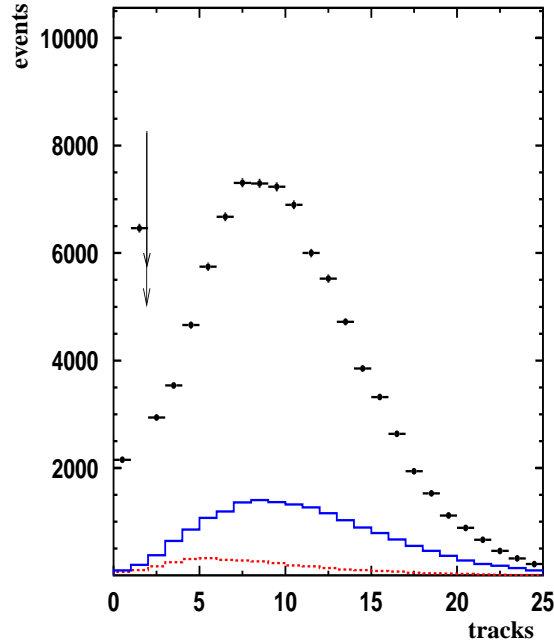


Figure 6.8: Number of tracks fitted to the vertex after the cut $|Z_{vertex}| < 35$ cm. The points are the data, the dashed line is the prompt photon signal (PYTHIA), the full line is signal+hadronic jet background (PYTHIA). The DIS background is not yet removed. All curves correspond to the integrated luminosity of 105 pb^{-1} .

Neutral current events in deep inelastic scattering rejection

Electrons from neutral current deep inelastic scattering (NC-DIS) at high Q^2 produce an electromagnetic shower in the liquid Argon calorimeter. These electrons produce also a track in the central jet chamber.

To remove these electrons we require that no track is pointing to the cluster candidate by a cut on the track-cluster distance. This cut is applied using the tracks fitted to the vertex (DTRA) and the tracks not fitted to the vertex (DTNV). Some tracks are not fitted to the vertex when their reconstruction is not very precise or when the particle producing the track has suffered an interaction or radiation after leaving the vertex position. The tracks are extrapolated to the inner liquid Argon calorimeter surface in order to find their impact position. The cluster-track distance is required to be greater than 25 cm in the plane transverse to the track. Figure 6.9 shows the distributions of these variables for the selected data, for the prompt photon signal, for the di-jets in photo-production background as given by the PYTHIA generator (see section 3.2) and for the background contribution of the NC-DIS events as given by the RAPGAP generator. The data and the NC-DIS events distributions are peaked at zero as expected from tracks correlated to the cluster. The distribution for the prompt photon signal has a small peak at zero due to photon conversions in the beam pipe ($\gamma \rightarrow e^+e^-$). This results in a signal loss of about 10 %.

Regions where the central jet chambers is not efficient are cut out (see more details in section

8.2). This rejects events where an electron goes through an inefficient region of the chamber faking a photon.

In addition, events are removed with a good electron candidate, besides the γ candidate, in the LAr calorimeter or the Spacal. For such NC-DIS events the fake prompt photon is in general not due to a mis-identified electron but due to a neutral meson produced in a hadronic jet.

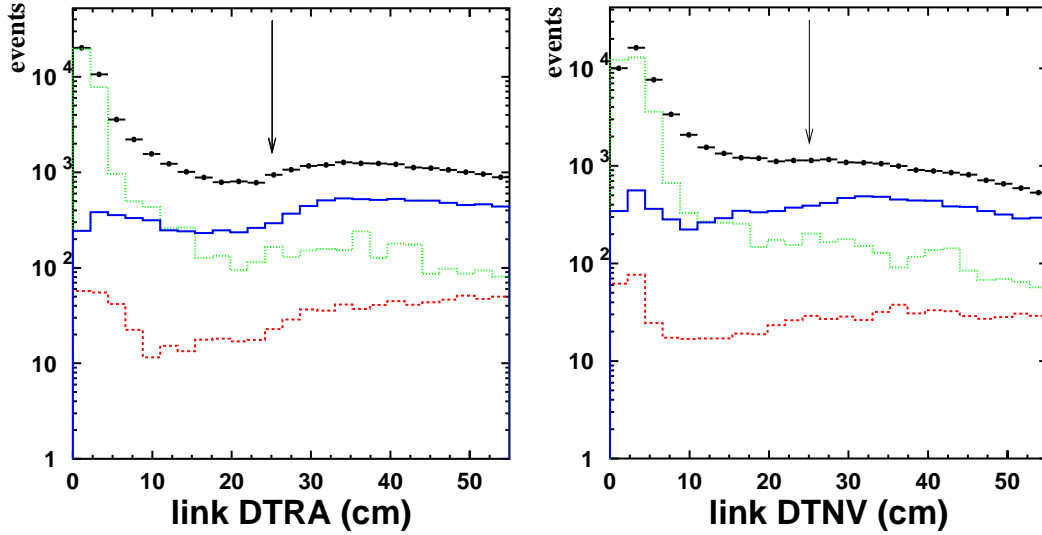


Figure 6.9: Distance of the track impact point on the calorimeter to the cluster candidate for tracks fitted to the vertex (left) and for tracks not fitted to the vertex (right). These distances are required to be > 25 cm. The points are the data, the dashed line is the prompt photon signal (PYTHIA), the full line is signal+hadronic jet background (PYTHIA), the dotted line is the NC-DIS background (RAPGAP). All curves correspond to the integrated luminosity of 105 pb^{-1} .

A further cut is applied on the quantity $y_{JB} = \frac{\Sigma(E-P_Z)}{2E_e}$ which is an estimate of $y = E_\gamma/E_e$ (see chapter 5). If a scattered electron is detected, it is included in $\Sigma(E - P_Z)$ and the value of y_{JB} tends to be close to 1. The value would be exactly one for an event completely contained in the H1 detector, if the energies of all particles are measured exactly. The cut $y_{JB} < 0.7$ removes therefore further NC-DIS events and also some residual compton events. A cut $y_{JB} > 0.2$ removes p -beam gas events which have a low y_{JB} , because most of the energy is deposited in the forward direction. The cut on y_{JB} is:

$$0.2 < y_{JB} < 0.7$$

The y_{JB} selection defines part of the phase space for the finally measured cross-section results. Figure 6.4 shows the y_{JB} distribution and various Monte-Carlo contributions. The photo-production events decrease with increasing y whereas the NC-DIS events peak at $y \approx 1$. After the y_{JB} cut some NC-DIS events remain. An estimate of the number of these events is subtracted from the final results and a small systematic error associated with this estimate is derived (see section 8.2).

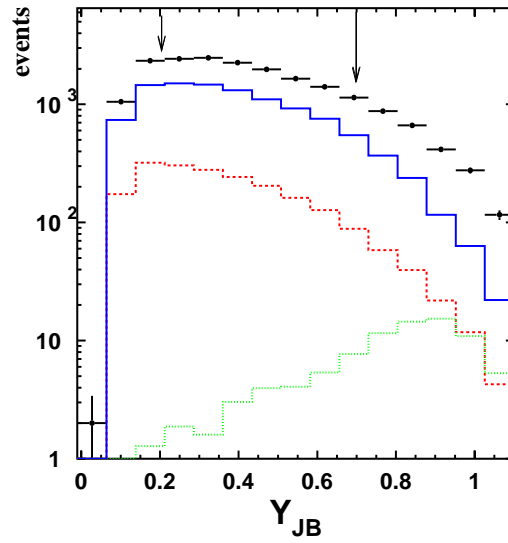


Figure 6.10: y_{JB} distribution after all previous cuts. A cut $0.2 < y_{JB} < 0.7$ is applied. The points are the data, the dashed line is the prompt photon signal (PYTHIA), the full line is signal+hadronic jet background (PYTHIA), the dotted line is the NC DIS background (RAPGAP). All curves correspond to the integrated luminosity of 105 pb^{-1} .

Isolation requirement against neutral mesons

The main remaining background is from neutral mesons (π^0, η) in hadronic jets. They decay in multi-photon states which cannot be resolved by the calorimeter at the considered energies and may fake a single photon shower. They are produced during the hadronisation process of partons and are not likely to be isolated. To reduce this background the cluster candidate is required to be isolated. A cone of radius 1.0 in the (η, ϕ) plane around the candidate cluster is considered. The transverse energy fraction in the cone around the candidate has been defined in section 5.4. The isolation requirement is performed by selecting only events for which this fraction is less than 0.1 (Fig. 6.11):

$$\frac{E_{T \text{ cone}}^{R^{\eta, \phi}=1}}{E_T^\gamma} < 0.1 \quad (6.2)$$

Figure 6.11 shows the distribution of the isolation variable for the selected data, for the prompt photon events and for the dijet-background simulated with PYTHIA before application of the isolation cut and after application of the previous cuts. The prompt photon signal is peaked at zero as expected for well isolated events. The data and the dijet background have a tail to large values of the isolation variable. The cut at 0.1 does not affect strongly the prompt photon signal. The isolation selection defines part of the phase space for the final cross-section results.

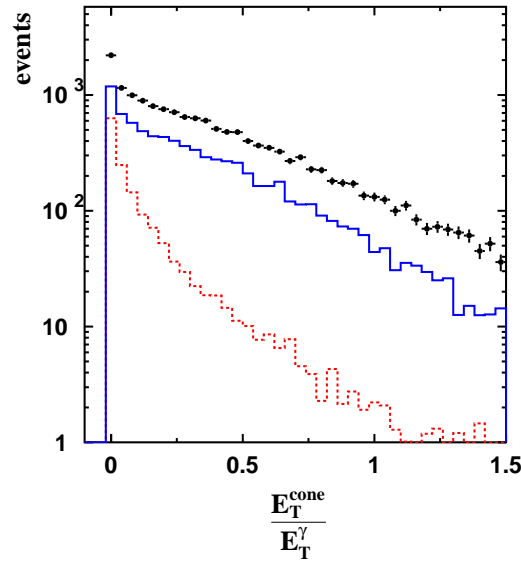


Figure 6.11: *Transverse energy fraction in the cone around the cluster candidate. This energy fraction is required to be less than 0.1. The points are the data, the dashed line is the prompt photon signal (PYTHIA), the full line is signal+hadronic jet background (PYTHIA). All curves correspond to the integrated luminosity of 105 pb^{-1} .*

6.5 Event selection summary

The described cuts are the following:

- Electromagnetic shower finder QESCAT in the LAr Calorimeter.
- DIS Rejection:
 - Cluster-track distance $> 25 \text{ cm}$ (DTNV and DTRA)
 - No other electron candidate.
 - $y_{JB} < 0.7$
- Finders against comics, halo muons
- At least 2 central tracks (against $ep \rightarrow ep\gamma$)
- Isolation in cone $R(\eta, \phi)=1.0$ (against hadronic jets):

$$\frac{E_T^{\text{cone}}}{E_T^\gamma} < 0.1 \quad (6.3)$$

- γ candidate:

$$E_T^\gamma > 5 \text{ GeV} \quad (6.4)$$

$$-1 < \eta^\gamma < 0.9 \quad (6.5)$$

$$0.2 < y < 0.7 \quad (6.6)$$

The efficiency of the cuts is shown in figure 6.12 as a function of the transverse energy E_T^γ and the pseudo-rapidity η^γ . The efficiency is defined as the fraction of the generated events

using the PYTHIA Monte-Carlo samples passing the cuts (defined at the detector level). The overall selection efficiency of the prompt photon signal in the selected fiducial kinematic range is 72%. Table 6.2 gives the number of events after the various cuts.

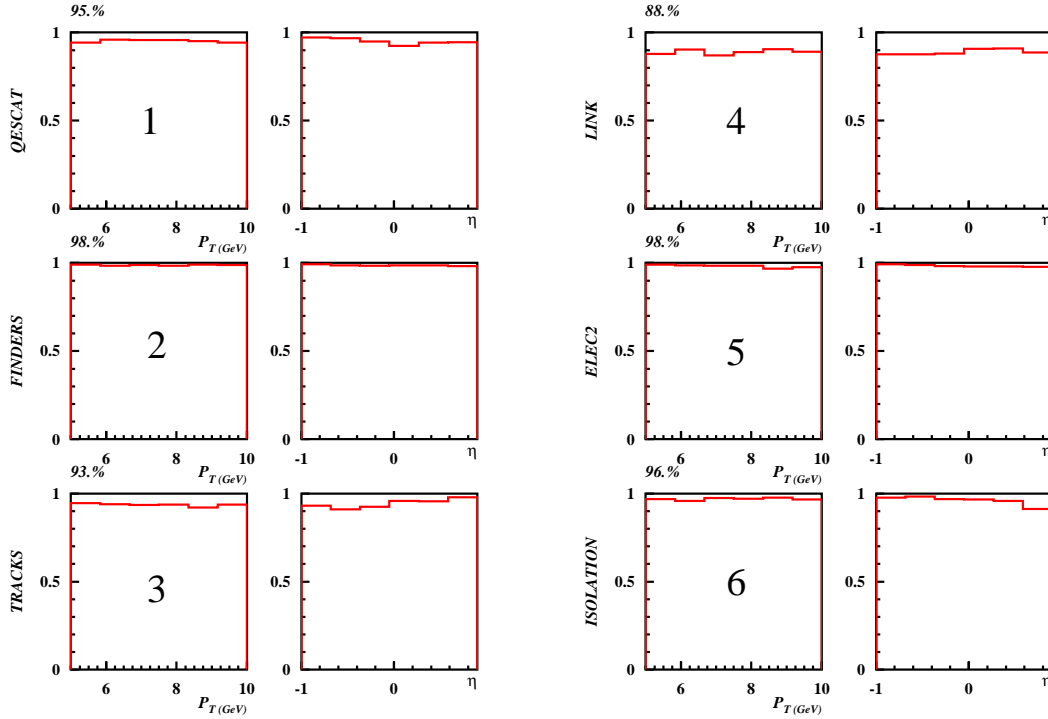


Figure 6.12: Efficiency of the cuts as a function of the transverse energy E_T^γ and the pseudo-rapidity η^γ . The overall efficiency of the various cuts are also indicated on top of the plots. The cuts labels are: *QESCAT*: QESCAT finder, *FINDERS*: cosmics and halo muon finders, *TRACKS*: at least two central tracks, *LINK*: cluster-track link veto, *ELEC2*: no second electron, *ISOLATION*: isolation requirement.

Cuts	Data events	Prompt photons	jets	NC-DIS
QESCAT	132735	2906	15201	44594
FINDERS	94684	2851	15067	44324
TRACKS	86069	2710	14856	38648
LINK	29120	2322	10424	143
ELEC2	22608	1990	8962	102
Y_{JB}	15359	1350	6420	29
ISOLATION	4343	941	1425	26
Shower shape	3383	874	939	24

Table 6.2: Number of events after the different cuts for the data, the prompt photon signal (PYTHIA), the hadronic jet background (PYTHIA) and the NC DIS background (RAP-GAP). The cuts labels are: QESCAT: QESCAT finder, FINDERS: cosmics and halo muon finders, TRACKS: at least two central tracks, LINK: cluster-track link veto, ELEC2: no second electron, Y_{JB} : Y_{JB} cut, ISOLATION: isolation requirement, Shower shape: cut described in chapter 7.

Chapter 7

Extraction of the signal

After the event selection (chapters 5,6) the sample of prompt photon candidates still contains background from neutral mesons (π^0, η). These mesons decay into photons which cannot be resolved by the calorimeter. They fake a single photon shower. Figure 7.1 shows for example an event with an isolated π^0 meson from the dijet background Monte Carlo sample which fulfills the selection criteria equally well as the prompt photon event shown in figure 6.1. The signal is extracted by a likelihood technique using shower shape variables as discriminators. For this purpose Monte Carlo samples were produced of single γ 's, π^0 's and η 's. The results are compared to the PYTHIA prediction.

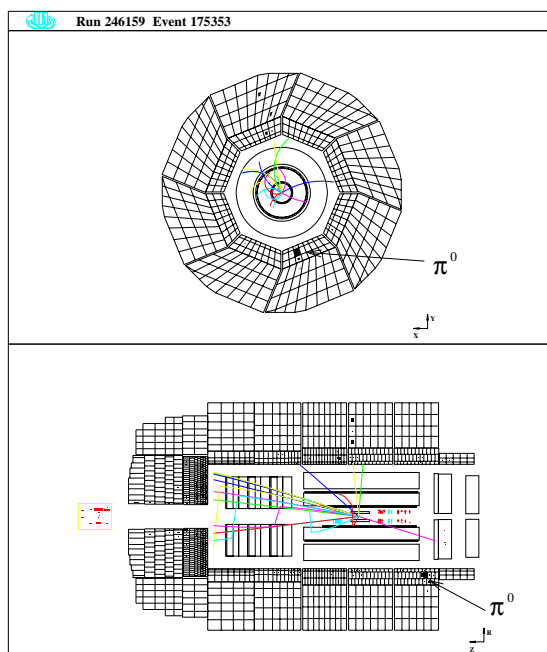


Figure 7.1: *Event with an isolated π^0 selected in the hadronic jet background Monte-Carlo sample. The topology of the event is identical to that of a prompt photon. The isolated cluster candidate (π^0) is compact and the event kinematics fulfill all the selection cuts.*

7.1 π^0 and η background

The decay modes of π^0 's and η and the branching ratios were given in section 3.2. If a π^0 of energy E_{π^0} decays in two photons of energy E_1 and $E_{\pi^0} - E_1$ the opening angle α of the two photons is given by:

$$\alpha = 2 \cdot \arcsin \left[\frac{m_{\pi^0}}{2 \cdot \sqrt{E_1(E_{\pi^0} - E_1)}} \right] \quad (7.1)$$

where $m_{\pi^0}=135$ MeV is the mass of the π^0 . For large π^0 energies ($E_{\pi^0} \gg m_{\pi^0}$) a strong boost takes place. The typical angle α of the two photons is given by the case where the two photons of the π^0 -decay emerge perpendicular to the π^0 -momentum. The angle α is then minimal and the photons have the same energy:

$$\alpha_{min} = 2 \cdot \arcsin \left(\frac{m_{\pi^0}}{E_{\pi^0}} \right) \quad (7.2)$$

The corresponding distance of the two photons $D_{\gamma\gamma}$ at the surface of the calorimeter is given for small α by:

$$D_{\gamma\gamma} \approx \frac{R_{cal}}{\sin(\theta_{\pi^0})} \alpha_{min} \approx \frac{2 \cdot R_{cal} \cdot m_{\pi^0}}{E_T^{\pi^0}} \quad (7.3)$$

where $R_{cal}=105$ cm is the inner radius of the LAr calorimeter.

The distance of the two photons $D_{\gamma\gamma}$ decreases with $E_T^{\pi^0}$. For π^0 's in the E_T range 5-10 GeV, $D_{\gamma\gamma}$ is in the range 2.8-5.7 cm and for η 's ($m_{\eta}=547$ MeV), in the same E_T range, $D_{\gamma\gamma}$ is in the range 11-23 cm. The typical size of the cells is 5×5 cm² in CB3 and 10×7 cm² in CB1 and CB2. The decay products of π^0 and η form at these energies a single shower in the LAr calorimeter. Background from η is however already strongly reduced by the QESCAT selection (section 5.1.1).

7.2 The shower shape variables

The shower shapes are different for photons and mesons. Figure 7.2 shows a sketch of the showers produced by a photon and by a π^0 .

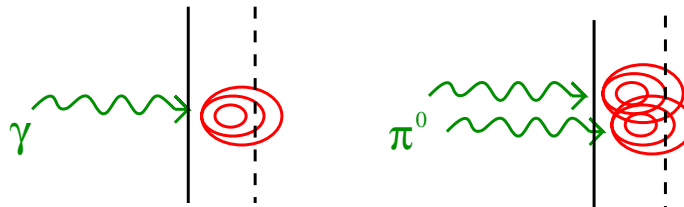


Figure 7.2: Sketch of the expected showers for γ 's and π^0 's.

The photon showers are expected to be more narrow and compact. For two or more photons the shower is likely to start closer to the calorimeter surface, because the probability of photon

conversion is higher than for one photon. Three shower shape variables are used to discriminate the background from the signal.

The shower radius $\langle R \rangle$

The shower radius is defined as the energy density weighted mean width:

$$\langle R \rangle = \frac{\sum_{cells} w_i r_i}{\sum_{cells} w_i}. \quad (7.4)$$

where w_i are the energy densities of the cells i of the selected cluster and r_i are the distances to the cluster axis. Narrow showers have small values of $\langle R \rangle$.

The hot core fraction HCF

The energy fraction in the core of the selected cluster HCF was defined in section 5.1.1:

$$HCF = \frac{\text{Energy in shower core}}{\text{Total Energy}}. \quad (7.5)$$

Compact showers have large values of HCF .

The first layer fraction FLF

Figures 4.6 and 4.5 show the cell structure of the calorimeter. During its development the shower crosses different layers of cells. FLF is the energy fraction of the selected cluster in the first (or inner) layer of the calorimeter:

$$FLF = \frac{\text{Energy in first layer}}{\text{Total Energy}}. \quad (7.6)$$

The energy of the cluster in the first layer depends on the starting point of the shower. It is expected that FLF is smaller for photons than for the π^0 background.

Samples of γ 's, π^0 's and η 's were simulated in the LAr calorimeter. The cuts of the electromagnetic shower finder QESCAT (see section 5.1) were applied to the simulated particles. Figures 7.3, 7.4 and 7.5 show the distributions of the shower shape variables for γ 's and π^0 's for different E_T and η bins. The distribution for all the Monte Carlo simulations have been tuned by comparing samples of selected electrons from the data and of simulated electrons (see section 8.2). The shapes of the distributions vary for different η bins as the granularity of the calorimeter changes from wheel CB3 ($-0.26 < \eta < 0.9$) to the wheels CB1-CB2 ($-1. < \eta < -0.26$). As the energy becomes larger the discrimination becomes worse for the $\langle R \rangle$ and HCF shower shape variables. This is expected because the decay products become more collimated and the showers become more compact. The FLF discrimination is rather energy independent because it just depends on the conversion probability of the photons. We restrict the analysis to E_T below 10 GeV where the discrimination is better and the statistics not too low.

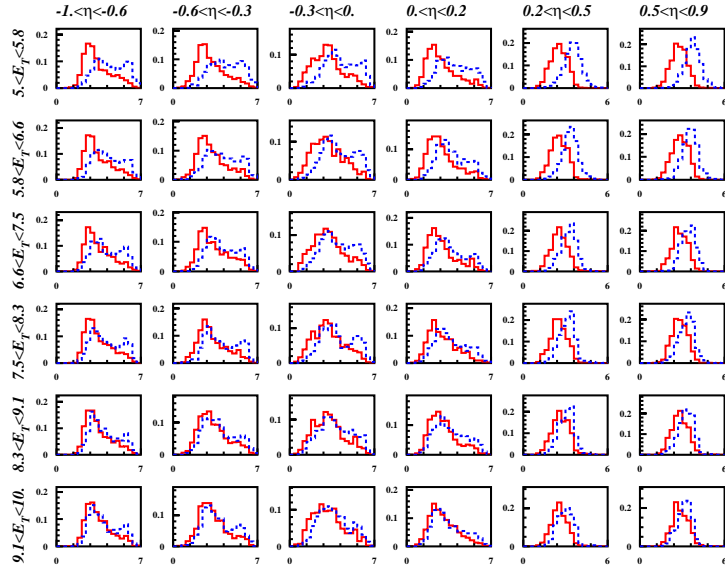


Figure 7.3: Clusters radius ($\langle R \rangle$ in cm) for all the used bins in η and E_T (GeV). Simulation of single γ 's (solid line) and π^0 (dashed line). The distributions are normalized to one.

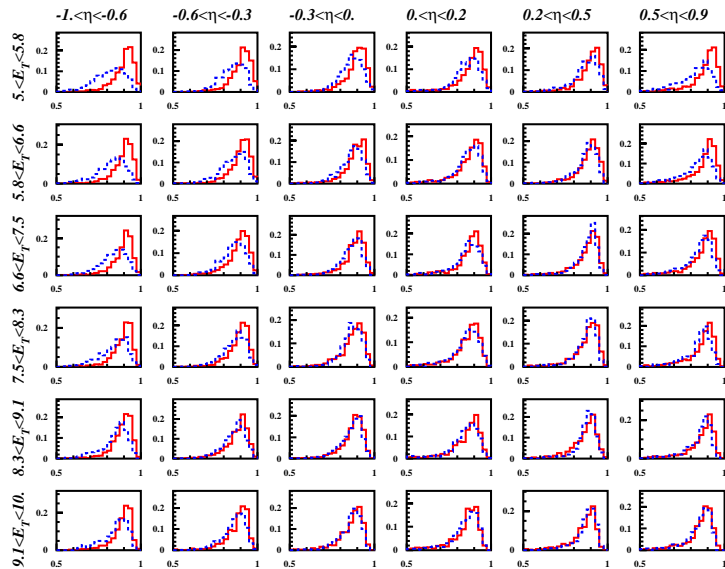


Figure 7.4: Clusters hot core fraction (HCF) for all the used bins in η and E_T (GeV). Simulation of single γ 's (solid line) and π^0 (dashed line). The distributions are normalized to one.

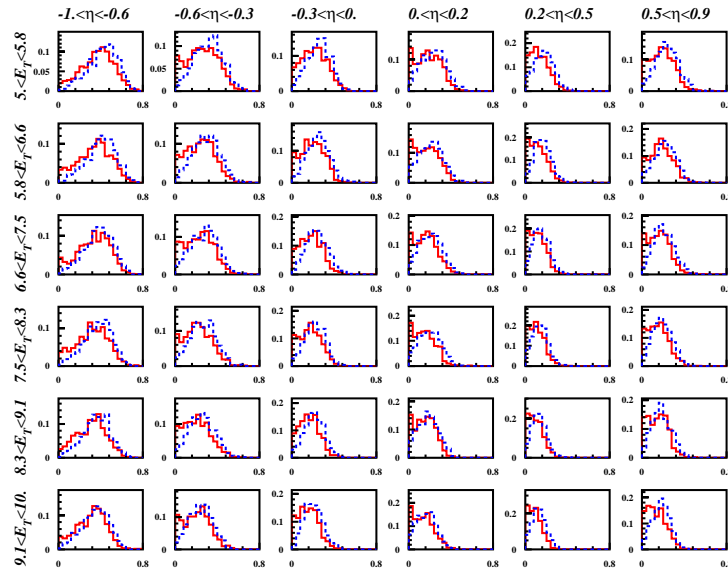


Figure 7.5: Clusters first layer fraction (FLF) for all the used bins in η and E_T (GeV). Simulation of single γ 's (solid line) and π^0 (dashed line). The distributions are normalized to one.

7.3 Signal extraction

7.3.1 Discriminator definition

The three discriminating variables $x_1 = \langle R \rangle$, $x_2 = HCF$ and $x_3 = FLF$ of a candidate shower are combined into a single discriminator using the definition [93]:

$$D = \frac{\prod_i P_\gamma(x_i)}{\prod_i P_\gamma(x_i) + \prod_i P_{\pi^0}(x_i)}, \quad i = 1, 2, 3 \quad (7.7)$$

The probability densities $P_\gamma(x_i)$ for photons and $P_{\pi^0}(x_i)$ for π^0 mesons are shown in figures 7.3, 7.4 and 7.5. The discriminator D is in the range $[0,1]$ and is greater for photons than for the background. Figure 7.6 shows the discriminator distribution for the selected data, for the prompt photon events and for the hadronic background simulated with PYTHIA after the selection of chapters 5 and 6. A further cut is applied on the discriminator which removes the region which is dominated by background:

$$D > 0.125 \quad (7.8)$$

This cut removes 27% of the π_0 background and 75% of the η background. After this cut 94% of the background are π_0 's and 5% are η 's, as estimated by the PYTHIA background simulation. The other sources of background are negligible (below 2% in total, e.g. 0.4 % antineutrons).

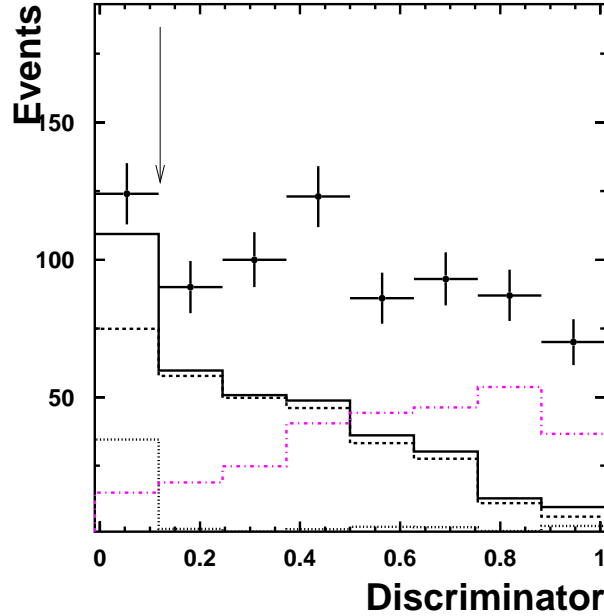


Figure 7.6: *Discriminator distribution after all previous cuts for $5 < E_T < 10$ GeV and $-1 < \eta < 0.9$. A cut $D > 0.125$ is applied in addition. The points are the data, the dashed-dotted line is the prompt photon signal (PYTHIA), the full line is hadronic background (PYTHIA), the dashed line is the π^0 contribution and the dotted line is the η^0 contribution. All curves correspond to the integrated luminosity of 105 pb^{-1} .*

Figure 7.7 shows as a consistency check how different cuts on the discriminator D ($D > 0$, $D > 0.5$, $D > 0.75$) affect the isolation distribution of the selected events, the simulated prompt photon signal and the simulated hadronic background. For higher discriminator values the candidate cluster is more isolated. This corresponds to the expectation that the prompt photons are more isolated than the background showers.

7.3.2 Fit of the different particle contributions to the data

As it is impossible to distinguish γ 's and π^0 's on a event by event basis, the number of signal events in the data is extracted by a fit of the measured discriminator distributions, defined in section 7.3.1, by signal and background components.

The different discriminator distributions for the data, for photons, π^0 's and η 's are labeled respectively D^{data} , D^γ , D^{π^0} and D^η . A fit $\alpha D^\gamma + \beta D^{\pi^0} + \delta D^\eta = D^{data}$, where α , β and δ are the parameters giving the fractions of the different particle contributions, is performed for each bin of the (E_T, η) -grid shown in figures 7.3, 7.4 and 7.5. The sum of all contributions is constrained to be the total number of data events: $\alpha + \beta + \delta = 1$. In the fit, the η fraction

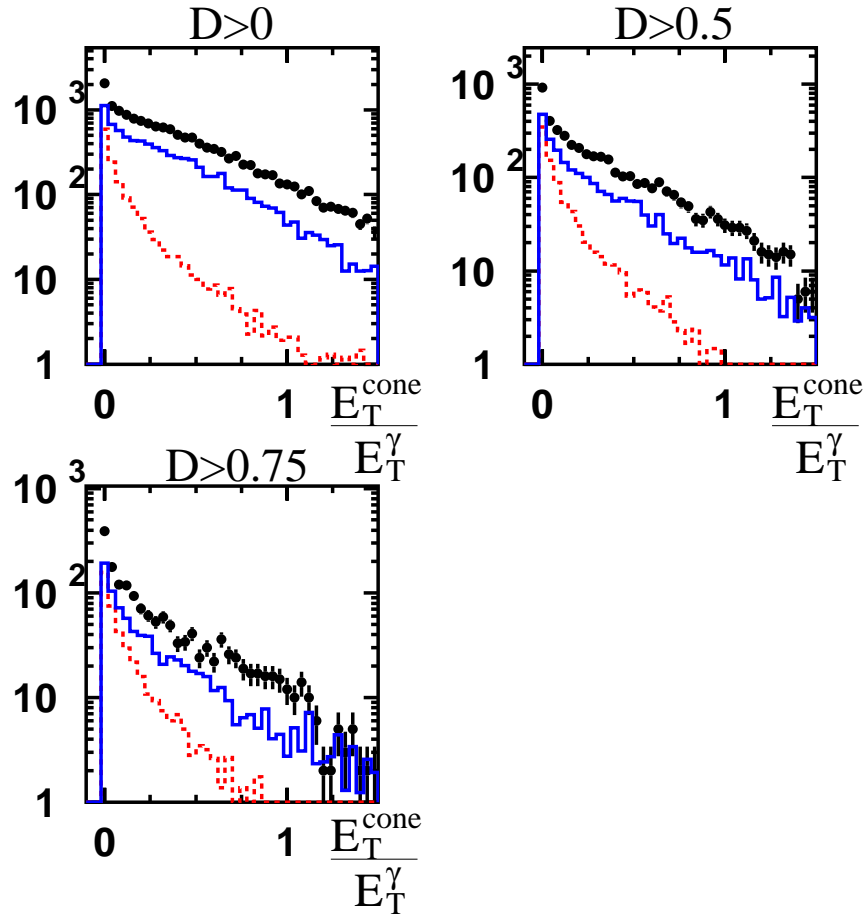


Figure 7.7: Effect of the variation of the discriminator cut on the the isolation distribution. The isolation cut $E_T^{\text{cone}}/E_T^\gamma < 0.1$ is here not applied. The mean $E_T^{\text{cone}}/E_T^\gamma$ of the data distributions is $\langle E_T^{\text{cone}}/E_T^\gamma \rangle = 0.35$ for $D > 0$, $\langle E_T^{\text{cone}}/E_T^\gamma \rangle = 0.29$ for $D > 0.5$ and $\langle E_T^{\text{cone}}/E_T^\gamma \rangle = 0.26$ for $D > 0.75$. The points are the data, the full line is signal+background (PYTHIA) and the dashed line is the the prompt photon signal (PYTHIA).

$\delta/(\beta + \delta)$ in the background is taken from the PYTHIA Monte-Carlo sample for each bin of the (E_T, η) grid individually. A so-called binned maximum likelihood fit [94] is used. It takes into account the possibly low statistics in some bins of the data discriminator distributions. The resulting fitted parameters are obtained when the function $\ln(L)$ is maximal ($\ln(L)_{\text{max}}$) with:

$$\ln(L) = \sum_k [D_k^{\text{data}} \cdot \ln(\alpha D_k^\gamma + \beta D_k^{\pi^0} + \delta D_k^\eta) - (\alpha D_k^\gamma + \beta D_k^{\pi^0} + \delta D_k^\eta)]. \quad (7.9)$$

The summation is over the bins k of the discriminator distributions. The standard deviation error of the parameters is obtained when the function $\ln(L)$ takes the value $\ln(L)_{\text{max}} - \frac{1}{2}$. The statistical errors provided by the fits depend on the number of events in the bins and the discrimination power of the shower shape variables. Figure 7.8 shows the results of the fits for all bins of the grid.

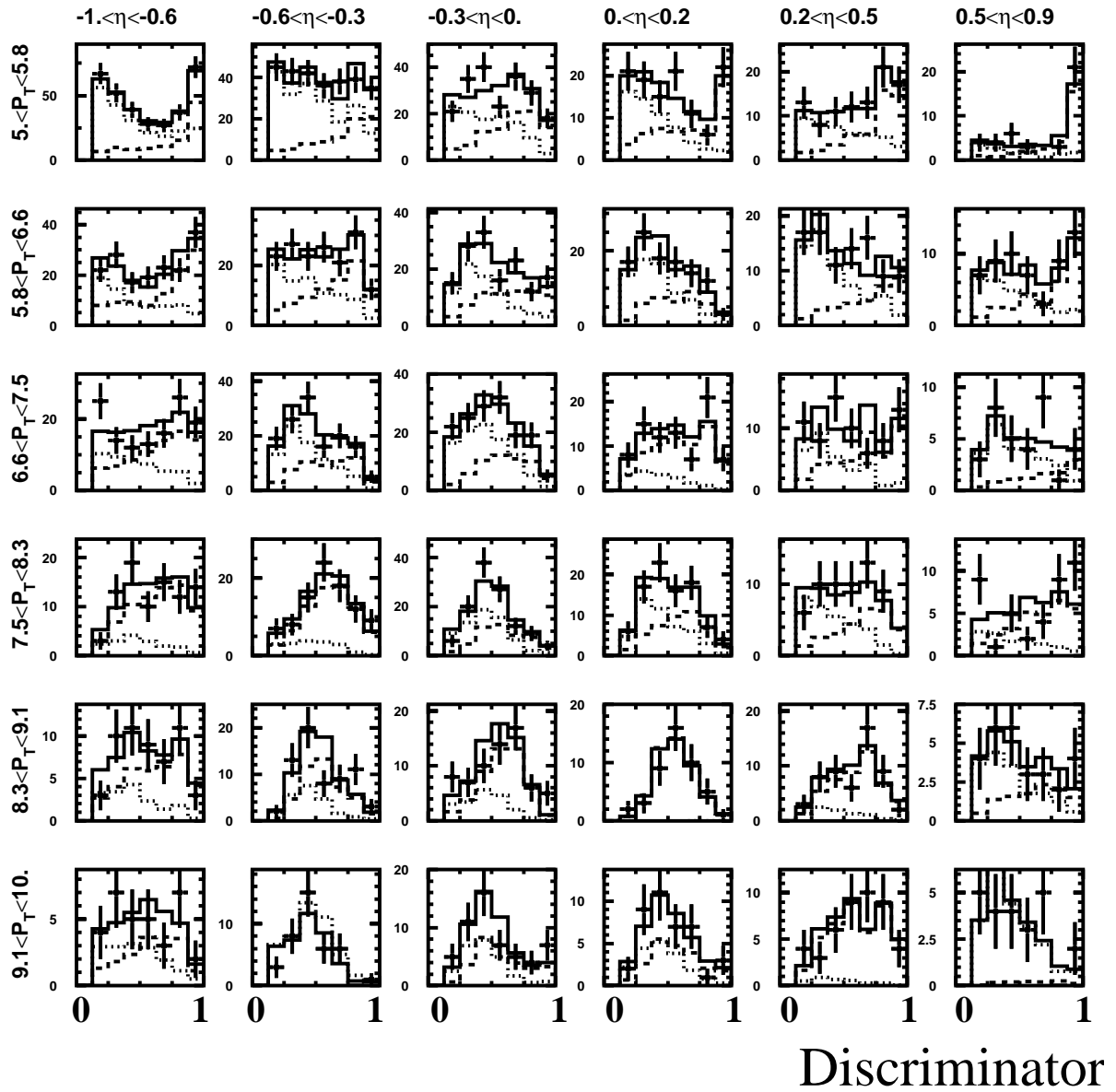


Figure 7.8: Discriminator distributions in all bins in η and E_T (GeV) are shown for the data together with the result of the fits (full dark line). The fitted contributions of γ 's (dashed dark line) and of the background (dotted light line) are also shown.

Figure 7.9 shows the measured distributions of $\langle R \rangle$, HCF and FLF and the simulated distributions of photons and background from π^0 and η mesons with the normalisations taken from the likelihood fits in the different bins. The measured distributions are well described by the distributions obtained from the fit.

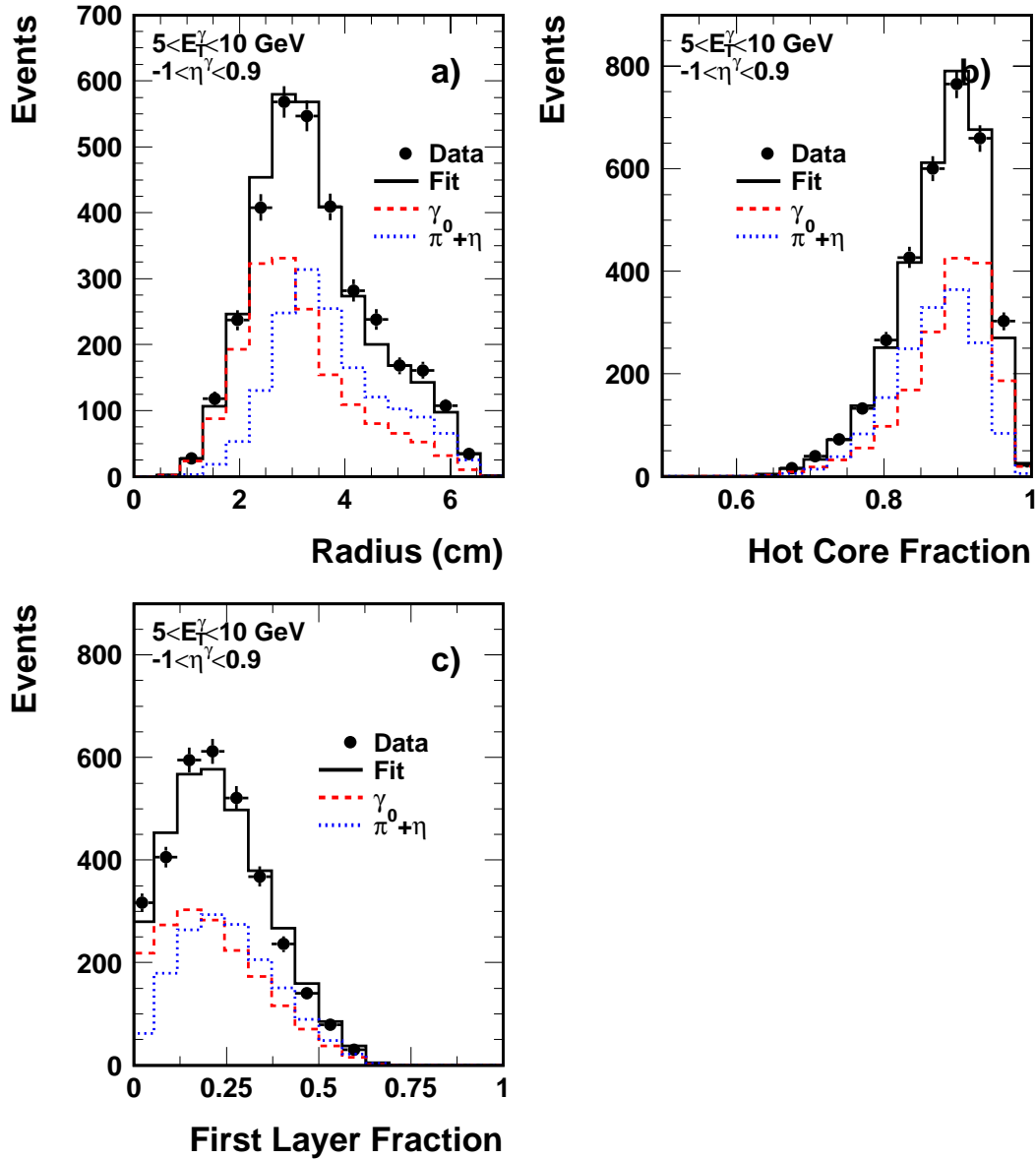


Figure 7.9: Distributions of the mean transverse shower radius $\langle R \rangle$ (a), and the hot core fraction HCF (b) and the first layer fraction FLF (c) for the selected photon candidates (solid line) summing over the full range for $-1 < \eta < 0.9$, $5 < E_T^\gamma < 10$ GeV. The simulated distributions for photons (dashed lines) and background ($\pi^0 + \eta$, dotted lines) are normalized by the likelihood fits.

7.4 Comparison to PYTHIA

7.4.1 E_T and η distributions with and without jet requirement

The E_T and η distributions of the selected events are compared with the PYTHIA prediction in figure 7.10. Here, in addition to the cuts of chapters 5 and 6, the discriminator cut $D > 0.125$ (see section 7.3.1) has been applied. PYTHIA is about 50

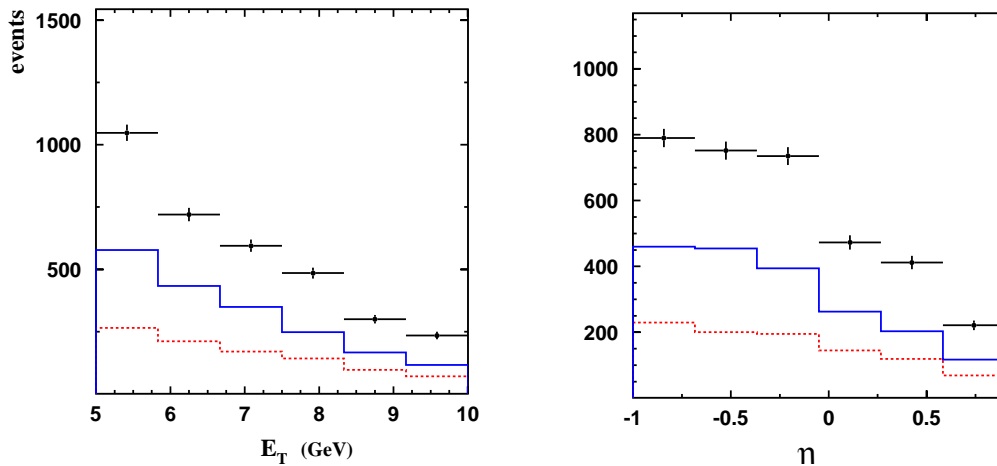


Figure 7.10: E_T and η distribution for the selected events. The points are the data, the full line is signal+background (PYTHIA) and the dashed line is the the prompt photon signal (PYTHIA).

In order to better understand the discrepancy between the data and the PYTHIA prediction further studies are done. In addition to the prompt photon candidate, a jet with $P_T^{jet} > 5$ GeV is required. The variables P_{\perp} , P_{\parallel} and $\Delta\Phi$ describe the acollinearity of the prompt photon candidate with the jet (fig. 7.11). If the jet perfectly balances the prompt photon in P_T , P_{\perp} is equal to zero, P_{\parallel} is equal to E_T^{γ} and $\Delta\Phi$ is equal to 180° .

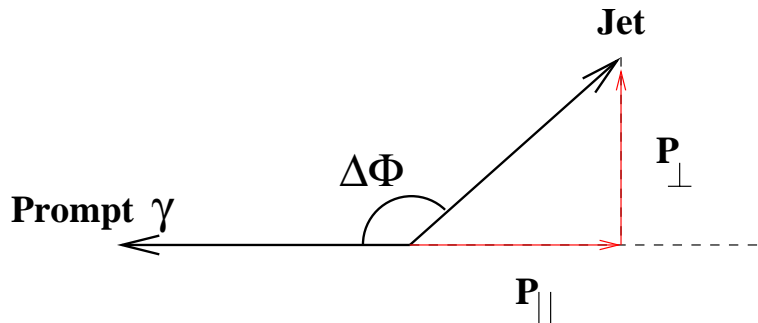


Figure 7.11: Definition of the variables P_{\perp} , P_{\parallel} and $\Delta\Phi$.

Figure 7.12 shows the P_{\perp} distribution with the previously described selection and with the jet requirement. Higher Order QCD effects enter for high values of P_{\perp} , for instance when a quark from the hard process radiates a gluon. PYTHIA fails to describe the data at large P_{\perp} . This indicates that the higher order treatment in PYTHIA by parton showers is not sufficient.

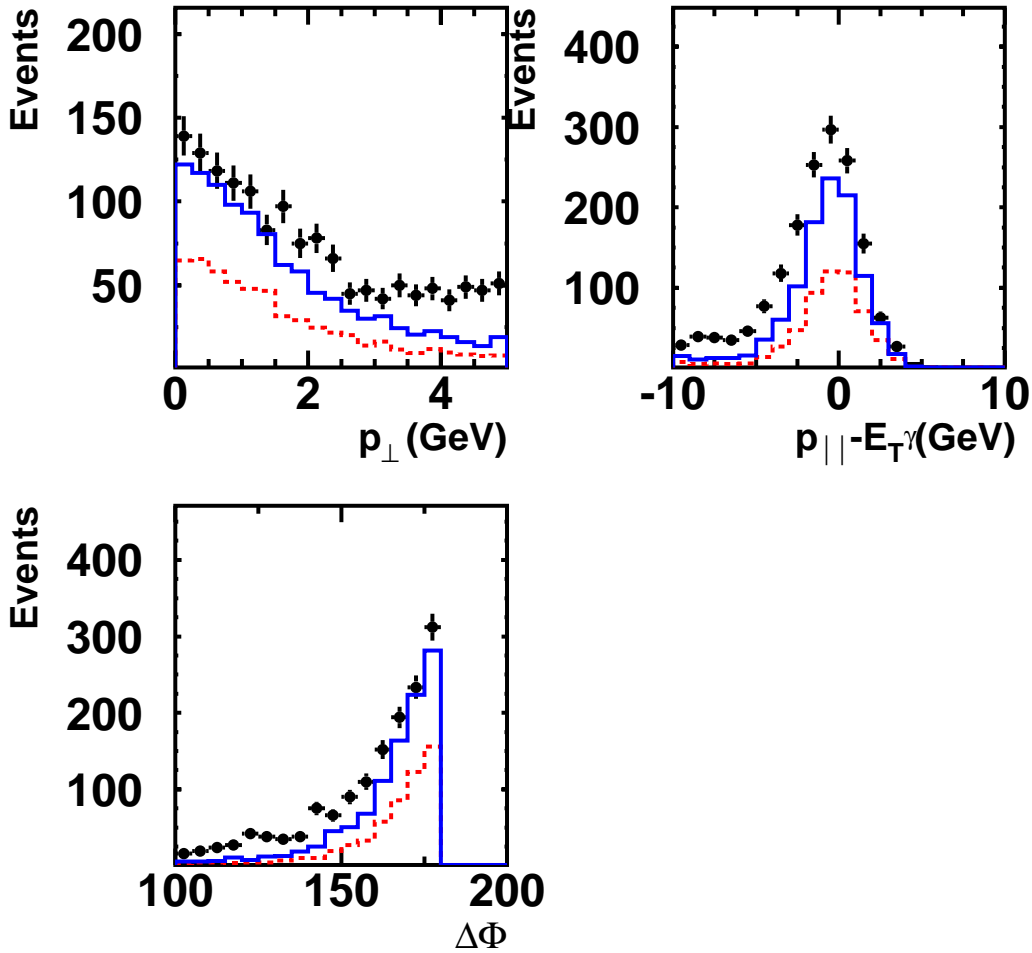


Figure 7.12: P_{\perp} , $P_{\parallel} - E_T^{\gamma}$ and $\Delta\Phi$ distributions. The points are the data, the full line is signal+background (PYTHIA) and the dashed line is the the prompt photon signal (PYTHIA).

The agreement with PYTHIA is much improved if well balancing jets are required. In figure 7.13 the further condition $P_{\perp} < 1$ GeV is applied to the selected events. The distributions of the transverse momentum E_T^{γ} , The pseudo-rapidity η^{γ} of the γ candidate, the transverse momentum P_T^{jet} , the pseudo-rapidity η^{jet} of the jet are very well described by PYTHIA with the exception of the η^{jet} distribution which is shifted in PYTHIA to lower η^{jet} values. In the subsequent prompt photon analysis the cut $P_{\perp} < 1$ GeV is not applied.

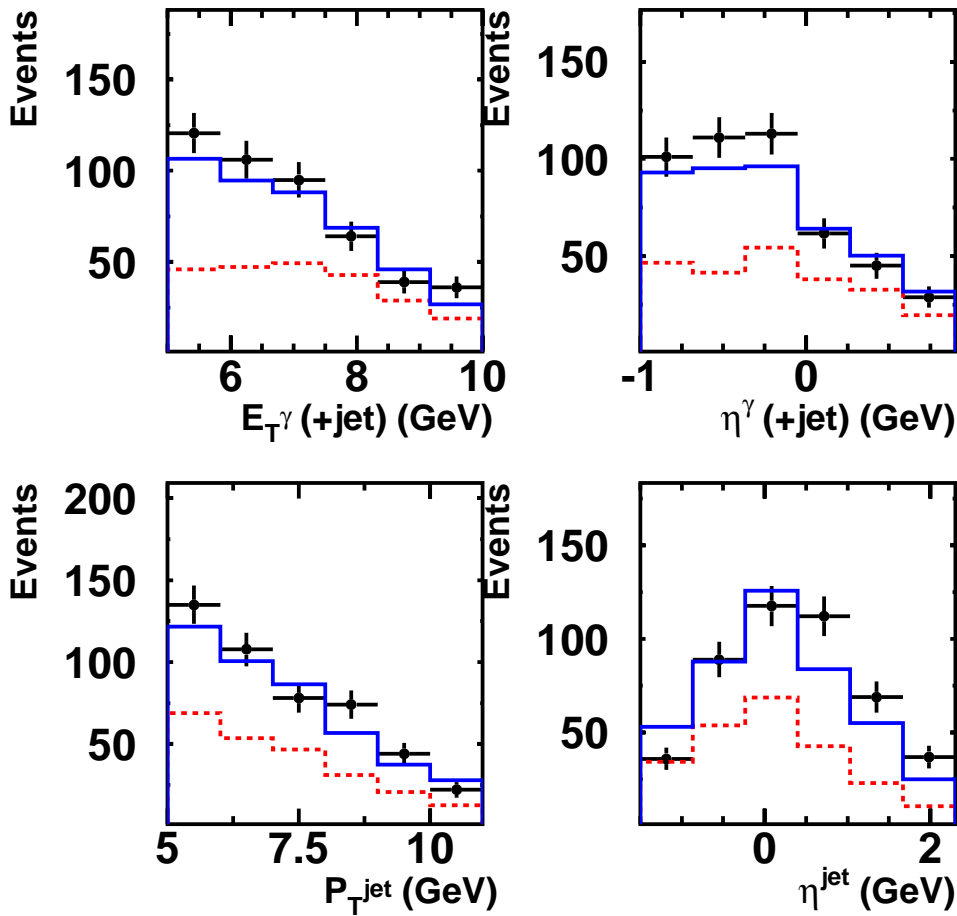


Figure 7.13: Distributions of the transverse momentum E_T^{γ} and the pseudo-rapidity η^{γ} of the γ candidate of the selected events, and the transverse momentum P_T^{jet} and the pseudo-rapidity η^{jet} of the jet with $P_T^{jet} > 5$ GeV and $P_{\perp} < 1$ GeV. The points are the data, the full line is signal+background (PYTHIA) and the dashed line is the the prompt photon signal (PYTHIA). These cuts are not applied for the final inclusive prompt γ results.

Figure 7.14 shows the resulting E_T and η distributions and comparisons to PYTHIA, separately for the extracted signal and for the background. In these distributions the number of events in the E_T (η) bins are obtained by adding the number of signal events from the fit in the corresponding rows (columns) of the grid in E_T and η . The statistical errors are obtained by adding in quadrature the errors of each contributing bin of the grid. PYTHIA is 30%-50% below the data for both the prediction of the signal and of the background.

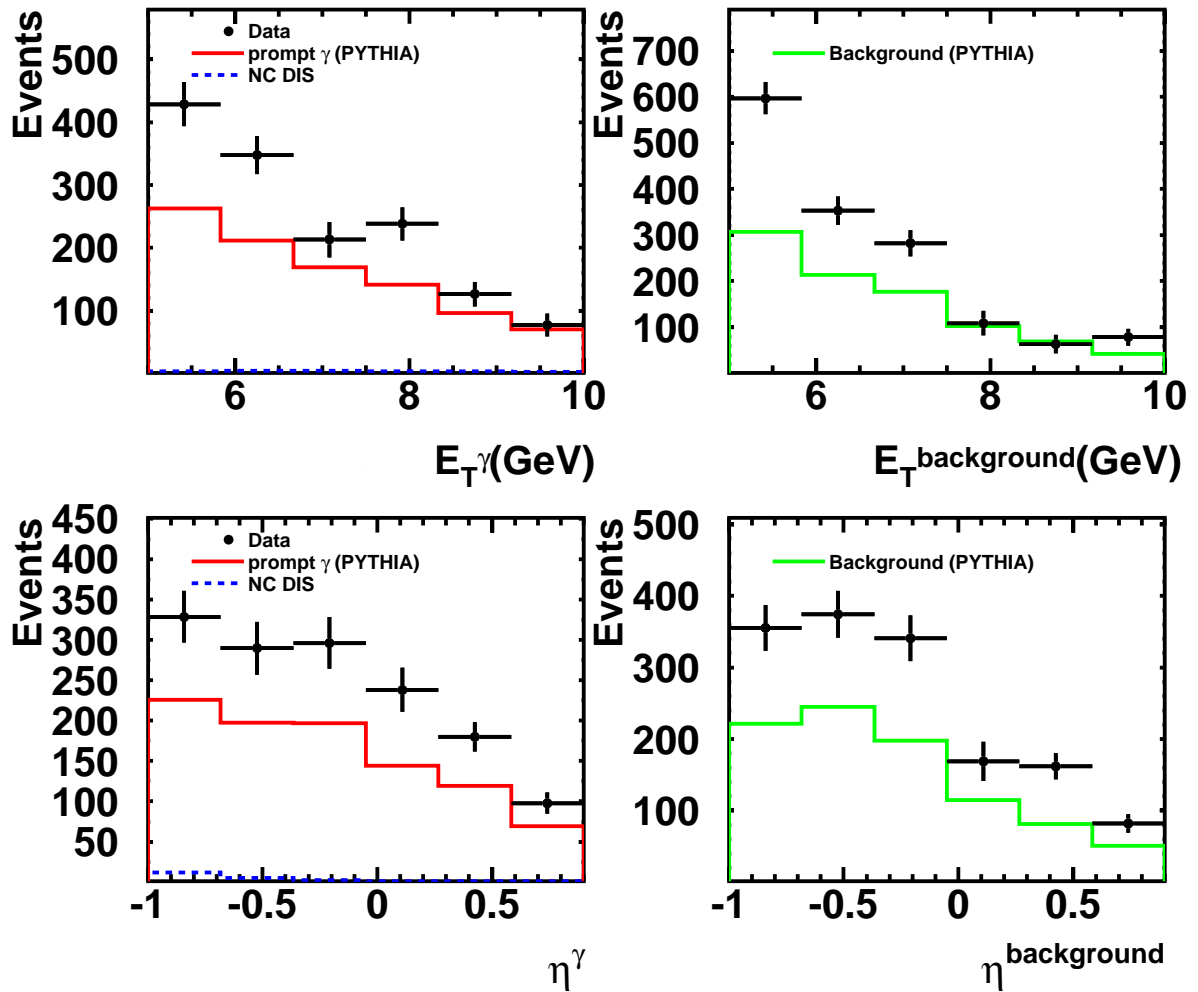


Figure 7.14: E_T and η distributions for extracted prompt photon candidates (left) and background (right) in comparison with PYTHIA. The dotted line is the NC DIS background (RAP-GAP) which is to be subtracted from the data (systematic error discussion in chapter 8).

7.4.2 Variation of the isolation cuts

The isolation requirement discussed in section 6.4 is varied for the data and the PYTHIA samples. This study shows how well the isolation properties of the prompt photon candidates are described by PYTHIA. In addition, as PYTHIA is used for the cross section extraction, the isolation description of PYTHIA has to be good enough and systematic uncertainties will be given in chapter chapter 8. Finally this study is also a good test of the procedure of signal extraction.

The cut in the analysis was:

$$\frac{E_T^{cone(R)}}{E_T^\gamma} < \varepsilon \quad (7.10)$$

with a cone radius $R=1$ and an isolation cut $\varepsilon=0.1$ Table 7.1 shows the different values used here for R and ε .

Variation of the cone radius	Variation of the isolation cut
R=1. reference (horizontal line)	$\varepsilon=0.1$ reference (horizontal line)
R=1.1	$\varepsilon=0.15$
R=0.7	$\varepsilon=0.05$

Table 7.1: *Variation of the isolation cuts used.*

After varying the isolation requirement, the extraction of the signal was performed again. Figure 7.15 shows the relative variations in the number of extracted signal events.

Figure 7.16 shows the same variations for the data before signal extraction and for the signal+hadronic jet background prediction of the PYTHIA Monte-Carlo. The variations are larger than for the signal, as the background is less isolated.

These relative variations for the extracted signal as well as for signal+background are very well reproduced by the PYTHIA simulations.

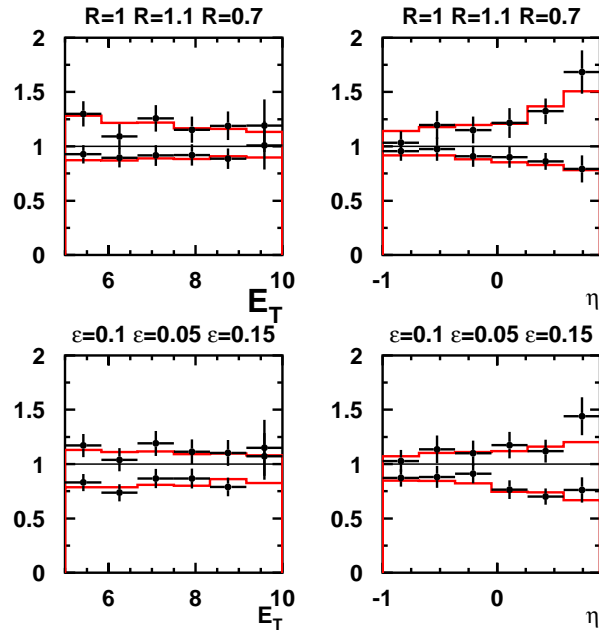


Figure 7.15: *Relative change of the extracted signal for data (points) and of prompt photon PYTHIA Monte Carlo (histograms) by variation of the isolation cut ϵ and radius R as a function of E_T and η .*

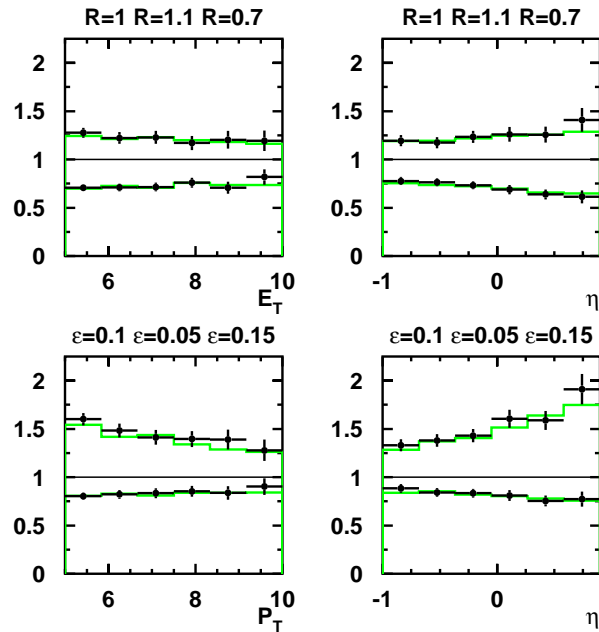


Figure 7.16: *Relative change of data yield before signal extraction (points) and of signal+hadronic jet background PYTHIA Monte Carlo (histograms) by variation of the isolation cut ϵ and radius R as a function of E_T and η .*

Chapter 8

Cross section calculation

This chapter describes how the prompt photon cross sections are derived from the extracted prompt photon signal. The different systematic uncertainties are presented.

8.1 Cross section determination

8.1.1 Correction to generator level

The number of prompt photon events has to be corrected to take into account the losses due to the selection described in chapters 6 and 7. This is done using the prompt photon PYTHIA Monte Carlo sample. In a first step, events are selected at the generator level without applying the cuts at the detector level. The selection cuts at the generator level for the inclusive prompt photon analysis are:

$$\begin{aligned}0.2 < y < 0.7 \\5 < E_T^\gamma < 10 \text{ GeV} \\-1 < \eta^\gamma < 0.9 \\E_T^{cone} / E_T^\gamma < 0.1 \\Q^2 < 1 \text{ GeV}^2\end{aligned}$$

A jet with $E_T^{jet} > 4.5 \text{ GeV}$ and $-1.5 < \eta^{jet} < 2.3$ is required in addition for the prompt photon+jet analysis.

In a second step, the selection which is applied to the data is also applied at the detector level to the Monte Carlo events. The correction factors or acceptances are then given for each bin i by comparing the number of generated events with the above selection to the number of selected events at the detector level:

$$\text{correction factor} = \frac{\text{generated events}}{\text{selected events}} \quad (8.1)$$

The 1996-97 data are corrected to the 920 GeV proton beam energy of the years 1998-2000 using PYTHIA (< 4% effect). Figure 8.1 shows the correction factors (inverse) averaged over

the years as a function of E_T and η . In the analysis the correction factors $C(\eta, E_T)$ are calculated for the (η, E_T) bins of the grid discussed in chapter 7.

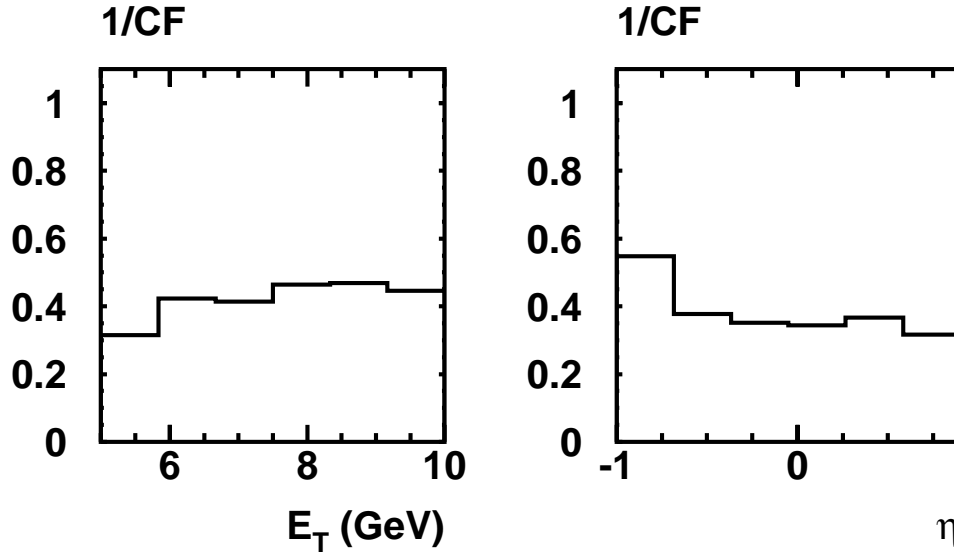


Figure 8.1: $1/(\text{correction factor})$ as a function of E_T and η obtained using PYTHIA prompt photon samples averaged over the full data taking period.

8.1.2 Bin Purities

Using the PYTHIA prompt photon events, the so-called purity of the bin i in η and E_T is determined as the number of generated and reconstructed events in bin i divided by the number of events reconstructed in bin i . For bins of high purity there is little contamination by events migrating from other bins. These migrations are due to the smearing of the variables resulting from the measurement. Figure 8.2 shows the purities of the η and E_T bins. The purity varies between 60 % and 70 % for the E_T bins and is about 90 % for the η bins. The purity is much better for the η bins than for the E_T bins because, relatively to the chosen bins, the resolution of the angle measurement is much better than the energy measurement.

8.1.3 Cross sections

The differential prompt photon cross sections $d\sigma/d\eta^\gamma$ and $d\sigma/dE_T^\gamma$ are then given by:

$$d\sigma/d\eta^\gamma = \frac{\sum_{E_T^\gamma} (N(\eta^\gamma, E_T^\gamma) \cdot C(\eta^\gamma, E_T^\gamma))}{\Gamma(\eta^\gamma) \cdot \int L dt} \quad (8.2)$$

$$d\sigma/dE_T^\gamma = \frac{\sum_{\eta^\gamma} (N(\eta^\gamma, E_T^\gamma) \cdot C(\eta^\gamma, E_T^\gamma))}{\Gamma(E_T^\gamma) \cdot \int L dt} \quad (8.3)$$

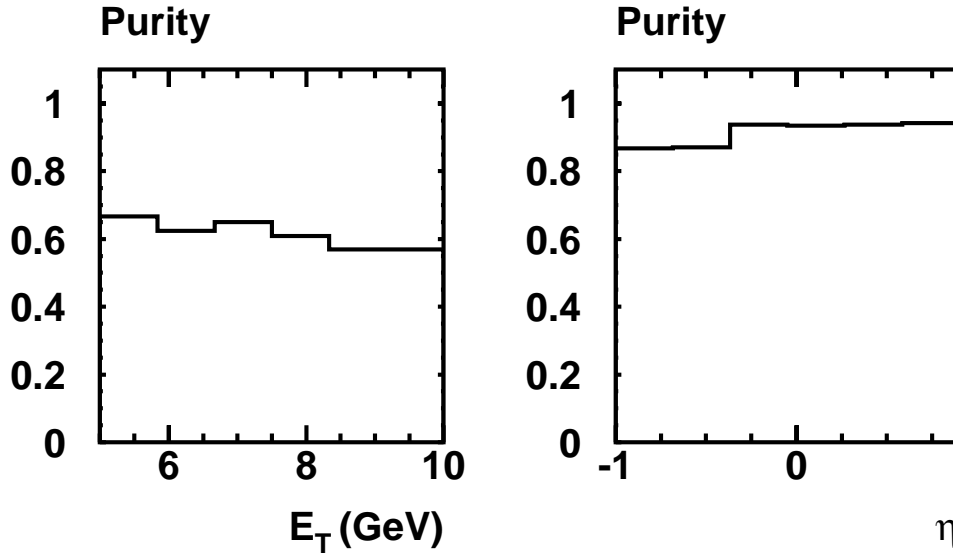


Figure 8.2: Bins purities as a function of E_T and η obtained using PYTHIA prompt photon samples for the full data taking period.

where $\sum_{E_T^\gamma} (\sum_{\eta^\gamma})$ is the sum over a column (row) of the grid discussed in chapter 7. $N(\eta^\gamma, E_T^\gamma)$ is the number of events in the $(\eta^\gamma, E_T^\gamma)$ bin of the grid. $C(\eta^\gamma, E_T^\gamma)$ are the correction factors described in section 8.1.1. $\int L dt = 105 \text{ pb}^{-1}$ is the integrated luminosity of the data. $\Gamma(\eta^\gamma)$ and $\Gamma(E_T^\gamma)$ are the widths of the bins.

8.2 Systematic uncertainties

The possibly insufficient simulations of the showers lead to systematic errors when the signal is extracted by the fits described in chapter 7. Also the errors due the kinematic measurements (mainly energy scale uncertainties) lead to systematic uncertainties on the cross section. Furthermore the assumptions in the used models in PYTHIA lead to errors on the extracted correction factors and eventually on the cross-sections. Various other errors, e.g. the deep inelastic scattering background subtraction, the luminosity measurements, are also discussed. The systematic uncertainties of the final results are obtained by adding the estimated systematic errors given below in quadrature, with the exception of the overall luminosity error. The main systematic errors are shown in figure 8.9.

Shower simulation

Inaccurate shower simulation used by the Monte Carlos, results in differences in the shower

shape distribution between the Monte Carlo samples and the data. The photon finder uses cuts on the shower shape variables leading to a systematic error of 2% (see section 5.1.1).

The shower shapes are also used to extract the signal through a fit (see section 7.3). Electrons selected from the experimental data and simulated electrons are used to estimate the errors on the shower shape variables and to determine correction factors F_{min} , F_{cent} and F_{max} on the simulated shower shape variables as given in table 8.1. Here F_{cent} corresponds to the central

Variables	$\langle R \rangle$			HCF			FLF		
Wheels	CB1	CB2	CB3	CB1	CB2	CB3	CB1	CB2	CB3
F_{min}	0.98	1.015	0.975	1.	1.	1.	0.995	0.97	0.95
F_{cent}	1.0	1.035	1.	1.05	1.05	1.05	1.015	0.99	0.98
F_{max}	1.02	1.045	1.025	1.1	1.1	1.1	1.035	1.01	1.01

Table 8.1: Factors applied to the shower shape variables radius, hot core fraction (HCF), first layer fraction FLF . The factors F are applied in the following way: $\langle R \rangle_{shift} = F \cdot \langle R \rangle$, $HCF_{shift} = F \cdot HCF + (1 - F)$ and $FLF_{shift} = F \cdot FLF$.

value used for the final results. The deviations F_{min} and F_{max} are used to estimate the systematic uncertainty. Figures 8.3, 8.4 and 8.5 show comparisons of shower shape variables for measured and simulated electrons for the three correction factors F_i . For the calculation of the systematic uncertainties, the signal extractions have been performed after applying these shifts to the shower shapes variables. Thereby $\langle R \rangle$ and HCF are varied together as they are strongly correlated. Figures 8.9 a) b) show the final systematic uncertainties obtained in the various bins. They are in the range 10%-20% and constitute the dominant contribution to the total systematic uncertainty.

Variations in the E_T and η distributions of the single particles used in the shower shape analysis (see chapter 7) lead to very small variations of the results of less than 1%.

Uncertainties due to the calorimeter energy scales

The electromagnetic energy calibration was described in section 5.1.2. The systematic errors due to the electromagnetic energy scale uncertainty are obtained by varying the calibrated photon energy by $\pm 0.7\%$ in wheel CB1 and by $\pm 1.5\%$ in wheels CB2 and CB3 according to the precision of the electromagnetic energy calibration for the different parts of the LAr calorimeter. This leads to an uncertainty on the final results smaller than 10% (figures 8.9 c)).

The hadronic energy calibration was described in section 5.2.2. The systematic errors have the following sources and the following variations are applied:

- hadronic LAr energy measurement: 3%
- tracks contributing to the energy measurement: 3%
- SPACAL energy measurement: 7%

The corresponding uncertainties on the final results are below 2% for the hadronic LAr energy measurement, below 1% for the energy measurement by tracks and below 1% for the SPACAL energy measurement.

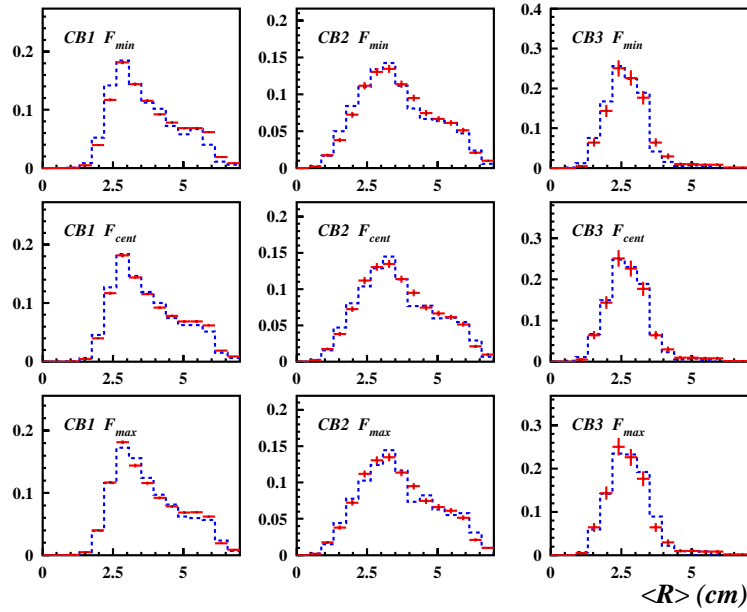


Figure 8.3: Shifts F_{min} , F_{cent} , F_{max} applied to the shower radius for the systematic error estimate (using electrons). The points are the data and the dotted lines are the simulation. The 3 different wheels of the central barrel of the LAr calorimeter (CB1, CB2, CB3) are plotted separately.

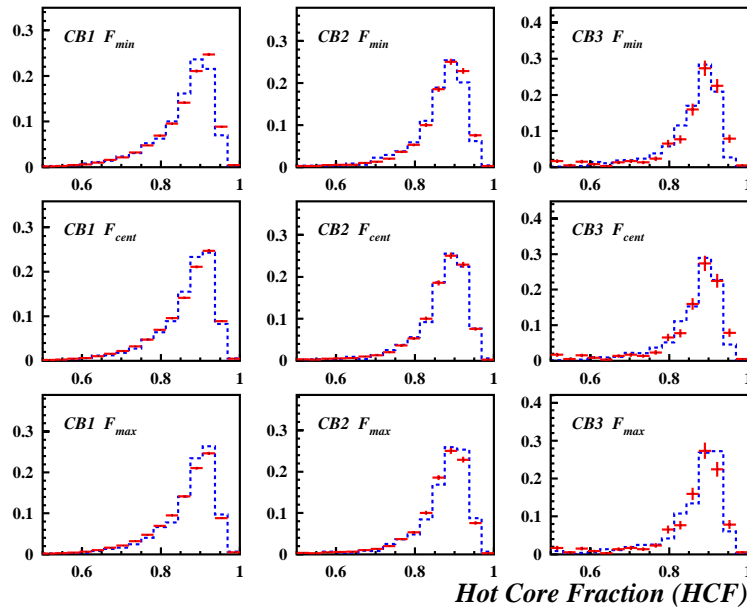


Figure 8.4: Shifts F_{min} , F_{cent} , F_{max} applied to the shower hot core fraction for the systematic error estimate (using electrons). The points are the data and the dotted lines are the simulation. The 3 different wheels of the central barrel of the LAr calorimeter (CB1, CB2, CB3) are plotted separately.

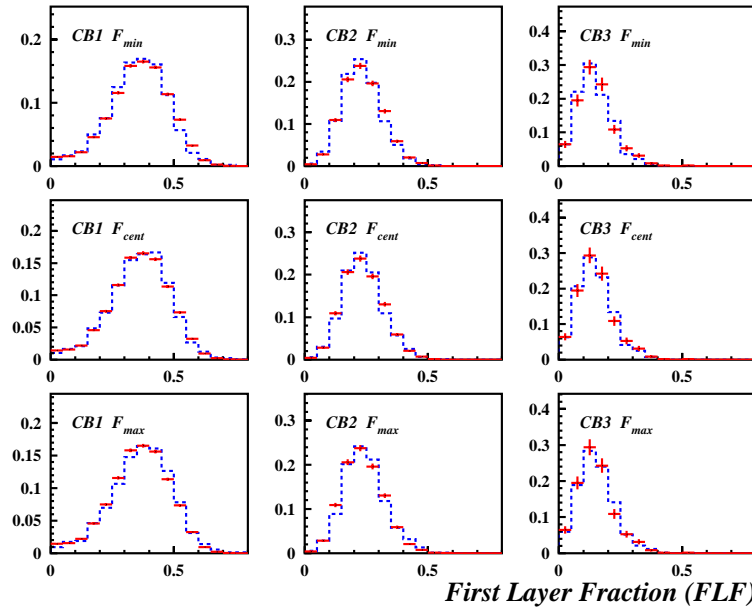


Figure 8.5: Shifts F_{min} , F_{cent} , F_{max} applied to the shower first layer fraction for the systematic error estimate (using electrons). The points are the data and the dotted lines are the simulation. The 3 different wheels of the central barrel of the LAr calorimeter (CB1, CB2, CB3) are plotted separately.

PYTHIA model

The uncertainties on the correction factors by the use of the PYTHIA simulation are estimated by varying the E_T^γ slope in PYTHIA according to figure 8.6. The resulting systematic uncertainties are below 3% (figures 8.9 d)).

Also the isolation description of PYTHIA is taken into account. Weights proportional to E_T^{cone} are applied to the PYTHIA prediction such that for $E_T^{cone} = 0.1 \cdot E_T$ (cut value), weights of 0.5 and 2 are applied. This leads to systematic errors below 3% on the final results (figures 8.9 e)).

DIS background

The cuts applied to reduce DIS background have been discussed in chapter 6. DIS events may still contribute to the prompt photon sample if no track from a scattered electron is linked to the candidate calorimetric cluster. Figure 8.7 shows the cluster-track link efficiency. This efficiency is determined using a selection of NC DIS data. Fiducial cuts have been applied year-wise to exclude central tracker regions with bad efficiency. The obtained overall inefficiency is 0.4%. The error on this estimate is given by the statistical error (10%) on this inefficiency of 0.4%. The events without a track have the same kinematic and shower shape distributions as the events with tracks (figure 8.8). The estimate of the DIS background in the prompt photon sample is obtained using a NC DIS Monte-Carlo sample applying all the cuts of the analysis

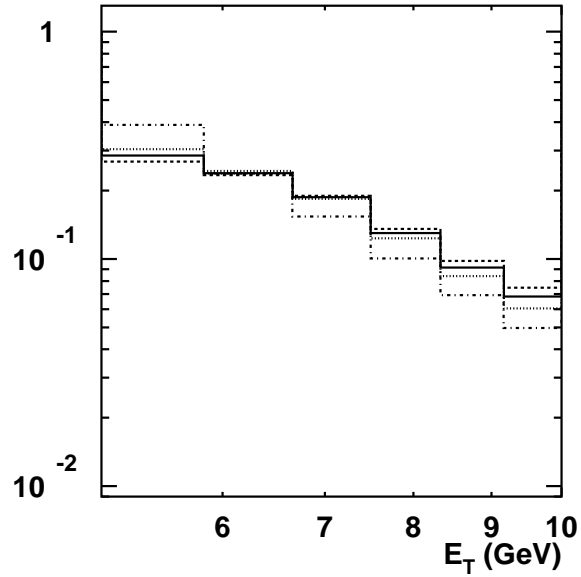


Figure 8.6: Variation of the E_T^γ slope. The E_T^γ slope variations (dotted and dashed histograms) are such that the slope becomes more and less steep than both, the PYTHIA prediction (full histogram), and the next-to-leading order calculation of [14] (dashed-dotted histogram).

with a weight of 0.4% due to the inefficiency. The prompt photon cross sections are corrected for the DIS background. The corrections are below 5 % with an error below 0.5% and are only affecting high E_T and low η bins (Figure 7.14).

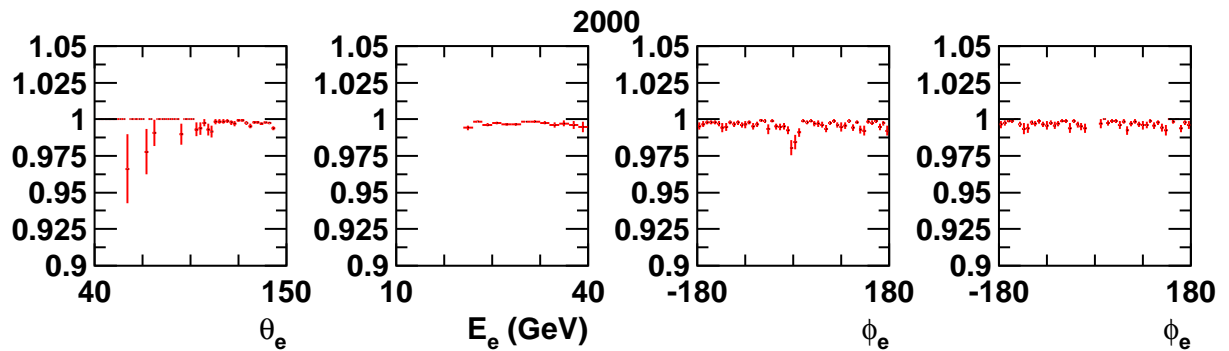


Figure 8.7: Efficiency (2000 data) of the cluster-track link using DTRA and DTNV tracks with a cut at 25 cm (as in the prompt photon analysis). The ϕ distribution is shown before and after fiducial cuts of inefficient central tracker regions (NC DIS events).

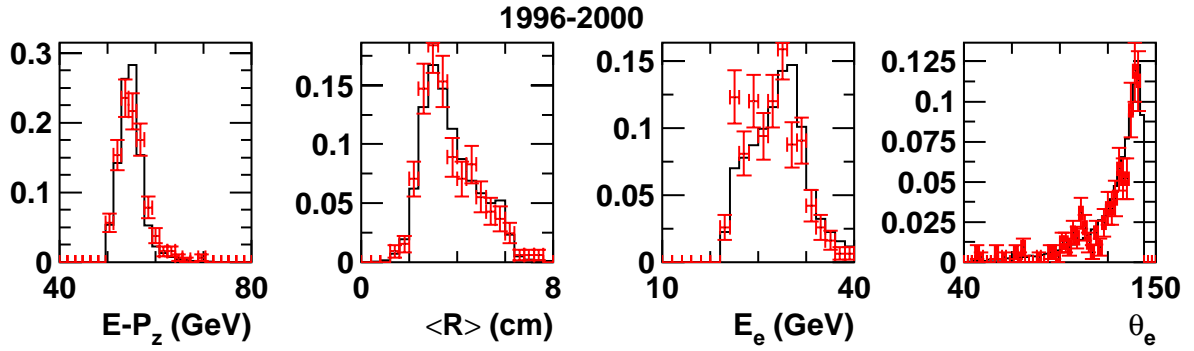


Figure 8.8: Control plots (1996-2000 data) for the efficiency evaluation of the cluster-track link using NC DIS events. The distributions of $E - P_z$, E_e , θ_e , and the shower radius $\langle R \rangle$ for events with a cluster-track link (histograms) and without (points) are compared, all normalized to one.

Luminosity measurement

An overall uncertainty of 1.5 % due to the luminosity measurement is not included in the figures with the final results.

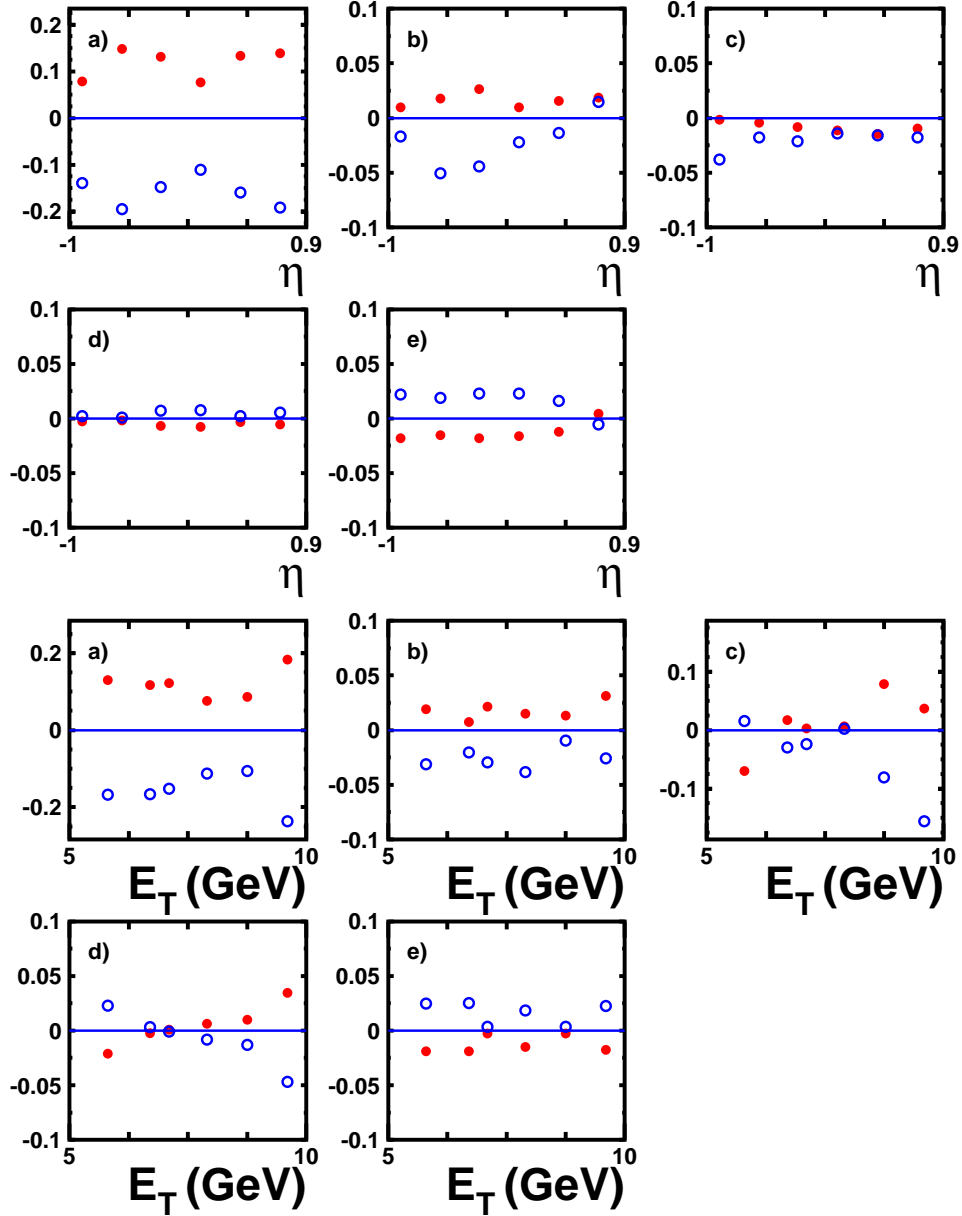


Figure 8.9: Systematic errors for the E_T and η bins calculated for a) $\langle R \rangle$ and HCF, b) FLF, c) electromagnetic energy scale, d) E_T^γ slope, e) isolation variation in PYTHIA.

Chapter 9

Results and comparison to theory

In this chapter the results are presented for photoproduction of prompt photons with $0.2 < y < 0.7$ corresponding to the γp center-of-mass energy range $140 < W_{\gamma p} < 270$ GeV. Inclusive cross sections $ep \rightarrow e\gamma X$ are given as a function of the pseudo-rapidity η^γ , for the transverse energy range $5 < E_T^\gamma < 10$ GeV, and as a function of the transverse energy E_T^γ , for the pseudo-rapidity range $-1 < \eta^\gamma < 0.9$. Cross sections for prompt photons requiring in addition a jet with $E_T^{jet} > 4.5$ GeV and $-1.5 < \eta^{jet} < 2.3$ are also presented. Comparisons are made with the leading-order Monte Carlo programs PYTHIA [58] and HERWIG [64] and with a next-to-leading-order program [14].

9.1 PYTHIA and HERWIG

The PYTHIA [58] and HERWIG [64] Monte-Carlo programs have been described in more detail in section 3.2. The leading order processes were shown in figure 3.3. Contributions from di-jet events where a quark radiates a photon are also included in the PYTHIA samples. For both generators the parton densities GRV (LO) [61, 62] were used for the photon and the proton. The leading order QCD matrix elements are regulated by a minimum cut-off in transverse momentum which is set to 3 GeV. The intrinsic k_T of the partons in the proton was set to 1 GeV. In addition, both generators simulate multiple interactions. Initial and final state radiation (ISR/FSR) are simulated by PYTHIA, but not by HERWIG. By producing PYTHIA samples without ISR/FSR, the latter effect was found to be below 1%.

9.2 NLO calculation

The NLO QCD calculation of the photo-production of prompt photons at HERA by Fontannaz et al [14] is used for comparison with the data. It is described in section 2.1. The calculations include NLO corrections to all the 4 contributions shown in figure 2.3: direct non-fragmentation, direct fragmentation, resolved non-fragmentation, resolved fragmentation. Here fragmentation refers to photons produced in the fragmentation process of quarks or gluons (see section 2.1). It also includes the box diagram shown in figure 2.3 e). This contribution is still sizeable [14, 95] although it is next-to-NLO (NNLO) (fig. 9.1).

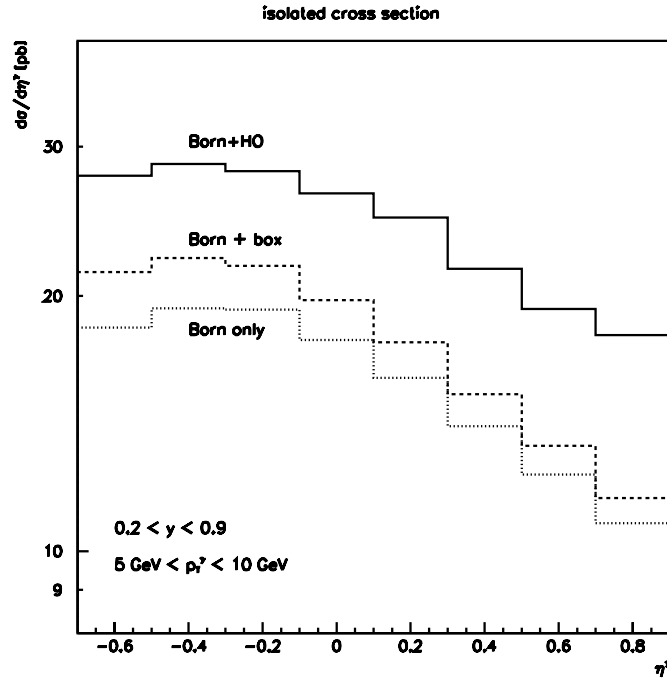


Figure 9.1: Prompt photon differential cross section $d\sigma/d\eta^\gamma$ for $5 < E_T^\gamma < 10 \text{ GeV}$ and $0.2 < y < 0.9$ at HERA kinematics, as predicted by the LO (dotted line), the LO+box (dashed line) and the NLO (full line) calculations (from [14]).

The photon and proton parton densities AFG [96] and MRST2 [97] are used respectively. For the parton-to-photon fragmentation functions the parametrisation by Bourhis et al. [98] has been used. The NLO (and NNLO) corrections increase the cross sections by about 40% [14] (fig. 9.1).

The importance of the fragmentation contribution is considerably reduced by the isolation requirement. This is illustrated in studies by L. Gordon and W. Vogelsang [99] and Fontannaz et al. [14]. The isolation requirement reduces the fragmentation contribution to about 6% of the total cross section (fig.9.2 a,b and 9.3 a) (see also [96]). The contribution of resolved photon interactions is dominant especially at large pseudo-rapidities (fig. 9.3 b). The prediction using GS [101] photon parton densities is much lower (about 40%) than using GRV [61] for negative pseudo-rapidities (fig. 9.3 c). In a ZEUS prompt photon analysis [15] the NLO predictions with GS [101] photon parton densities were much below the data (Fig. 2.6). On the other hand the predictions using AFG [96] and GRV [61] photon parton densities are very close (fig.9.2 c). The sensitivity to proton parton densities is marginal (fig. 9.3 c). The difference resulting from using CTEQ4M [50] or MRST1 [97] for the proton parton densities was found to be of order 3% at most [14]. The processes involving a gluon from the photon dominates the cross section at large positive pseudo-rapidities (fig. 9.3 d). It has however been shown, by varying the gluon distribution in the photon, that there is basically no sensitivity for the pseudo-rapidity range measured in this analysis to the gluon density in the photon [14] (fig.9.2 c,d).

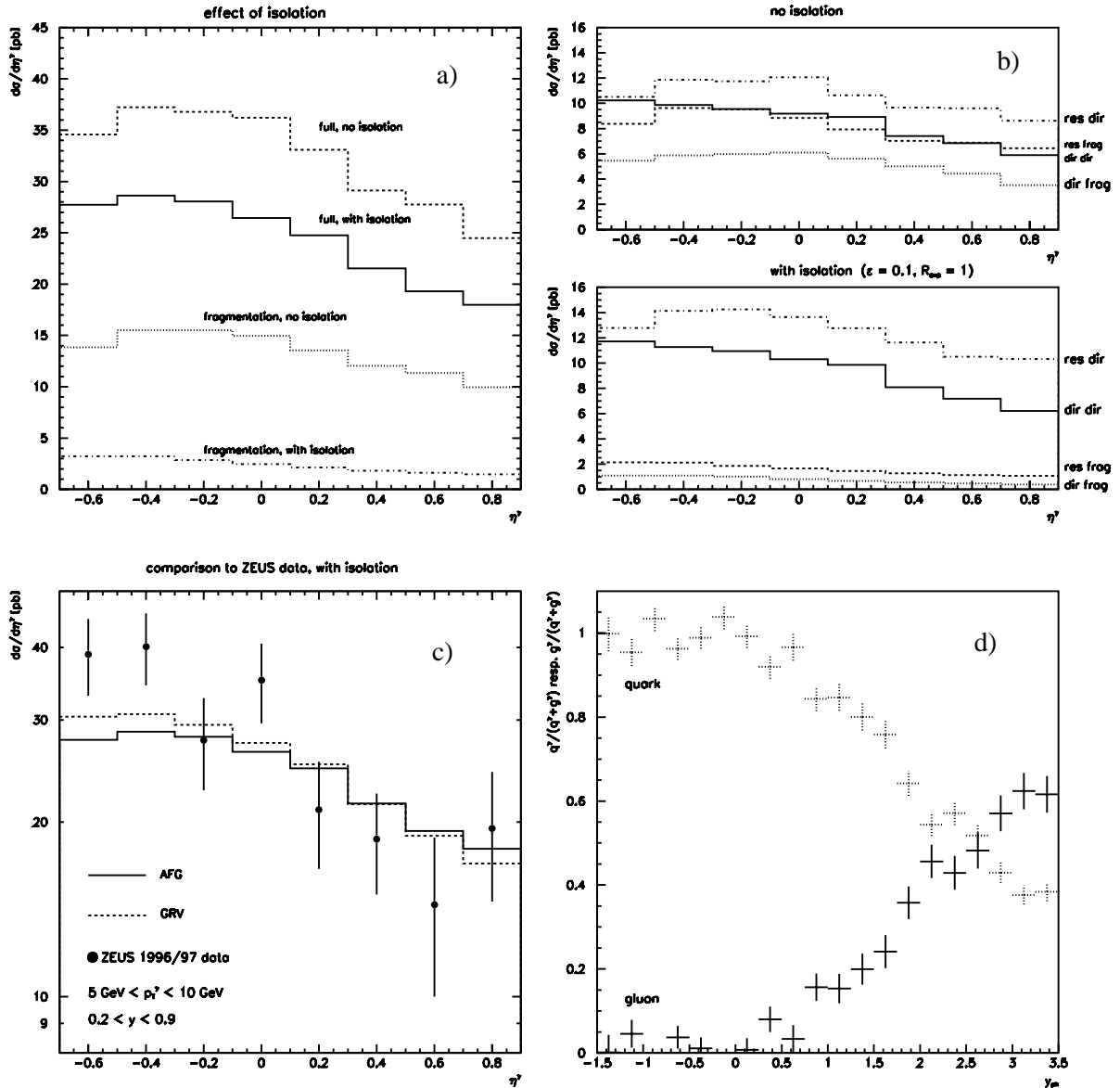


Figure 9.2: The prompt photon cross-sections $d\sigma/d\eta^\gamma$ computed by Fontannaz et al. [14] for $5 < E_T^\gamma < 10 \text{ GeV}$ at HERA kinematics. (a) Comparison of the full cross sections for non-isolated (dashed line) and isolated (full line) prompt photons and the fragmentation cross-sections for non-isolated (dotted line) and isolated (dash-dotted line) prompt photons. (b) Comparison with and without isolation requirement (the cone radius $R=1$ and the cut $\epsilon = 0.1$ were described in chapter 6) of the direct non-fragmentation (dir-dir, full line), direct fragmentation (dir-frag, dotted), resolved non-fragmentation (res-dir, dashed-dotted), resolved fragmentation (res-frag, dashed). (c) Isolated prompt photon cross sections for AFG [96] and GRV [61] photon parton densities and comparison to ZEUS data. (d) Ratio of the contribution of gluon (dotted) and quark (solid) in the photon to the full resolved part of the isolated prompt photon cross section as a function of the pseudo-rapidity η^γ (here named y_{ph}).

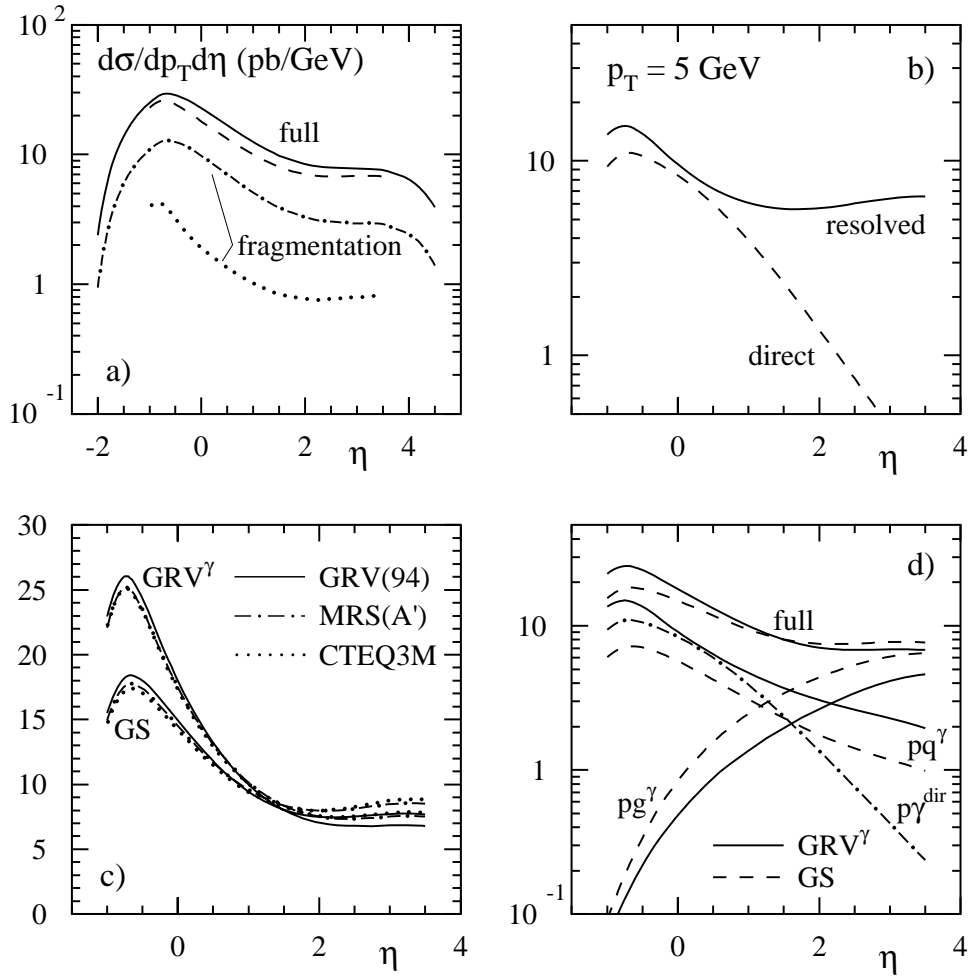


Figure 9.3: The prompt photon cross-sections $d\sigma/d\eta^\gamma$ computed by L. Gordon and W. Vogelsang [99] for $E_T^\gamma > 5$ GeV at HERA kinematics. (a) Comparison of the full cross sections for non-isolated (full line) and isolated (dashed line) prompt photons and the fragmentation cross-section for non-isolated (dashed-dotted line) and isolated (dotted line) prompt photons. (b) Resolved (full line) and direct (dashed line) contributions to the isolated cross-section. (c) Full isolated cross-section for different sets of parton distributions of the proton (GRV(94) [62] (full line), MRS(A') [100] (dashed-dotted), CTEQ3M [50] (dotted)) and of the photon (GRV [61], GS [101]). (d) Full isolated cross section and different direct and resolved subprocesses contributions for GRV (full lines) and GS (dashed lines) photon parton distributions. $p\gamma^{\text{dir}}$ is the direct component, pg^γ (pq^γ) is the resolved component where a gluon (quark) from the photon enters the hard scatter.

9.3 Multiple interactions

Multiple interactions (MI) which are also often described in terms of a so-called soft underlying event, have been described in section 3.1.2. They are not treated in the NLO QCD calculation but may have a sizeable effect on the final results. Indeed, a large fraction of the hadronic energy in the isolation cone may come from the underlying event activity [14]. It was shown in section 7.4.3, by varying the isolation requirements, that PYTHIA reproduces very well the hadronic energy in the isolation cone. Samples of PYTHIA events without MI were simulated for comparison. Figures 9.4 shows the cross sections by PYTHIA, $d\sigma/dE_T^\gamma$ and $d\sigma/d\eta^\gamma$, with and without multiple interactions. Due to the isolation requirement the cross section is reduced, when including multiple interactions, by about 25% for positive pseudo-rapidities. Figures 9.4 shows also besides the full PYTHIA prediction, separately the component where a final state quark in di-jet events radiates a photon and the contribution of the resolved interactions of the exchanged photon.

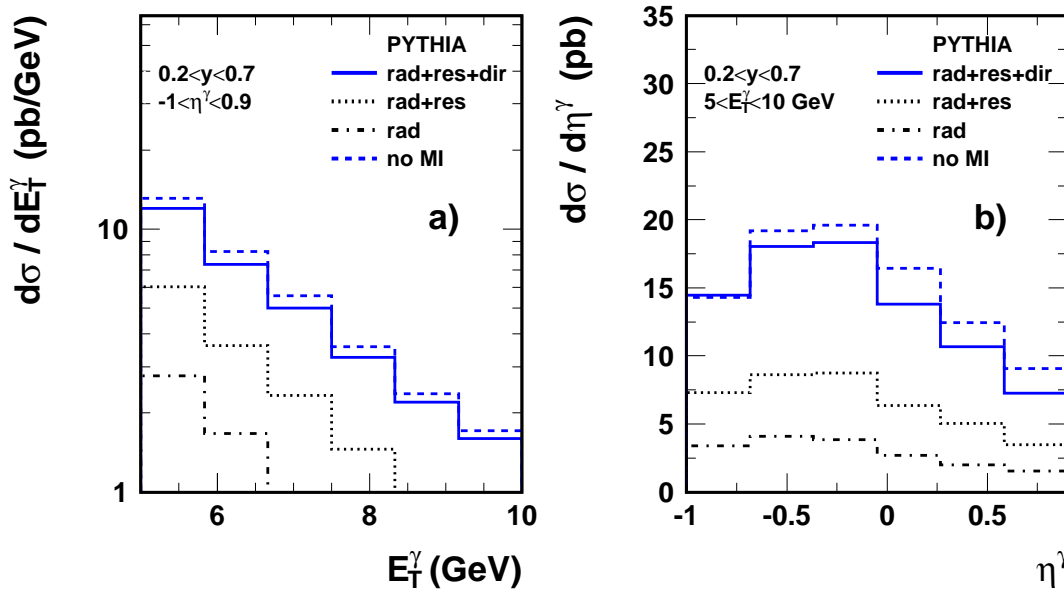


Figure 9.4: Prompt photon differential cross sections $d\sigma/dE_T^\gamma$ for $-1 < \eta^\gamma < 0.9$ (a) and $d\sigma/d\eta^\gamma$ for $5 < E_T^\gamma < 10$ GeV (b) at $\sqrt{s} = 318$ GeV and $0.2 < y < 0.7$, as predicted by the PYTHIA generator [63] including MI (full line) and without (dashed line). Also shown are, for the case of MI, the contribution from di-jet events where a final state quark radiates a photon (dashed-dotted) and this component summed with resolved photon events (dotted line).

9.4 Cross section of inclusive prompt photon production

The cross section extraction of prompt photon production using the data taken by H1 during the years 1996 to 2000 (105 pb^{-1}) has been described in chapter 8. The resulting cross sections are given here for the selection: $0.2 < y < 0.7$, $5 < E_T^\gamma < 10 \text{ GeV}$, $-1 < \eta^\gamma < 0.9$, $E_T^{\text{cone}}/E_T^\gamma < 0.1$ and $Q^2 < 1 \text{ GeV}^2$. Figure 9.5 shows the cross sections $d\sigma/dE_T^\gamma$ and $d\sigma/d\eta^\gamma$ and a comparison to LO and NLO QCD predictions using the code described in [14]. The inner error bars are the statistical errors. They are given by the likelihood fit (chapter 7) and are sensitive to both the number of selected events and the discrimination power for the used discriminator. The outer error bars include systematic errors (chapter 8) added in quadrature.

The NLO QCD calculation describes the data quite well in the presented η^γ and E_T^γ ranges with a tendency to overshoot the data especially at large η^γ where the multiple interactions effect gets larger. Figure 9.5 also shows the NLO prediction corrected for the multiple interactions effect. This effect is estimated using PYTHIA (see section 9.3). The description of the data by the NLO calculation is improved after this correction.

Figure 9.6 shows the comparison to PYTHIA and HERWIG. The PYTHIA simulation describes the data well in shape, is however low in normalisation. The HERWIG prediction is even lower because the contributions from di-jet events where a final state quark radiates a photon are not included.

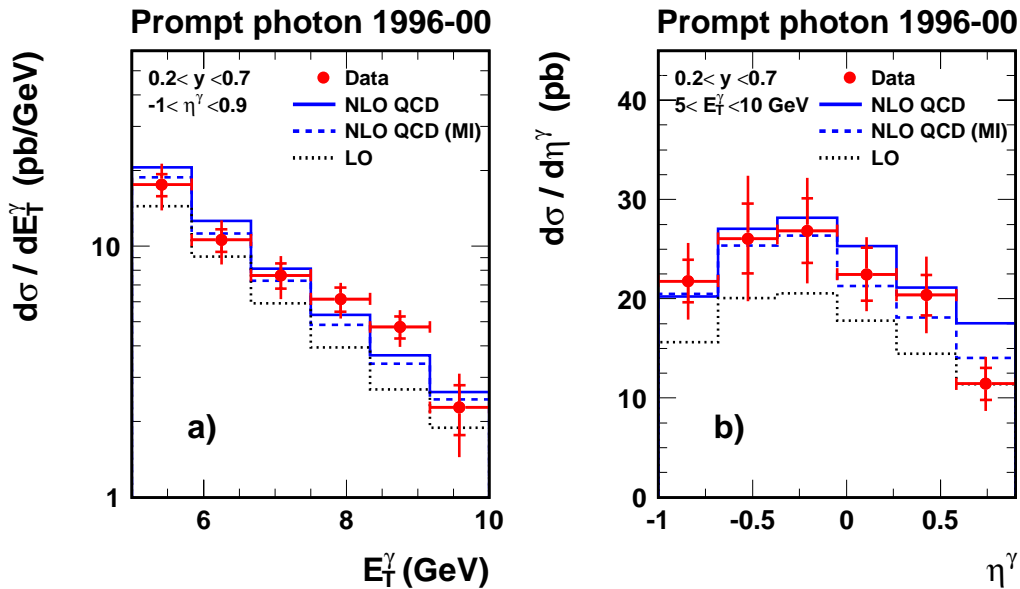


Figure 9.5: Prompt photon differential cross sections $d\sigma/dE_T^\gamma$ for $-1 < \eta^\gamma < 0.9$ (a) and $d\sigma/d\eta^\gamma$ for $5 < E_T^\gamma < 10 \text{ GeV}$ (b) at $\sqrt{s} = 318 \text{ GeV}$ and $0.2 < y < 0.7$ compared to the prediction of LO (dotted line) and NLO (full line) pQCD calculations [14]. The dashed line shows the NLO prediction corrected for the multiple interactions effect predicted by PYTHIA.

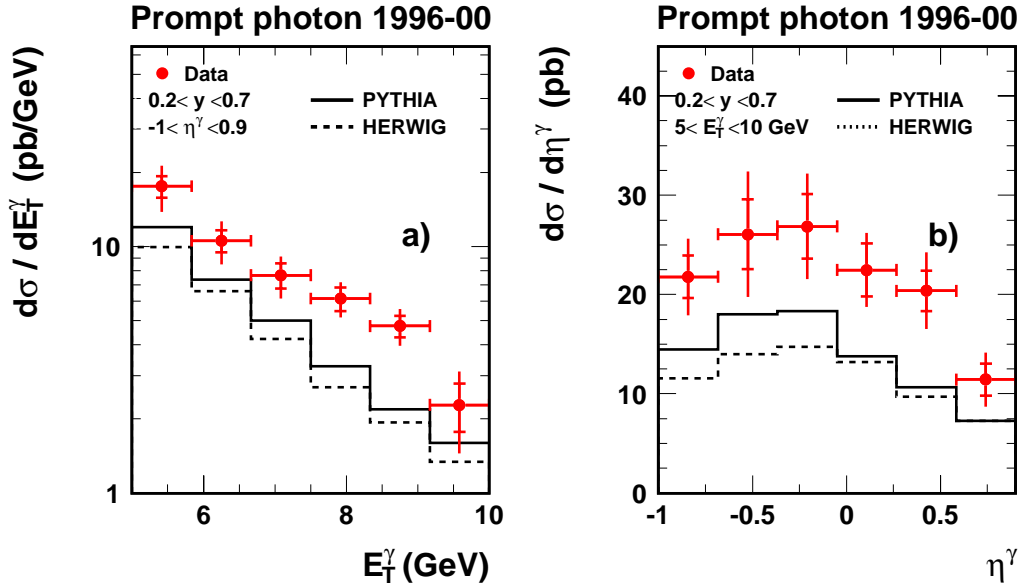


Figure 9.6: Prompt photon differential cross sections $d\sigma/dE_T^\gamma$ for $-1 < \eta^\gamma < 0.9$ (a) and $d\sigma/d\eta^\gamma$ for $5 < E_T^\gamma < 10$ GeV (b) at $\sqrt{s} = 318$ GeV and $0.2 < y < 0.7$ compared to the PYTHIA prediction (full line) and the HERWIG prediction (dashed line).

9.5 Comparison to ZEUS results

The latest published results from the ZEUS experiment were based on an integrated luminosity of 38.4 pb^{-1} using 1996 and 1997 data [15–18]. The cross-section was given as a function of the pseudo-rapidity η and transverse energy E_T for $E_T > 5$ GeV and in the γp center-of-mass energy range 134–285 GeV. Comparisons were made with NLO QCD calculations. Good agreement is observed for the E_T distributions but for negative η all predictions are below the ZEUS data. Figure 9.7 shows the cross-section of the present analysis with the cuts applied in the ZEUS analysis. The data are consistent, but the H1 data are somewhat lower at small η^γ , where the ZEUS data results appear to exceed the NLO calculation. At positive pseudo-rapidities the NLO calculation has also the tendency to overshoot the ZEUS data. This may be due to the multiple interactions effect (see previous sections).

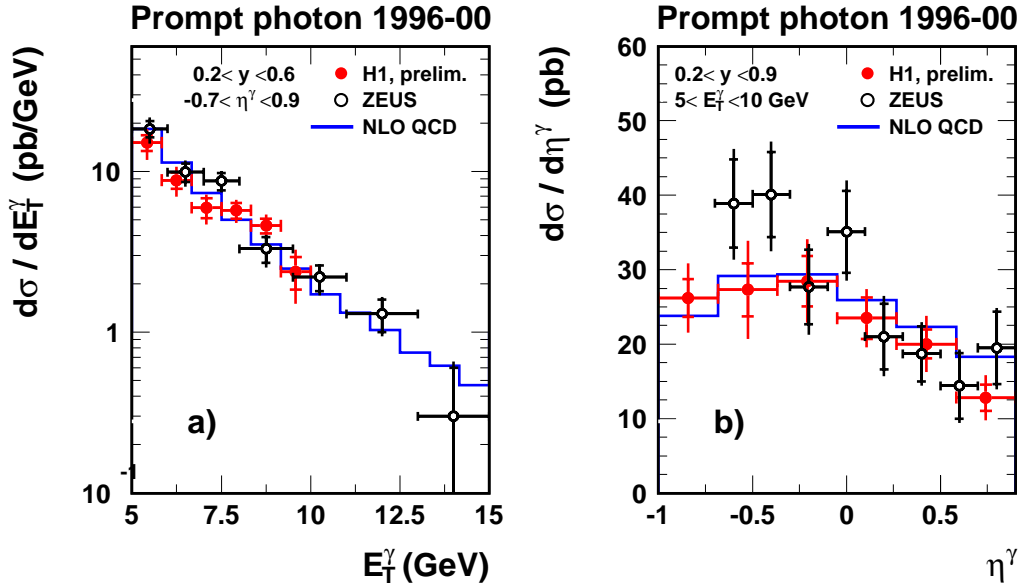


Figure 9.7: Prompt photon differential cross-sections $d\sigma/dE_T^\gamma$ for $-0.7 < \eta^\gamma < 0.9$ (a) and $d\sigma/d\eta^\gamma$ for $5 < E_T^\gamma < 10$ GeV (b) corrected for $\sqrt{s} = 300$ GeV and $0.2 < y < 0.9$ compared to results of the ZEUS collaboration [15]. Also shown is the prediction of a NLO pQCD calculation [14].

9.6 Cross section of Prompt Photon + jet production

The requirement of a jet in addition to the prompt photon allows to define additional observables which may provide a more detailed description of the underlying partonic process than in the inclusive case. For example, the fraction of incoming photon energy participating in the hard interaction x_γ or the fraction of incoming proton energy participating in the hard interaction x_p could be measured. Also the effective parton intrinsic transverse momentum $\langle k_T \rangle$ in the proton can be extracted using the acollinearity of the photon-jet system [16].

The cut on E_T^{jet} has to be different from the cut on E_T^γ . Indeed, it has been observed that for symmetric cuts on E_T^{jet} and E_T^γ , the NLO pQCD calculations lose their predictive power [102–104]. Figure 9.8 shows the obtained LO and NLO cross-section prediction $d\sigma/dE_T^\gamma$ with the conditions $E_T^\gamma, E_T^{jet} > 5$ GeV and $-1.5 < \eta^{jet} < 2.3$ in addition to the selection cuts of the inclusive case (see section 9.4). Close to the cut region $E_T^\gamma > 5$ (first bin) the NLO prediction drops unphysically. Similar effects have been observed in di-jet analyses when the same $E_{T,min}$ was required for both jets [105].

In this analysis we limit ourselves to the measurement of the cross sections $d\sigma/dE_T^\gamma$ and $d\sigma/d\eta^\gamma$ when in addition to the previous selection of inclusive prompt photons a jet is required with $E_T^{jet} > 4.5$ GeV and $-1.5 < \eta^{jet} < 2.3$.

Figure 9.9 shows the cross sections $d\sigma/dE_T^\gamma$ and $d\sigma/d\eta^\gamma$ and a comparison to LO and NLO QCD prediction [14]. The inner error bars are the statistical errors. The outer error bars include systematic errors (chapter 8) added in quadrature. Due to the jet requirement the cross sections

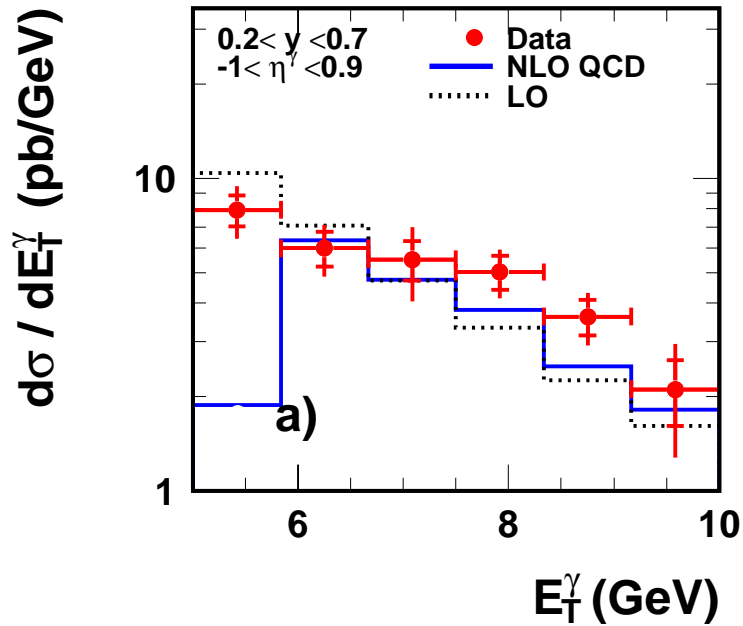


Figure 9.8: Prompt photon + jet differential cross section $d\sigma/dE_T^\gamma$ as given by the LO (dashed line) and NLO (full line) pQCD calculations [14] using symmetric cuts in E_T^γ and E_T^{jet} . The cross sections are for $-1 < \eta^\gamma < 0.9$ requiring a jet with $E_T^\gamma, E_T^{jet} > 5$ GeV and $-1.5 < \eta^{jet} < 2.3$ and at $\sqrt{s} = 318$ GeV and $0.2 < y < 0.7$. The data points are also shown.

are about 35% lower than in the inclusive case. The η^γ distributions are very similar in shape to the inclusive case. The E_T^γ distributions are somewhat more flat at low E_T^γ values. This is due to the cut $E_T^{jet} > 4.5$ GeV which reduces strongly the cross sections when E_T^γ is low in the used range and has less effect when E_T^γ is large. The higher order corrections to the direct non-fragmentation term are negative and those for the resolved term are positive. For the chosen cuts, the NLO result is lower than the LO result for negative pseudo-rapidities. The errors bars are somewhat larger than for the inclusive case but the tendency of the NLO QCD calculation to overshoot the data especially at large η^γ remains. Figure 9.9 also shows the NLO prediction corrected for the multiple interactions effect (see also sections 9.3 and 9.4). As in the inclusive case, the description of the data by the NLO calculation is improved after this correction.

Figure 9.10 shows the comparison to PYTHIA and HERWIG. As in the inclusive case, the PYTHIA simulation describes the data well in shape, is however low in normalisation. The HERWIG prediction is even lower because the contributions from di-jet events where a final state quark radiates a photon are not included.

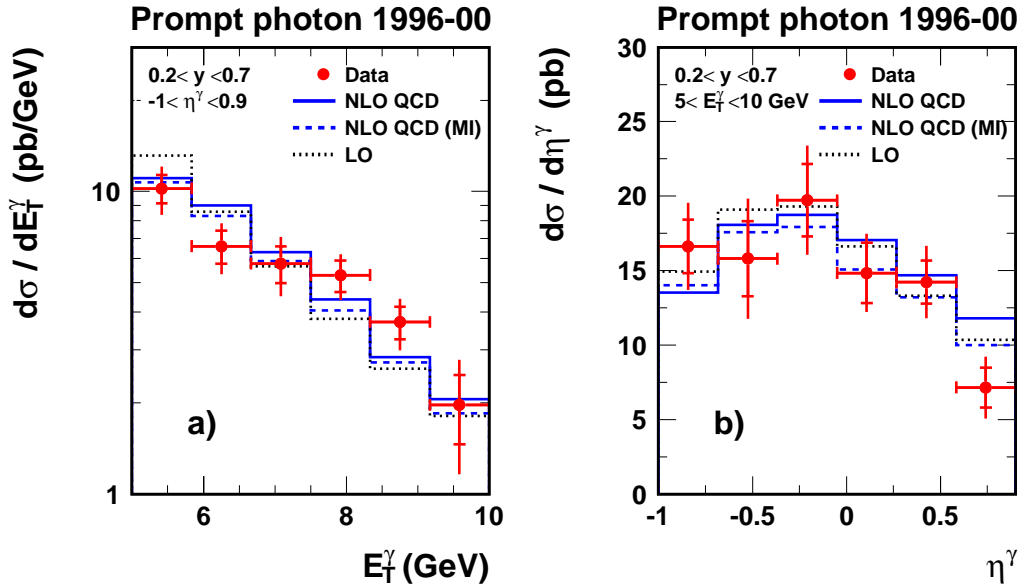


Figure 9.9: Prompt photon + jet differential cross sections $d\sigma/dE_T^\gamma$ for $-1 < \eta^\gamma < 0.9$ (a) and $d\sigma/d\eta^\gamma$ for $5 < E_T^\gamma < 10$ GeV (b) requiring a jet with $E_T^{jet} > 4.5$ GeV and $-1.5 < \eta^{jet} < 2.3$ and at $\sqrt{s} = 318$ GeV and $0.2 < y < 0.7$ compared to the prediction of LO (dashed line) and NLO (full line) pQCD calculations [14].

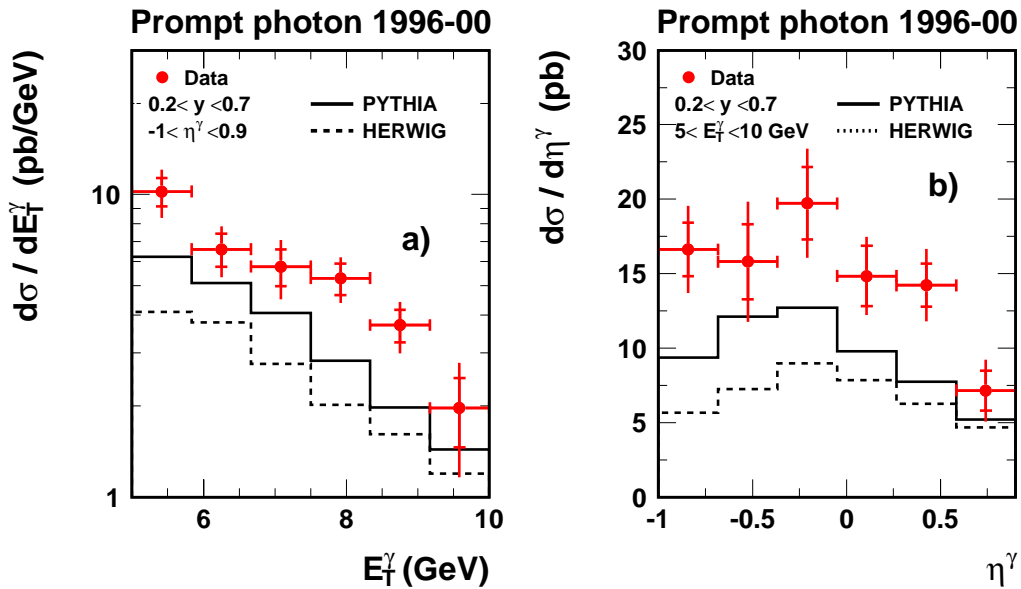


Figure 9.10: Prompt photon + jet differential cross sections $d\sigma/dE_T^\gamma$ for $-1 < \eta^\gamma < 0.9$ (a) and $d\sigma/d\eta^\gamma$ for $5 < E_T^\gamma < 10$ GeV (b) requiring a jet with $E_T^{jet} > 4.5$ GeV and $-1.5 < \eta^{jet} < 2.3$ and at $\sqrt{s} = 318$ GeV and $0.2 < y < 0.7$ compared to the PYTHIA prediction (full line) and the HERWIG prediction (dashed line).

Chapter 10

Summary and outlook

In this thesis a measurement of prompt photons in photo-production was presented using data taken between years 1996 and 2000 by the H1 detector at the ep collider HERA. The data have been collected in different data taking periods with electrons or positrons with energy $E_e = 27.5$ GeV colliding with protons of energies $E_p = 820$ GeV or $E_p = 920$ GeV. The data correspond to an integrated luminosity of 105 pb^{-1} of which 28.8 pb^{-1} and 58.6 pb^{-1} are recorded in e^+p interactions at center of mass energies $\sqrt{s} = 300$ GeV and $\sqrt{s} = 318$ GeV respectively, and 14.9 pb^{-1} in e^-p interactions at $\sqrt{s} = 318$ GeV.

The prompt photon processes are sensitive to the partonic structure of the photon and of the proton. The reactions provide clean QCD tests, because an isolated photon at large transverse energy E_T^γ can be measured directly. This is in contrast to jet studies where the partonic structure is hidden behind the non perturbative hadronisation process. The cross sections are however smaller for prompt photons and the background situation is more difficult.

The selection of the prompt photon candidates in the liquid Argon calorimeter has been presented. Cuts have been applied to select prompt photon candidates and to reject non- ep -background, Compton events, neutral current deep-inelastic-scattering events and neutral mesons in hadronic jets. After all selection cuts, the background is still of similar size as the prompt photon signal. The signal is extracted exploiting a combination of discriminating shower shape functions in a likelihood analysis. Distributions of the γ candidates are fitted by a sum of contributions of simulated photons, π^0 and η mesons.

The data are corrected for detector effects by a detailed simulation of prompt photon production in the H1 detector using the PYTHIA event generator [63]. The background estimate of PYTHIA is not used in the analysis. Only the η/π^0 fraction in the background ($\approx 5\%$ after selection) is taken from the generator. The systematic error is dominated by the potentially not perfect simulation of the shower shapes.

The results are presented as ep cross sections. The cross sections obtained at $\sqrt{s} = 300$ GeV are transformed to $\sqrt{s} = 318$ GeV by corrections of about 4% taken from PYTHIA. The extracted cross sections $d\sigma/dE_T^\gamma$ and $d\sigma/d\eta^\gamma$ were measured at $\sqrt{s} = 318$ GeV and $0.2 < y < 0.7$, corresponding to the γp center-of-mass energy range $[140 - 270]$ GeV, for photon virtualities $Q^2 < 1 \text{ GeV}^2$, including the photon isolation condition $E_T^{cone} = 0.1 \cdot E_T^\gamma$.

The cross-sections were confronted with the event generators PYTHIA [63] and HERWIG [64] based on leading order QCD matrix elements and leading logarithmic parton showers

and with NLO pQCD calculations using the program of Fontannaz, Guillet and Heinrich [14]. The PYTHIA event generator describes the data distributions well in shape with a normalisation that is about 30% low. The HERWIG prediction does not include the contributions from di-jet events, where a final state quark radiates a photon, and is even lower. PYTHIA describes well the dependence of the measured cross sections on the chosen cut on the isolation cone.

The data are quite well described in the covered η^γ and E_T^γ range by the NLO pQCD calculation, but the prediction is above the data in the forward region ($\eta^\gamma > 0.6$) which could be related to underlying event activity not contained in the NLO calculation. The cross sections $d\sigma/dE_T^\gamma$ and $d\sigma/d\eta^\gamma$ requiring an additional jet with $E_T^{jet} > 4.5$ GeV and $-1.5 < \eta^{jet} < 2.3$ have been measured and compared to the theoretical calculations with similar conclusions to the inclusive case.

The cross sections in the range $-0.7 < \eta^\gamma < 0.9$ and $0.2 < y < 0.9$ are roughly consistent with results from the ZEUS collaboration [15], which however tend to be higher at negative η^γ .

More insight in the prompt photon production processes could be gained by further studies. The cross sections as a function of the jet transverse energy E_T^{jet} , the jet pseudo-rapidity η^{jet} , the fraction of incoming photon energy participating in the hard interaction x_γ , the fraction of incoming proton energy participating in the hard interaction x_p could be measured. Furthermore a study of the effective parton intrinsic transverse momentum $\langle k_T \rangle$ in the proton can be carried out using the acollinearity of the photon-jet system [16]. Indeed discrepancies of the measured prompt photons with the predictions in hadronic measurements were suspected to be due to an theoretically under-estimated $\langle k_T \rangle$. Prompt photon production measurements using the data taken at HERA in future, will due to improved statistics reduce the errors on the cross sections and help to better constrain the parton densities of the photon and contribute to a better understanding of QCD.

Bibliography

- [1] R. P. Feynman, Phys. Rev. Lett. **23** (1969) 1415.
- [2] C. G. Callan and D. J. Gross, Phys. Rev. Lett. **22** (1969) 156.
- [3] T. Eichten *et al.*, Phys. Lett. B **46** (1973) 274.
- [4] V. N. Gribov and L. N. Lipatov, Yad. Fiz. **15** (1972) 781 [Sov. J. Nucl. Phys. **15** (1972) 438].
- [5] L. N. Lipatov, Sov. J. Nucl. Phys. **20** (1975) 94 [Yad. Fiz. **20** (1974) 181].
- [6] Y. L. Dokshitzer, Sov. Phys. JETP **46** (1977) 641 [Zh. Eksp. Teor. Fiz. **73** (1977) 1216].
- [7] G. Altarelli and G. Parisi, Nucl. Phys. B **126** (1977) 298.
- [8] R. Petronzio and W. Furmanski,
*In *Bad Honnef 1980, Proceedings, Current Topics In Elementary Particle Physics*, 23-47.*
- [9] J. J. Sakurai, Phys. Rev. Lett. **22** (1969) 981.
- [10] C. F. von Weizsacker, Z. Phys. **88** (1934) 612.
- [11] L. E. Gordon, hep-ph/9706355.
- [12] L. E. Gordon and W. Vogelsang, hep-ph/9606457.
- [13] M. Krawczyk and A. Zembrzuski, hep-ph/9810253.
- [14] M. Fontannaz, J. P. Guillet and G. Heinrich, Eur. Phys. J. C **21** (2001) 303
- [15] J. Breitweg *et al.* [ZEUS Collaboration], Phys. Lett. B **472** (2000) 175
- [16] S. Chekanov *et al.* [ZEUS Collaboration], Phys. Lett. B **511** (2001) 19
- [17] Anthony W. Vaiciulis thesis,
Observation of isolated high-ET photons in photo-production at HERA, (1999)
- [18] Sung Won Lee thesis, *Measurement of prompt photons photo-production at HERA*, (2000)
- [19] H1 Collaboration, Proc.. Phys. Soc. Conference, Jerusalem 1997,
- [20] P. Darriulat *et al.*, Nucl. Phys. B **110** (1976) 365.
- [21] E. Amaldi *et al.*, Phys. Lett. B **77** (1978) 240.
- [22] E. Anassontzis *et al.*, Z. Phys. C **13** (1982) 277.

- [23] M. McLaughlin *et al.*, Phys. Rev. Lett. **51** (1983) 971.
- [24] P. Astbury *et al.* [NA14 Collaboration], Phys. Lett. B **152** (1985) 419.
- [25] J. Badier *et al.* [NA3 Collaboration], Z. Phys. C **31** (1986) 341.
- [26] C. De Marzo *et al.* [NA24 Collaboration], Phys. Rev. D **36** (1987) 8.
- [27] M. Bonesini *et al.* [WA70 Collaboration], Z. Phys. C **37** (1988) 535.
- [28] M. Bonesini *et al.* [WA70 Collaboration], Z. Phys. C **38** (1988) 371.
- [29] C. Albajar *et al.* [UA1 Collaboration], Phys. Lett. B **209** (1988) 385.
- [30] J. Alitti *et al.* [UA2 Collaboration], Phys. Lett. B **263** (1991) 544.
- [31] J. Alitti *et al.* [UA2 Collaboration], Phys. Lett. B **288** (1992) 386.
- [32] J. Alitti *et al.* [UA2 Collaboration], Phys. Lett. B **299** (1993) 174.
- [33] G. Sozzi *et al.* [UA6 Collaboration], Phys. Lett. B **317** (1993) 243.
- [34] G. Ballocci *et al.* [UA6 Collaboration], Phys. Lett. B **436** (1998) 222.
- [35] F. Abe *et al.* [CDF Collaboration], Phys. Rev. Lett. **68** (1992) 2734.
- [36] F. Abe *et al.* [CDF Collaboration], Phys. Rev. Lett. **70** (1993) 2232.
- [37] F. Abe *et al.* [CDF Collaboration], Phys. Rev. D **48** (1993) 2998.
- [38] F. Abe *et al.* [CDF Collaboration], Phys. Rev. Lett. **73** (1994) 2662
- [39] D. Acosta *et al.* [CDF Collaboration], Phys. Rev. D **65** (2002) 112003
- [40] S. Abachi *et al.* [D0 Collaboration], Phys. Rev. Lett. **77** (1996) 5011
- [41] B. Abbott *et al.* [D0 Collaboration], Phys. Rev. Lett. **84** (2000) 2786
- [42] L. Apanasevich *et al.*, Phys. Rev. D **59** (1999) 074007
- [43] D. Decamp *et al.* [ALEPH Collaboration], Phys. Lett. B **264** (1991) 476.
- [44] D. Buskulic *et al.* [ALEPH Collaboration], Z. Phys. C **69** (1996) 365.
- [45] P. Abreu *et al.* [DELPHI Collaboration], Z. Phys. C **53** (1992) 555.
- [46] O. Adriani *et al.* [L3 Collaboration], Phys. Lett. B **292** (1992) 472.
- [47] M. Z. Akrawy *et al.* [OPAL Collaboration], Phys. Lett. B **246** (1990) 285.
- [48] G. Alexander *et al.* [OPAL Collaboration], Phys. Lett. B **264** (1991) 219.
- [49] J. Breitweg *et al.* [ZEUS Collaboration], Phys. Lett. B **413** (1997) 201
- [50] H. L. Lai *et al.*, Phys. Rev. D **51** (1995) 4763
- [51] J. Huston, E. Kovacs, S. Kuhlmann, H. L. Lai, J. F. Owens and W. K. Tung, Phys. Rev. D **51** (1995) 6139

- [52] S. Catani, M. L. Mangano, P. Nason, C. Oleari and W. Vogelsang, JHEP **9903** (1999) 025
- [53] N. Kidonakis and J. F. Owens, Phys. Rev. D **61** (2000) 094004
- [54] E. Laenen, G. Sterman and W. Vogelsang, Phys. Rev. Lett. **84** (2000) 4296
- [55] K. Ackerstaff *et al.* [OPAL Collaboration], Eur. Phys. J. C **2** (1998) 39
- [56] B. Andersson, G. Gustafson, G. Ingelman and T. Sjostrand, Phys. Rept. **97**, 31 (1983).
- [57] T. Sjostrand, Comput. Phys. Commun. **82** (1994) 74.
- [58] T. Sjostrand, L. Lonnblad and S. Mrenna, hep-ph/0108264.
- [59] G. Marchesini, B. R. Webber, G. Abbiendi, I. G. Knowles, M. H. Seymour and L. Stanco, Comput. Phys. Commun. **67** (1992) 465.
- [60] S. Aid *et al.* [H1 Collaboration], Z. Phys. C **70** (1996) 17
- [61] M. Glück, E. Reya and A. Vogt, Phys. Rev. D **46**, 1973 (1992).
- [62] M. Glück, E. Reya and A. Vogt, Z. Phys. C **67** (1995) 433.
- [63] T. Sjostrand, P. Eden, C. Friberg, L. Lonnblad, G. Miu, S. Mrenna and E. Norrbin, Comput. Phys. Commun. **135** (2001) 238
- [64] G. Marchesini, B. R. Webber, G. Abbiendi, I. G. Knowles, M. H. Seymour and L. Stanco, Comput. Phys. Commun. **67** (1992) 465.
- [65] G. Corcella *et al.*, hep-ph/9912396.
- [66] H. Jung, Comput. Phys. Commun. **86** (1995) 147.
- [67] I. Abt *et al.* [H1 Collaboration], Nucl. Instrum. Meth. A **386** (1997) 310.
- [68] I. Abt *et al.* [H1 Collaboration], Nucl. Instrum. Meth. A **386** (1997) 348.
- [69] W. Heitler *et al.*,
The quantum theory of radiation 3^d edition, Oxford University Press, London (1954)
- [70] B. Rossi *et al.*, *High Energy Physics* Prentice Hall (1952)
- [71] E. Longo and I. Sestili, Nucl. Instrum. Meth. **128** (1975) 283 [Erratum-ibid. **135** (1976) 587].
- [72] C. W. Fabjan, CERN-EP-85-54
- [73] U. Amaldi, in *C80-06-16.25* Phys. Scripta **23** (1981) 409.
- [74] B. Andrieu *et al.* [H1 Calorimeter Group Collaboration], Nucl. Instrum. Meth. A **336** (1993) 460.
- [75] B. Andrieu *et al.* [H1 Calorimeter Group Collaboration], Nucl. Instrum. Meth. A **350** (1994) 57.
- [76] B. Andrieu *et al.* [H1 Calorimeter Group Collaboration], Nucl. Instrum. Meth. A **336** (1993) 499.
- [77] T. Nicholls *et al.* [H1 SPACAL Group Collaboration], Nucl. Instrum. Meth. A **374** (1996) 149.
- [78] R. D. Appuhn *et al.* [H1 SPACAL Group Collaboration], Nucl. Instrum. Meth. A **386** (1997) 397.

- [79] R. D. Appuhn *et al.* [H1 SPACAL group Collaboration], Nucl. Instrum. Meth. A **382** (1996) 395.
- [80] J. Burger *et al.*, Nucl. Instrum. Meth. A **279** (1989) 217.
- [81] R. Brun *et al.*, *GEANT3 user's guide*, CERN-DD/EE-84-1 (1987).
- [82] S. Peters thesis, *Die parametrisierte Simulation elektromagnetischer Schauer* (1992)
- [83] M. Rudowicz thesis, *Hadronische Schauersimulation fuer den H1-Detektor* (1992)
- [84] P. Loch thesis, *Kalibration des H1 fluessig-Argon Kalorimeters unter beruecksichtigung der Gewichtungsmethode fuer Teilchenjets* (1992)
- [85] L. Goerlich, H.P. Wellisch H1 Internal Note, H1-IN-204 (1991)
- [86] V. Shekelyan H1 Internal Note, H1-04/93-288 (1993)
- [87] J. Marks *QESCAT - e identification software in HIPHAN*
http://www-h1.desy.de/~marks/electron/phan_e_finder.html
- [88] C. Adloff *et al.* [H1 Collaboration], Z. Phys. C **74** (1997) 221
- [89] B. Heinemann thesis, *Measurement of charged current and neutral current cross-sections in positron-proton collisions at $\sqrt{s} \approx 300$ GeV* (1992)
- [90] C. Adloff *et al.* [H1 Collaboration], Nucl. Phys. B **545** (1999) 3
- [91] S. D. Ellis and D. E. Soper, Phys. Rev. D **48** (1993) 3160
- [92] S. D. Ellis and D. E. Soper, Phys. Rev. D **48** (1993) 3160
- [93] D. Karlen, Computers in Physics, 12:4 (1998) 380
- [94] R. J. Barlow and C. Beeston, Comput. Phys. Commun. **77** (1993) 219.
HBOOK Reference Manual.
- [95] P. Aurenche, P. Chiappetta, M. Fontannaz, J. P. Guillet and E. Pilon, Z. Phys. C **56** (1992) 589.
- [96] P. Aurenche, J. P. Guillet and M. Fontannaz, Z. Phys. C **64** (1994) 621
- [97] A. D. Martin, R. G. Roberts, W. J. Stirling and R. S. Thorne, Eur. Phys. J. C **14** (2000) 133
- [98] L. Bourhis, M. Fontannaz and J. P. Guillet, Eur. Phys. J. C **2** (1998) 529
- [99] L. E. Gordon and W. Vogelsang, Phys. Rev. D **52** (1995) 58.
- [100] A. D. Martin, W. J. Stirling and R. G. Roberts, Phys. Lett. B **354** (1995) 155
- [101] L. E. Gordon and J. K. Storrow, Z. Phys. C **56** (1992) 307.
- [102] P. Aurenche, hep-ph/9706386.
- [103] S. Frixione and G. Ridolfi, Nucl. Phys. B **507** (1997) 315
- [104] M. Fontannaz, J. P. Guillet and G. Heinrich, Eur. Phys. J. C **22** (2001) 303
- [105] C. Adloff *et al.* [H1 Collaboration], Eur. Phys. J. C **13** (2000) 415

List of Figures

1.1	Diagrams of electron and proton scattering	3
1.2	Picture of a Lorentz contracted proton with momentum P	5
1.3	The different models for the proton	6
1.4	Sketch of the variation of F_2 as a function of x and Q^2	6
1.5	Picture of a proton probed by photons of different virtualities	7
1.6	Leading order diagrams to define the splitting functions	7
1.7	The three components of the photon structure	8
1.8	Feynman graphs of direct di-jets photo-production events	10
1.9	Feynman graphs of resolved di-jets photo-production events	10
2.1	Example of direct prompt photon processes at leading order	12
2.2	Examples of resolved prompt photon processes at leading order	12
2.3	Diagrams of the prompt photon production (LO cross-sections)	13
2.4	Diagrams of the prompt photon production (NLO calculation)	14
2.5	ZEUS E_T^γ distribution of the prompt photons	15
2.6	ZEUS η^γ distribution of the prompt photons	16
2.7	Cross sections for different prompt photon experiments	18
2.8	E706 prompt photon and π^0 inclusive cross-sections for $\langle k_T \rangle$ studies	19
2.9	NLO calculation compared to E706 prompt photon results	19
3.1	The different components of a Monte-Carlo event generator	20
3.2	Sketch of the breaking of a string into mesons used in the Lund model	21
3.3	Graphs for prompt photon production as handled by PYTHIA and HERWIG	23
4.1	The storage rings of HERA and the pre-accelerators	26
4.2	The definition of the Cartesian coordinate system (x, y, z) at H1	27
4.3	Schematic view of the H1 detector	28
4.4	The different wheels of the LAr Calorimeter	30
4.5	Wheel and cell structure of the LAr calorimeter	31
4.6	Octant and cell structure of the CB1 wheel of the LAr calorimeter	31
4.7	Schematic transverse view of the tracking system	32
4.8	The trigger system	34
4.9	Lateral shower profile distributions for electrons	36
4.10	Lateral shower profile distributions for pions	36
5.1	Shower variables and cuts of the photon finder	39
5.2	Efficiency of the photon finder	40
5.3	Resolution and possible bias for various photon variables	42
5.4	Correlation plots between true and measured y	44
5.5	Resolution and possible bias for various jet variables	46
6.1	Prompt photon candidate in the H1 detector	49
6.2	Fiducial cuts due to trigger efficiency	51
6.3	Trigger Efficiency (years 1998-2000)	52

6.4	Trigger Efficiency (years 1996-1997)	52
6.5	Vertex position Z_{vertex} distribution	53
6.6	A cosmic-ray event and a halo-muon event in the H1 detector	54
6.7	A beam-gas event and a compton event in the H1 detector	54
6.8	Number of tracks fitted to the vertex distribution	55
6.9	Distance of the track impact point on the calorimeter to the cluster candidate	56
6.10	y_{JB} distribution	57
6.11	Transverse energy fraction in the cone around the cluster candidate	58
6.12	Efficiency of the selection cuts	59
7.1	Event with an isolated π^0 selected in background Monte-Carlo sample	61
7.2	Sketch of the expected showers for γ 's and π^0 's	62
7.3	Cluster radius for simulated single γ 's and π^0 's	64
7.4	Cluster hot core fraction for simulated single γ 's and π^0 's	64
7.5	Cluster first layer fraction for simulated single γ 's and π^0 's	65
7.6	Showers discriminator distribution	66
7.7	Effect of the variation of the discriminator cut on the the isolation distribution	67
7.8	Discriminator distributions in all used bins	68
7.9	Distributions of the shower shape variables normalized by the likelihood fits	69
7.10	E_T and η distribution for the selected events	70
7.11	Definition of the variables P_{\perp} , P_{\parallel} and $\Delta\phi$	70
7.12	P_{\perp} , $P_{\parallel} - E_T^{\gamma}$ and $\Delta\phi$ distributions	71
7.13	Distributions E_T^{γ} , η^{γ} , P_T^{jet} , η^{jet} with $P_T^{jet} > 5$ GeV and $P_{\perp} < 1$ GeV	72
7.14	E_T and η distributions for extracted prompt photon candidates	73
7.15	Effect of variation of the isolation cut and radius on the extracted signal	75
7.16	Effect of variation of the isolation cut and radius on the data yield	75
8.1	Correction factors obtained using PYTHIA	77
8.2	Bins purities as a function of E_T and η obtained using PYTHIA	78
8.3	Distributions with shifts of the shower radius for systematics	80
8.4	Distributions with shifts of the shower hot core fraction for systematics	80
8.5	Distributions with shifts of the shower first layer fraction for systematics	81
8.6	Variation of the E_T^{γ} slope for systematics	82
8.7	Efficiency of the cluster-track link	82
8.8	Control plots for the efficiency evaluation of the cluster-track link	83
8.9	Systematic errors for the E_T and η bins	84
9.1	Box contribution to the NLO pQCD calculation by Fontannaz et al.	86
9.2	The prompt photon cross-sections $d\sigma/d\eta^{\gamma}$ predicted by the NLO pQCD calculation by Fontannaz et al.	87
9.3	The prompt photon cross-sections $d\sigma/d\eta^{\gamma}$ predicted by the NLO pQCD calculation by L. Gordon and W. Vogelsang	88
9.4	Multiple interactions effect predicted by the PYTHIA	89
9.5	Prompt photon differential cross sections $d\sigma/dE_T^{\gamma}$ and $d\sigma/d\eta^{\gamma}$ compared to LO and NLO pQCD calculations	90
9.6	Prompt photon differential cross sections $d\sigma/dE_T^{\gamma}$ and $d\sigma/d\eta^{\gamma}$ compared to PYTHIA and HERWIG predictions	91
9.7	Prompt photon differential cross sections $d\sigma/dE_T^{\gamma}$ and $d\sigma/d\eta^{\gamma}$ compared to results of the ZEUS collaboration	92
9.8	Effect of a symmetric cut in E_T^{γ} , E_T^{jet} on the NLO pQCD calculation	93
9.9	Prompt photon + jet differential cross sections $d\sigma/dE_T^{\gamma}$ and $d\sigma/d\eta^{\gamma}$ compared to the prediction of LO and NLO pQCD calculations	94
9.10	Prompt photon + jet differential cross sections $d\sigma/dE_T^{\gamma}$ and $d\sigma/d\eta^{\gamma}$ compared to PYTHIA and the HERWIG predictions	94

List of Tables

2.1	List of experiments on prompt photon production	17
3.1	Integrated luminosities of prompt photons simulated with PYTHIA	23
3.2	Integrated luminosities of prompt photons simulated with HERWIG	24
3.3	Integrated luminosities of hadronic background simulated with PYTHIA	25
5.1	Cut description for photon shower identification	39
6.1	Experimental conditions for the different years	48
6.2	Number of events after the different cuts for the data and the Monte-Carlos	60
7.1	Variation of the isolation cuts used	74
8.1	Factors applied to the shower shape variables for systematics	79

Acknowledgments

I have had the opportunity during my work in the H1 collaboration to enjoy a friendly and enthusiastic environment. It is a pleasure to thank all the people I worked with during this time.

My special thanks go to:

- Jörg Gayler for the great support, guidance and commitment he gave me during my time as a Ph.D. student.
- Prof. Dr. F.W. Büsser for being the supervisor of this thesis and for helpful discussions.
- Prof. Dr. B. Naroska for providing the second report on the thesis.
- Dr. Prof. Dr. R. Klanner for agreeing the financial support of the thesis by DESY.
- Georges Cozzika from the Saclay group who first introduced me to the H1 Collaboration.
- Eram Rizvi, Andrew Metha, Beate Heinemann for their great help with technical aspects of the analysis.
- Katharina Müller for her help in the generation of the PYTHIA and HERWIG Monte-Carlo events.
- Gudrun Heinrich for her help concerning the NLO calculations.
- Manfred Fleischer, Jozef Ferencei, Alexei Babaev, Johannes Haller with whom I worked in the Calorimeter group of H1.
- Alla Grabowsky, Hildegard Haertel and Sabine Platz for their help as secretaries of the H1 collaboration.
- Olivia Worku from the international office for her friendly help with administration matters.
- Florian Keil, Nicolai Tobien, Wenbiao Yan who shared my room at DESY.
- Sophie Gamblin for her friendship and my parents, my sisters and my brothers for their support.
- Gabriela Miu for her support and for a beautiful time.